Full Counting Statistics of Rough Superconducting Tunnel Junctions

Georg Heinrich

München 2007

Full Counting Statistics of Rough Superconducting Tunnel Junctions

Georg Heinrich

Diplomarbeit
an der Fakultät für Physik
der Ludwig–Maximilians–Universität
München

vorgelegt von
Georg Heinrich
aus Heidelberg

München, den 23.10.2007

Erstgutachter: Prof. Dr. Jan von Delft
Zweitgutachter: Prof. Dr. Jörg Kotthaus

Contents

Chapter 1

Introduction

1.1 Noise and mesoscopic transport

For decades physicists have been interested in noise not only as undesirable fluctuations hampering experimental signal detection, but also as an additional source of information. Landauer summarized this in the statement "The noise is the signal" [1]. One of the earliest examples of noise featuring an additional information source was Walter Schottky's work on fluctuations in vacuum diodes [2]. The result, known as the *Schottky formula*

$$S_I = 2eI,$$

relates the zero-frequency noise power of current fluctuations S_I to the average current I and gives direct access to the charge quantum e of the charge carriers, notifying information which is not accessible through conductance measurements only.

An extremely powerful concept in mesoscopic physics is the description of transport through mesoscopically small devices in terms of quantum transport channels or tubes [3]. Each conductor possesses a number of conductance channels depending on its cross sectional area and is characterized by a set of transmission eigenvalues $\{T_n\}$ which correspond to the electron transmission probability through several channels. The total conductance is the sum of contributions from the individual transport channels.

As a well known result, a normal conducting single-mode quantum point contact (QPC), i.e a contact containing only a single quantum transport channel, with transmission T and bias voltage V produces *shot noise* [4]

$$S_I = \frac{Ve^3}{\pi\hbar}T(1-T)$$

As for partition noise, shot noise reflects the uncertainty whether an incident electron is reflected or transmitted through the channel under consideration. In this sense, shot noise refers to the discreteness of charge. In the the limit of small transmission $T \ll 1$ we infer the Schottky formula which is also known as *Poissonian shot noise*.

1.2 Quantum computing

In contrast to classical computers, where information is represented by bits, i.e. two classical, distinct states 0 and 1, a quantum computer uses quantum mechanical variables to store

and process information [5]. Typically, these variables consist of superposed and entangled two-state quantum systems which, in general, are denoted as quantum bits or *qubits*.

Due to the quantum mechanical nature of their fundamental units, quantum computers can capitalize on intrinsic quantum mechanical resources, which are unknown to classical computers and traditional information processing technology, and reveal an enormous source of computing power. Utilizing these resources, various quantum algorithms have been developed which allocate an enormous speedup over classical computation [6, 7, 8].

The challenging requirements that realizations of a quantum computer have to accomplish are summarized by the *DiVincenzo Criteria* [9]. These are first of all the ability to prepare qubits in an initial state, to do coherent manipulations with sufficiently long coherence times using a universal set of gates, to couple qubits with each other and finally to measure their state at the end of computation.

1.3 Superconducting circuits as implementation scheme

So far, no specific physical system is singled out to be the quantum computational device of the future. Since every quantum mechanical two-state system that meets the criteria mentioned above might be considered as a quantum computer, there are several physical systems under investigation. The range of systems reaches from ions trapped in electromagnetic fields [10], NMR [11], to photons [12], and solid-state realizations [13, 14]. Currently the most elaborate systems are found in liquid-state NMR setups, where, as proof of principle, small quantum algorithms have already been carried out [15].

Despite these achievements in NMR and other microscopic systems it seems to be extremely hard to scale these kinds of systems to a large number of qubits where a quantum computer could finally beat its classical counterpart in performance. In this context, implementing qubits using superconducting circuits [13] is very promising, as coupling and scaling to a large number of devices is expected to be straightforward using established circuit fabrication techniques. In addition to scalability, manufacturability and controllability of superconducting qubit devices are assets as well.

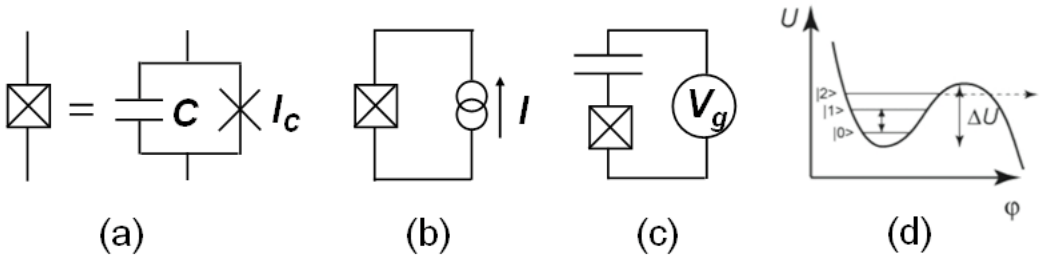

Figure 1.1: (a) Circuit diagram of a Josephson junction including its inherent capacitance and the maximal current through the junction I_c. (b) Circuit diagram of a phase qubit biased by current I. (c) Circuit diagram of a charge qubit or Cooper pair box. The superconducting island is situated between the Josephson junction and the capacitance. (d) Washboard potential of a phase qubit as a function of phase. The potential barrier of hight ΔU can be tuned by the voltage bias. Here it is adjusted such that there are three energy states in the well. $|0\rangle$ and $|1\rangle$ are the qubit states. Higher levels can be used for readout.

The basic idea to describe superconducting qubits is to quantize the Hamiltonian of a given superconducting circuit using the fact that the flux and charge operators are canonically conjugate variables [13]. Following this procedure, depending on the circuit setup, there are basically three types of superconducting qubits. The first type, utilizing flux quantization, is denoted as *flux qubit* and consists of a superconducting loop that is interrupted by a Josephson junction [16, 17, 18]. The two different basis states, which are represented by the magnetic flux pointing in different directions along the loop axis, are superposed and yield symmetric and antisymmetric eigenstates. The second type of qubit, the *charge qubit*, which is sometimes also referred to as *Cooper pair box*, uses charge quantization [19, 20]. The setup consists of a superconducting island which is coupled by a Josephson junction and a capacitance to a superconducting reservoir. The eigenstates which are superimposed refer to different excess charges on the island. The third qubit setup is the *phase qubit*, which consists of a current-biased Josephson junction [21, 22, 23]. The relevant eigenstates are given by the ground and first exited state of the *tilted-washboard potential* [24]. The energy states of a phase qubit's washboard potential and its circuit diagram as well as that of a charge qubit are shown in Figure 1.1.

The crucial device in all the setups presented above, which is indispensable for designing superconducting qubits, is the Josephson tunnel junction which, due to the Josephson effect, introduces an important non-linear circuit element [25]. This feature is necessary to provide an anharmonicity missing in circuits containing solely linear elements such as an LC-resonator. By reason of this non-degenerate level spacing, single-qubit transitions can be addressed selectively and the dynamics of the system can be restricted to only two qubit states. Both are essential to operate qubits.

Hence, understanding Josephson tunnel junctions and all possible features that might be introduced by them is essential to advance building quantum computing devices from superconducting circuits. In this thesis we will be concerned with Josephson tunnel junctions as they are used in superconducting qubit devices.

1.4 Decoherence

One of the major challenges for the realization of practical quantum computing is to do quantum manipulations within the coherence time. The need to maintain quantum coherence during the operation process is especially difficult to achieve in solid state systems. Unlike, for example, in case of an ion trapped in an electromagnetic field, which can be well isolated from its environment, solid-state systems couple relatively strongly to uncontrollable environmental degrees of freedom, such as fluctuations that generate quick decoherence.

The typical understanding of decoherence comprises the two effects of *dephasing* and *energy relaxation*. Dephasing refers to the effect of vanishing phase correlation between states that, for instance, might be caused by fluctuations in the energy-level spacing induced by some sort of noise. This process finally leads to a classical state mixture instead of quantum mechanical superposition. In contrast, relaxation refers to energy exchange and usually leads to thermal equilibrium.

Gaussian noise sources can be described with a heat bath modeled by a set of harmonic oscillators that represent unobserved environmental degrees of freedom [26]. In such an approach, the complete system consisting of the two-state system and the bath is fully quantum-coherent. However, the reduced system, which is obtained after integrating out the bath's

degrees of freedom, shows both relaxation and dephasing. Central for describing decoherence in this scheme is the symmetrized spectral noise power

$$S(\omega) = \frac{1}{2}\int_{-\infty}^{\infty} d\tau\, e^{i\omega t}\, \langle \xi(\tau)\xi(0) + \xi(0)\xi(\tau)\rangle$$

due to quantum noise $\xi(t)$ where $\langle \ldots \rangle$ denotes quantum statistical average. (Later, $\xi(t)$ will be the current fluctuation operator $\delta I(\tau) = I(\tau) - \langle I \rangle$).

This way, by choosing appropriate spectral densities, we can model Gaussian noise sources, where only the first two cumulants are non-zero. However, after electromagnetic qubit environments have been successfully shaped to improve decoherence we are now mostly concerned with intrinsic noise of the solid state system. Hence in this thesis we will investigate the intrinsic noise of few high-transmission channels, so-called *pinholes*, that potentially reside in the Josephson tunnel junction.

1.4.1 1/f noise

The most prominent source of intrinsic decoherence is non-Gaussian 1/f noise, for which the spectral function behaves like $S(\omega) \propto 1/\omega$ [27, 28]. Although 1/f noise is ubiquitous in solid-state systems, a fully universal origin has not yet been found. 1/f noise typically appears due to slowly moving defects in strongly disordered materials and is usually explained by two-level fluctuators that couple to the system under consideration. A heat bath causes uncorrelated switching events between the two states, which are described by a Poissonian distribution with mean switching time τ. For a single fluctuator this model is known as *random telegraph noise*. Superposing several such fluctuators using an appropriate mean switching time distribution $\rho(\tau)$ results in a 1/f noise spectrum.

A prominent, possible decoherence mechanism for low-frequency 1/f noise in junctions of superconducting qubits is critical-current fluctuations due to charge trapping at defects in the tunnel barrier [29]. As a result of Coulomb repulsion, a trapped electron might block tunneling through a region of the junction and hence effectively modulate the junction area or the number of transport channels. Consequently, the untrapped state results in high critical current. The trapped state results in low critical current. Thus, a single-charge fluctuator can produce random telegraph noise due to the charge-fluctuator state and its lifetime. Considering several fluctuators with appropriate lifetime distribution leads to 1/f noise as mentioned above.

1.5 Rough superconducting tunnel junctions

The crucial importance of Josephson junctions for designing superconducting qubits was emphasized in Section 1.3. The oxide layer defining the Josephson junction between the two superconductors can be considered as an insulator. It is a well-known concept in mesoscopic physics to describe transport through such sufficiently small scatterers by quantum transport channels [3]. In the following, when we discuss transmission eigenvalues or channels of Josephson junctions, we will always implicitly refer to those of the respective oxide layer.

Typically, Josephson junctions, as used in superconducting qubit devices, are considered as tunnel junctions, meaning that the transmission eigenvalues of all transport channels are assumed to be small. However, the fabrication process is not at all epitaxial quasi-equilibrium

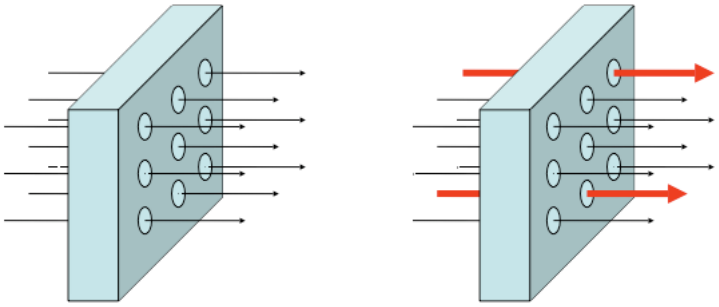

Figure 1.2: Schematic diagram of the oxide layer of a Josephson Junction. Several transport channels are indicated. The arrow thickness corresponds to the respective transmission eigenvalue. Left: schematic diagram of an ideal Josephson tunnel junction. The transmission of all channels is small. Right: considered *rough Josephson tunnel junction*, i.e., a tunnel junction including some high-transmission channels: so-called *pinholes*.

growth, thus one has to expect the oxide layer to be non-crystalline and disordered. Hence, in this thesis we will investigate *rough superconducting tunnel junctions*, where we assume that the junction additionally possesses some transport channels with very high transmission eigenvalues: so-called *pinholes*, see Figure 1.2. These pinholes might occur as defects due to the fabrication process. Indeed in Ref. [30, 31] the importance of pinholes was pointed out, but also work in Ref. [32] discusses the significance of pinholes in mesoscopic devices, e.g., for the Kondo effect.

Not long ago, there was particular interest in pinholes to understand subharmonic gap structure in weak links, meaning current characteristics as a function of voltage for voltage energies smaller than the superconducting gap 2Δ. In Ref. [33] the subharmonic gap structure of a tunnel junction was modeled by assuming that 30 percent of all transmission channels have pinhole character with transmission eigenvalue $T = 0.6$. Regarding superconducting qubits having an amount of pinholes in the Josephson junction is particularly interesting in many respects. We will present some of these motivating aspects in the following subsections.

1.5.1 Multiple Andreev Reflections (MAR)

In Josephson Junctions with voltage bias smaller than the superconducting gap, direct tunneling is impossible due to the energy gap 2Δ. In this case, effective charge transport is governed by *Multiple Andreev Reflection* (MAR), see Ref. [34, 35, 36]. *Andreev Reflections* occur at contacts consisting of a scatterer and a superconductor, see Figure 1.3. For voltage bias smaller than the superconducting gap, electrons from the scatterer have insufficient energy to be transferred to the superconductor as quasiparticles. Charge can only be transmitted in a higher-order process, where a normal electron grabs a second one with adequate energy and momentum to generate an additional Cooper pair. Hence, in this process effectively two electrons are transferred at a time. After this process, the missing electron appears as a reflected hole.

In a system consisting of two superconductors separated by a scatterer there are two superconductor-scatterer interfaces, where Andreev Reflection can occur. This leads to processes involving sequential Andreev cycles known as Multiple Andreev Reflections, in which

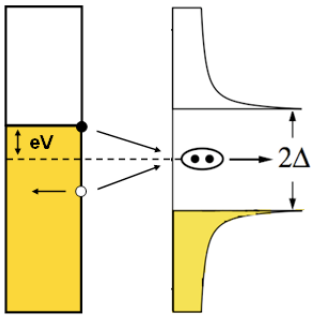

Figure 1.3: Andreev Refection in a schematic energy diagram between a scatterer (left) and a superconductor possessing energy gap 2Δ (right) at $T = 0K$ and voltage bias $V \leq 2\Delta/e$. The diverging density of states of the superconductor is indicated. Energy levels are filled up to the Fermi energy (colored). Due to the energy gap, direct tunneling is impossible and charge can only be transferred in a higher order process where a normal conducting electron grabs a second one with adequate energy and momentum to generate an additional Cooper pair in the superconductor. After the process the missing electron appears as a reflected hole.

charge can be transferred even for voltages smaller than $2\Delta/e$, see Figure 1.4.

In general, an n^{th} order MAR process transferring n charge quanta at a time, a so-called *Andreev cluster*, comprises $(n-1)$ Andreev Reflections and occurs above a threshold voltage

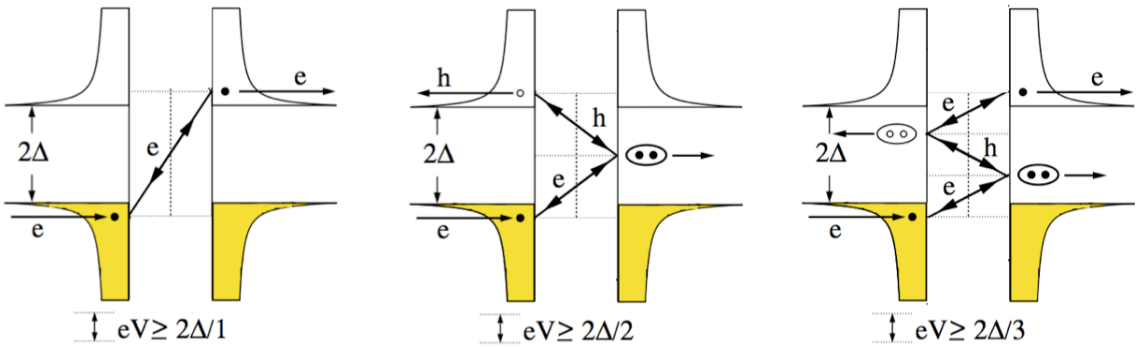

Figure 1.4: Schematic diagram of charge transport trough a weak link involving Multiple Andreev Reflection (MAR) for different voltage bias, taken from Ref [37]. Left: voltage energy larger than the superconducting energy gap. As indicated, direct quasi-particle transport is possible. Middle: $eV \geq 2\Delta/2$. An electron coming from the left, crossing the center, gains energy eV. However, this is insufficient to enter the second superconductor as a quasi-particle. After Andreev Reflection due to the reversed charge sign, the reflected hole gains additional energy eV on its way back to the left superconductor such that in total, the excitation can overcome the superconducting energy gap. Charge transport at this voltage involves at least one Andreev Reflection and conveys at least two charge quanta at a time. Right: $eV \geq 2\Delta/3$. Charge transport involves at least two Andreev Reflections and conveys at least three charge quanta at a time.

$V_n = 2\Delta/(en)$. For voltages below this so-called *MAR voltage* V_n, the energy gap cannot be overcome by n crossings. As these processes are composed of several transmission cycles, it is intuitively clear that they will sensitively depend on the electron transmission probability, i.e., the set of transmission eigenvalues characterizing the junction.

Hence, coming back to our original interest, rough superconducting tunnel junctions will be highly affected by MAR and we will see that even very few pinholes will have an extreme impact on the junction.

1.5.2 Noise enhancement due to MAR

In Ref. [30, 31], shot noise of $NbN/MgO/NbN$ superconductor-isulator-superconductor tunnel junctions was measured. The result of this measurement is shown in Figure 1.5 and shows shot noise enhanced by Andreev reflection. The authors attributed this to the occurrence of MAR processes in pinholes, which are assumed to be present in the MgO barrier. They modeled their data assuming Poissonian shot noise $2eI$, where they replaced the single charge quantum e by an effective transferred charge $q(V)$, due to MAR.

Such processes might be highly relevant as a source of intrinsic noise in superconducting qubit devices due to pinholes residing in the Josephson junction. As a first guess, we might think of arbitrarily large Andreev clusters transferred due to MAR in very high-transmission channels, that might drastically enhance Poissonian shot noise $2eI$ due to the effectively transferred charge. On the other hand, in the case of transport through pinholes, this intuitive idea has to be revised, as the Poissonian shot noise formula is strictly only valid in the case of small transmission.

The method, we will use to investigate rough superconducting tunnel junctions, properly deals with all possible transmission eigenvalues. Hence, quantitative statements on the impact

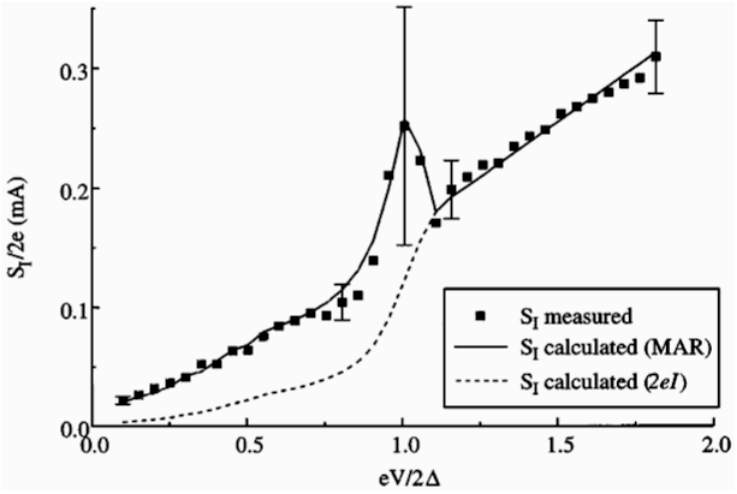

Figure 1.5: Andreev Reflection enhanced shot noise in $NbN/MgO/NbN$ superconductor-insulator-superconductor tunnel junctions measured in Ref. [30]. The dashed line corresponds to naively guessed expected Poissonian shot noise which would be directly proportional to the measured current. The (MAR) labeled line includes an increased effective charge due to MAR.

of rough barriers will be possible.

1.5.3 Junction Resonators

One of the central measurements revealing major intrinsic sources of decoherence in Josephson junction qubits was performed in Ref. [38]. After improving their phase qubit, the authors performed spectroscopy, driving transitions between qubit states $|0\rangle$ and $|1\rangle$ with excitation frequency ω and reading out state $|1\rangle$ via higher non-qubit states, see Figure 1.1 (d). The experimental result is shown in Figure 1.6. Apart from the theoretically expected decrease in

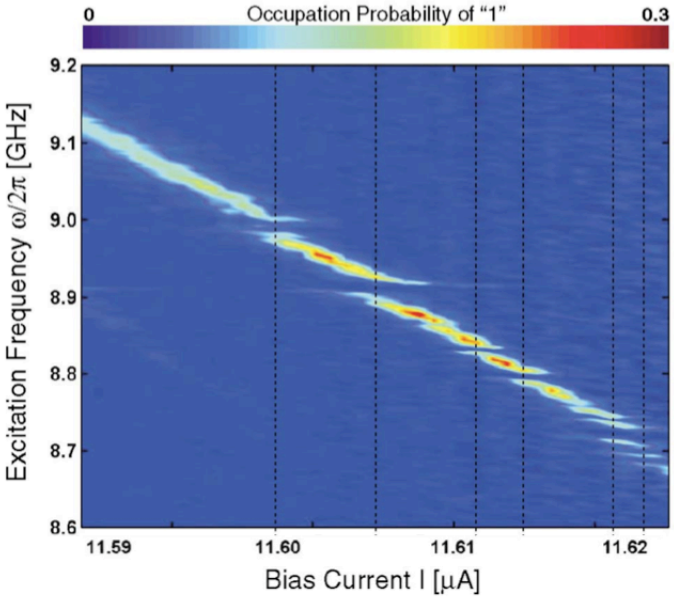

Figure 1.6: Spectroscopy on a phase qubit done in Ref. [38]. For a given bias current transitions between qubit states $|0\rangle$ and $|1\rangle$ are driven with excitation frequency ω. The $|1\rangle$ qubit state is read out. Its occupation probability is encoded in terms of color. Dotted vertical lines are centered at level splittings due to so-called spurious resonators.

transition frequency for bias current approaching the critical current, at certain voltages, there are characteristics of energy-level repulsion, as predicted for coupled two-state systems. This structure of level-splittings that is unique for different, but identically constructed qubits, and thus, can be considered as a 'qubit fingerprint', was attributed to so-called *spurious resonators* residing in the Josephson tunnel junction. Measurements of Rabi oscillations revealed that these resonators cause significant decoherence. Similar to a scenario of charge trapping, mentioned in Section 1.4.1 with respect to 1/f noise, the energy-level repulsion could be explained by assuming two-state current fluctuators in the junction. Since its first measurement, new designs separating the capacitance from now smaller Josephson tunnel junctions have significantly reduced the number of two-level fluctuators coupled to the qubit, see Ref. [39].

Although other processes such as charge trapping might be more relevant effects for realizing such spurious resonators within the junction barrier, pinholes in rough tunnel junctions considered here might be additional candidates for introducing two-state current fluctuators,

see Section 9.3.

1.6 Methods

To investigate rough superconducting tunnel junctions with respect to the raised questions, we will be interested in the *full counting statistics* (FCS) of charge transfer through the junction. This is the probability distribution $P_{t_0}(N)$ for N total charge quanta to be transmitted within measurement time t_0. This probability distribution will not only supply us with the noise characteristic proportional to the second cumulant, but also with all other cumulants that are especially important in describing non-Gaussian noise such as contributions resembling two-level systems.

To calculate $P_{t_0}(N)$ we will use the non-equilibrium Keldysh Green's function approach, which was at first suggested in Ref. [40]. Within this scheme, by diagrammatic expansion technique, the full counting statistics of a general quantum mechanical variable can be related to Keldysh Green's functions, which were originally invented to describe non-equilibrium systems and turned out to be particularly useful in the case of non-equilibrium superconductors. By doing so, we can use several quantum field-theoretical methods used in the transport theory of metals [41] and describe the system under consideration microscopically. This way, we accurately take into account high transmission channels and the effects due to Multiple Andreev Reflections.

Chapter 2

Full Counting Statistics

2.1 General aspects on FCS

Having motivated the the interest in noise as an additional source of information, see Section 1.1, it is natural to ask for *higher correlators* of the current operator, see Section 1.4, to obtain more information on the transport process. To make calculation of these correlators feasible, and thereby gain deeper insight into the transport process of electrons in solid-state systems, Levitov and Lesovik introduced the concept of *full counting statistics* (FCS), already known in the field of quantum optics, to mesoscopic physics [42, 43, 44]. In quantum optics, it is experimentally possible to count the number of photons occupying a certain quantum state, see Ref. [45]. Due to quantum and thermal fluctuations, this result fluctuates and a statistical description of the number of counted photons is necessary. Conceptually generalized, in mesoscopic physics, the full counting statistics refers to the probability distribution $P_{t_0}(N)$ for N electrons having passed a certain conductor within the measurement time t_0. Equivalently, instead of computing $P(N)$, we can also regard its *cumulant generating function* (CGF) $S(\chi)$

$$\exp[S(\chi)] = \sum_N P_{t_0}(N) \exp(iN\chi). \tag{2.1}$$

Given the full counting statistics, we can calculate all cumulants

$$C_1 = \bar{N} \equiv \sum_N N P_{t_0}(N),$$

$$C_2 = \overline{(N-\bar{N})^2},$$

$$C_3 = \overline{(N-\bar{N})^3},$$

$$C_4 = \overline{(N-\bar{N})^4} - 3\overline{(N-\bar{N})^2}^2,$$

and so on. Sequentially the meaning of the first three cumulants, with respect to the probability distribution, are average, width and skewness. More easily, the cumulants can be determined by the cumulant generating function

$$C_n = (-i)^n \left.\frac{\partial^n}{\partial \chi^n} S(\chi)\right|_{\chi=0}.$$

Hence, altogether the full counting statistics, as a new concept in mesoscopic physics, represents all information on the electron transport process contained in charge counting.

2.2 Attempts to calculate the FCS

The central question in the following chapters will be be how the full counting statistics, or equivalently the cumulant generating function, can be calculated. The first idea to establish full counting statistics in mesoscopic physics [42] was to consider a transfered-charge operator

$$\hat{Q} = \int_0^{t_0} dt\, \hat{I}(t). \tag{2.2}$$

Very intuitively, this operator counts transfered charge quanta. The operator of electrical current is well-defined in the Fockspace spanned by the scattering states of electrons and it might appear reasonable to apply the measurement postulate of quantum mechanics. Following this approach, the probability for N charge quanta being transfered equals to the square of the projection of the system state on the eigenstate of $\hat{Q}$ with eigenvalue N. However, the result turned out to be unsatisfactory, for example, see Ref. [42], the quantum of charge in this approach was given by the non-interger $2e\sqrt{T}$, where T was the transparency of the quantum channel under consideration.

The problem is that operator 2.2 in connection with the measurement postulate of quantum mechanics does not properly respect causality. The measurement paradigm, described above, assumes an instantaneous measurement. In contrast, Equation 2.2 accumulates information over the measurement time t_0. Generally, causality in quantum mechanics is introduced by a time ordering operator which seems to be missing in the expression above. To address this, in preceding work [43, 44], it was pointed out that the electrical current operators, appearing in Equation 2.2 at different times, do not commute so that, in general, the operator of transfered charge $\hat{Q}$ is unphysical. Instead, the measurement device has to be included into the system Hamiltonian. In Ref. [44], this was done by introducing a spin-1/2 detector, modeling a quantum galvanometer, consisting of a spin 1/2 that precesses in the magnetic field of the current.

In Ref. [46], this idea was further elaborated by defining the full counting statistics of a general quantum mechanical variable $\hat{A}$, replacing the specific current operator $\hat{I}$ above. This way, by using an exact quantum mechanical description of the measurement setup in terms of a path integral over detector variables, the essence of statistics was pointed out and the full counting statistics was generally adopted as relation between quantum mechanical density operators. This deeper understanding is fundamental to appreciate and cope with the calculation of "negative probabilities" for transport between superconductors reported in Ref. [47].

Therefore, in the remainder of this chapter, we will present the full counting statistics of a general quantum mechanical variable basically following Ref. [46] although, we will add some additional calculation steps and remarks to improve comprehensibility. The following chapters will build on this and will present how, based on this general expression, quantum-field theoretical methods can be used to calculate the full counting statistics of charge transport.

2.3 FCS of a general quantum mechanical variable

As a generalization of the counting statistics in electrical transport, we are generally interested in the expression $\int dt\, \hat{A}(t)$, where $A(t)$ is an arbitrary quantum mechanical observable. Note that for an arbitrary operator, in general, the result does not have to be discrete, like in case

of counting charges. However, the term "counting" is kept. In the general case of an arbitrary operator $\hat{A}$, to properly take into account the measuring device and its back-action on the system, we introduce a detector variable x whose operator $\hat{x}$ commutes with all operators of the system to be measured. We assume that the canonically conjugate detector variable q, with $[\hat{x}, \hat{q}] = i$, can be measured following the measurement postulate of quantum mechanics. (Here we use units with $\hbar = 1$). The basic idea will be to introduce a detector-system interaction such that, during the measurement time t_0, the Heisenberg equation of motion is given by

$$\dot{\hat{q}}(t) = \hat{A}(t).$$

This way, the time integral of $\hat{A}(t)$ is accurately linked to an operator that, as postulated, can be measured.

The detector, given its one degree of freedom x and canonically conjugated variable q, is modeled with the Hamiltonian $\hat{q}^2/2m$. We assume a linear coupling of the detector variable x to the system operator $\hat{A}$ that is measured within the measurement time interval $(0, t_0)$. Given appropriate times $t_a < 0$ and $t_b > t_0$, a smooth coupling function

$$\alpha_{t_0}(t) = \begin{cases} 1 & t \in (0, t_0) \\ 0 & t \notin [t_a, t_b] \\ \text{adiabatic switching} & \text{else} \end{cases} \tag{2.3}$$

provides adiabatic coupling between detector and system. The entire Hamiltonian, comprising the measured system and the detector, amounts to

$$\hat{H}(t) = \hat{H}_{sys} - \alpha_{t_0}(t)\hat{x}\hat{A} + \frac{\hat{q}^2}{2m} \tag{2.4}$$

and the Heisenberg equation for the detector variable q reads

$$\dot{\hat{q}}(t) = \frac{1}{i}[\hat{q}, \hat{H}] = \alpha_{t_0}(t)\hat{A}(t)$$

suggesting that the statistics of variable q, after measurement time t_0 and uncoupling the detector from the system, corresponds to the statistics of the expression $\int_0^{t_0} dt\, \hat{A}(t)$, that we are interested in. To rule out classical back-action of the detector, we will consider a static detector in the limit $m \to \infty$ such that $\dot{\hat{x}} = 0$.

Given the detector model and the entire Hamiltonian 2.4, comprising detector and the measured system, we can ask the question how can we calculate the full counting statistics from this. To obtain the statistics of measurement outcomes, we need the reduced density matrix of the detector. This way it will be possible to relate the detector's density-matrix elements after measuring $\rho^f(x_1, x_2) = \langle x_1|\hat{\rho}^f|x_2\rangle$, $t \geq t_b$, to the ones before the measurement has taken place $\rho^{in}(x_1, x_2) = \langle x_1|\hat{\rho}^{in}|x_2\rangle$, $t \leq t_a$. We will define the full counting statistics to be contained in this expression using path integrals.

In basic quantum mechanics [48], the propagator between two states, $|x_N, t_N\rangle$ at time t_N and $|x_1, t_1\rangle$ at time t_1, can be written in terms of a Feynman path integral

$$\begin{aligned} \langle x_N, t_N|x_1, t_1\rangle &= \langle x_N, t_1|\hat{\mathscr{U}}^\dagger(t_N, t_1)|x_1, t_1\rangle \\ &= \int_{x_1}^{x_N} \mathscr{D}[x(t)]\ \exp\left[i \int_{t_1}^{t_N} dt\ \tfrac{L_{classical}(x,\dot{x})}{\hbar}\right], \end{aligned} \tag{2.5}$$

where $\int_{x_1}^{x_N} \mathscr{D}[x(t)]$ denotes integration over all paths with fixed starting point x_1 and fixed end point x_N. The time integral over the classical Lagrangian is also known as action S.

To understand the structure of later formulas, let us first neglect the measured system and consider only the detector. Then the detector's density matrix can easily be written in the form of two path integrals

$$\begin{aligned}
\rho^f(x_1,x_2) &= \langle x_1|\hat{\mathscr{U}}^\dagger(t_b,t_a)\,\hat{\rho}^{in}\,\hat{\mathscr{U}}(t_b,t_a)|x_2\rangle \\
&= \int dx' \int dx''\ \langle x_1|\hat{\mathscr{U}}^\dagger|x'\rangle\langle x'|\hat{\rho}^{in}|x''\rangle\langle x''|\hat{\mathscr{U}}|x_2\rangle \\
&= \int_{\tilde{x}_1(t_b)=x_1} \mathscr{D}[\tilde{x}_1(t)] \exp\left[iS_{Det}(\tilde{x}_1(t))\right] \\
&\times \int_{\tilde{x}_2(t_b)=x_2} \mathscr{D}[\tilde{x}_2(t)] \exp\left[-iS_{Det}(\tilde{x}_2(t))\right]\ \rho^{in}(\tilde{x}_1(t_a),\tilde{x}_2(t_a)),
\end{aligned} \tag{2.6}$$

where S_{Det} denotes the detector action. Due to the detector Hamiltonian $\hat{q}^2/2m$, it is given by

$$S_{Det}(x) = \int_{t_a}^{t_b} dt\ \frac{m}{2}\dot{x}^2.$$

Note that, in contrast to the propagator for the wave function (2.5), for both integrals in Equation 2.6 only the end point $\tilde{x}_i(t_b)$ is fixed. The start point is integrated out. Hence, there is implicit integration over both arguments of the initial density matrix $\rho^{in}(\tilde{x}_1(t_a),\tilde{x}_2(t_a))$ which are always given by the starting point $\tilde{x}_i(t_a)$ of the two specific paths under consideration.

Now we come back to the entire Hamiltonian 2.4 considering detector and measured system. $\hat{\rho}^{system}$ denotes the initial density matrix of the system. We assume that the entire density matrix is initially factorized, thus $\hat{D} = \hat{\rho}^{system}\hat{\rho}^{in}$. Remember, when modeling the measuring device we already assumed the operator $\hat{x}$ to commute with all system operators. To find the reduced density matrix of the detector after the measurement, the system's degrees of freedom have to be traced out. Hence we have

$$\begin{aligned}
\rho^f(x_1,x_2) &= \mathrm{Tr}_{System}\langle x_1|\hat{\mathscr{U}}^\dagger(t_b,t_a)\,\hat{\rho}^{system}\hat{\rho}^{in}\,\hat{\mathscr{U}}(t_b,t_a)|x_2\rangle \\
&= \mathrm{Tr}_{System}\left\langle x_1\left|\overrightarrow{T}\, e^{-i\int_{t_a}^{t_b} dt\,[\hat{H}_{sys}-\alpha_{t_0}(t)\hat{x}\hat{A}+\hat{q}^2/2m]}\right.\right. \\
&\times \left.\left.\hat{D}\,\overleftarrow{T}\, e^{i\int_{t_a}^{t_b} dt\,[\hat{H}_{sys}-\alpha_{t_0}(t)\hat{x}\hat{A}+\hat{q}^2/2m]}\right|x_2\right\rangle,
\end{aligned} \tag{2.7}$$

where we have inserted the time-evolution operator using time- $\overrightarrow{T}$, and anti-time-ordering operator $\overleftarrow{T}$.

Basically, we can proceed using path integrals like in Equation 2.6. Due to the larger Hilbert space, which is now composed of system and detector spaces, to construct our complete set of states we use product states, generated by any complete set of states of the system and the detector. By inserting such designed sets into Equation 2.7, using alternately complete sets of eigenstates of the position or the momentum operator of the detector, in Ref. [46] the position and momentum operator in the exponential were replaced by their eigenvalues. Therewith, we receive an expression in terms of double path integrals whose structure is

similar to Equation 2.6

$$\begin{aligned}\rho^f(x_1,x_2) &= \int_{\tilde{x}_1(t_b)=x_1}\mathscr{D}[\tilde{x}_1(t)]\int_{\tilde{x}_2(t_b)=x_2}\mathscr{D}[\tilde{x}_2(t)]\,\rho^{in}(\tilde{x}_1(t_a),\tilde{x}_2(t_a))\,e^{iS_{Det}(\tilde{x}_1(t),\tilde{x}_2(t))}\\ &\times \mathrm{Tr}_{System}\left[\overrightarrow{T}\,e^{-i\int_{t_a}^{t_b}dt\,[\hat{H}_{sys}-\alpha_{t_0}(t)\tilde{x}_1(t)\hat{A}]}\hat{\rho}^{system}\overleftarrow{T}\,e^{i\int_{t_a}^{t_b}dt\,[\hat{H}_{sys}-\alpha_{t_0}(t)\tilde{x}_2(t)\hat{A}]}\right],\end{aligned} \tag{2.8}$$

where the detector action is given by

$$S_{Det}(\tilde{x}_1(t),\tilde{x}_2(t)) = \int_{t_a}^{t_b} dt\,\frac{m}{2}\left[\dot{\tilde{x}}_1(t)^2-\dot{\tilde{x}}_2(t)^2\right].$$

Again, for both path integrals only the end point $\tilde{x}_i(t_b)$ is fixed and hence, there is implicit integration over both arguments of the initial density matrix of the detector $\rho^{in}(\tilde{x}_1(t_a),\tilde{x}_2(t_a))$ via the starting points of each path considered.

One of the crucial steps here and in Ref. [46] is to replace the detector's operators $\hat{x}$ and $\hat{q}$ by their eigenvalues, by virtue of the argument given above. Nevertheless, this step is far from being trivial. For instance, although by definition the operator $\hat{x}$ commutes with all system operators, because it acts on a different Hilbert space, we still have $[\hat{x},\hat{q}]=i$. This relation does not have to be taken into account, but it is implicit in the use of path integrals, see Ref. [49].

We make this point explicit by summarizing the derivation of path integrals in the simplest case of a Hamiltonian in its standard form, being the sum of a kinetic and a potential energy

$$\hat{H} = T(\hat{p},t)+V(\hat{x},t),$$

which is, for example, given in Ref. [50]. Note that, if we take into account that the measured system is traced out, the Hamiltonian 2.4 has this form. To find the Feynman description of a propagator like that given in Equation 2.5, it is standard procedure to slice the time-evolution operator into infinitesimal ($N\to\infty$) time intervals of width $\epsilon\equiv t_n-t_{n-1}=(t_N-t_1)/(N+1)$ and factorize the displacement operator for these time intervals according to the *Baker-Campbell-Hausdorff formula*

$$\begin{aligned}e^{-i\epsilon\hat{H}/\hbar} &= e^{-i\epsilon(\hat{T}=\hat{V})/\hbar} = e^{-i\epsilon\hat{V})/\hbar}e^{-i\epsilon\hat{T}/\hbar}e^{-i\epsilon^2\hat{X}/\hbar^2}\\ \hat{X} &\equiv \frac{i}{2}[\hat{V},\hat{T}]-\frac{\epsilon}{\hbar}\left(\frac{1}{6}[\hat{V},[\hat{V},\hat{T}]]-\frac{1}{3}[[\hat{V},\hat{T}],\hat{T}]\right)+\ldots.\end{aligned}$$

To proceed, firstly, powers of ϵ are neglected and, due to factorization of $e^{-i\epsilon\hat{H}/\hbar}$, it is straightforward to derive an expression for the propagator like that given in Equation 2.5 and thereto, replace operators by their eigenvalues. Finally, it can be easily shown that in the limit $N\to\infty$ the commutator term proportional to ϵ^2 does not contribute such that the approximation converges to something other than the expression given in Equation 2.5. Expressions of this kind are called the *Trotter product formula*.

From this short review of the derivation we essentially see that the replacement of the detector operators by their eigenvalues is central to Feynman path integrals. The set of paths takes care of the commutation relation which is inherent in this formulation of quantum mechanics. This is one of the central incentives and gains of describing the system in terms of path integrals.

Having understood Equation 2.8, by introducing a kernel K we can rewrite this expression as

$$\rho^f(x_1, x_2) = \int d\tilde{x}_1 \int d\tilde{x}_2 K(x_1, x_2; \tilde{x}_1, \tilde{x}_2)\rho^{in}(\tilde{x}_1, \tilde{x}_2).$$

Taking the limit of infinite detector mass, ruling out classical back-action, the detector action S_{Det} in Equation 2.8 suppresses all fluctuations in the path integrals. In the appendix of Ref. [46] it was shown that the kernel becomes local in position space

$$K(x_1, x_2; \tilde{x}_1, \tilde{x}_2) = \delta(x_1 - \tilde{x}_1)\delta(x_2 - \tilde{x}_2)P(x_1, x_2, t_0)$$

with

$$P(x_1, x_2, t_0) \quad = \quad \mathrm{Tr}_{System}\left[\overrightarrow{T}\, e^{-i\int_{t_a}^{t_b} dt\, [\hat{H}_{sys} - \alpha_{t_0}(t)x_1\hat{A}]}\hat{\rho}^{system}\, \overleftarrow{T}\, e^{i\int_{t_a}^{t_b} dt\, [\hat{H}_{sys} - \alpha_{t_0}(t)x_2\hat{A}]}\right] \tag{2.9}$$

Equation 2.9 is the central result concerning the full counting statistics of a general quantum mechanical variable, comprising the entire statistics we are interested in. To see this, it is instructive to rewrite the density matrices in Wigner representation

$$\rho(x, q) = \int \frac{d\chi}{2\pi}\, e^{-iq\chi}\, \rho(x + \frac{\chi}{2}, x - \frac{\chi}{2})$$

and define

$$P(x, q, t_0) = \int \frac{d\chi}{2\pi}\, e^{-iq\chi}\, P(x + \frac{\chi}{2}, x - \frac{\chi}{2}, t_0). \tag{2.10}$$

Then, we finally get a convolution relating the reduced density matrix of the detector after the measurement to the one before measuring

$$\rho^f(x, q) = \int dq_1\, P(x, q - q_1, t_0)\, \rho^{in}(x, q_1) \tag{2.11}$$

Following Ref. [46], Equation 2.9 to 2.11 define the full counting statistics of the variable A. If we assume that we can interpret the detector and its density matrix classically, $\rho(x, q)$ in Wigner representation gives the probability for the detector to be at position x showing momentum q. Thus, in this interpretation the kernel $P(x, q, t_0)$ of convolution 2.11 gives the probability of shifting the detector's momentum. Consequently, in this classical interpretation, $P(x, q, t_0)$ gives the probability of having measured $q = \int_0^{t_0} dt\, A(t)$.

Certainly, in general, the density matrix in Wigner representation cannot be interpreted in this classical sense since it is not everywhere positive. In fact, non-positivity is a hallmark of non-classicality, see Ref. [51]. Nevertheless, Equation 2.11 still predicts the outcome of measurement. Thus, due to the fact that the full counting statistics is defined as a relation between density matrices, quantum-mechanically the calculation of "negative probabilities", as reported in Ref. [47], can make sense but we have to beware of interpreting these results classically.

Anyhow, we can immediately find a situation where the classical interpretation of $P(x, q, t_0)$ is applicable. If $P(x, q, t_0)$ does not depend on x we can integrate Equation 2.11 to

$$\Pi^f(q) = \int dq_1\, P(q - q_1)\, \Pi^{in}(q_1),$$

where $\Pi^k(q) \equiv \int dx\ \rho^k(x,q)$. In this case the full counting statistics relates the probability distribution of the detector before and after the measurement, i.e., $\Pi^{in}(q)$ and $\Pi^f(q)$, which are now positive and, thus, so is $P(q,t_0)$. A glance at Equation 2.10 shows that this is the case if $P(x_1,x_2,t_0)$, in Equation 2.9, does only depend on the difference $x_1 - x_2$. Therefore, we immediately see that the possibility of classical interpretation of the full counting statistics is associated with certain symmetries.

Further analysis reveals that, in case of charge transport, this symmetry is related to gauge invariance. In the normal conducting case, using a specific gauge transformation, see Ref. [40, 46], it is possible to transform $P(x_1,x_2,t_0)$ to an $(x_1 - x_2)$-dependence. In the superconducting case, the mean-field approach of the BCS theory, see Ref [24], sets a fixed phase. Thus, in this mean-field sense, superconductivity breaks gauge invariance and it turns out that we cannot transform to an $(x_1 - x_2)$-dependence anymore, making the classical interpretation of the full counting statistics, given above, impossible. This is precisely the reason for the emerging "negative probabilities" in the superconducting case, reported in Ref. [47]. Thus, regarding our interest in rough superconducting tunnel junctions, we will have to take care of this issue later on.

As a final remark, we note that, in the case when the measurement time t_0 exceeds the time scale associated with the system, $P(x_1,x_2,t_0)$, given in Equation 2.9, can be directly related to the cumulant generating function by using a simple saddle point approximation [46]

$$P(x_1,x_2,t_0) = e^{S(x_1,x_2)}.$$

That such a relation makes sense can already be seen by comparing Equation 2.10 with the definition of the cumulant generating function in Equation 2.1. In the above mentioned case, where we can interpret $P(x,q,t_0)$ (Equation 2.10) classically and $P(x_1,x_2,t_0)$ (Equation 2.9) does only depend on the difference $\chi = x_2 - x_1$, we find for the cumulant generating function

$$e^{S(\chi)} = \mathrm{Tr}_{System}\left[\overrightarrow{T}\, e^{-i\int_0^{t_0} dt\,[\hat{H}_{sys}+\frac{\chi}{2}\hat{A}]}\ \hat{\rho}^{system}\ \overleftarrow{T}\, e^{i\int_0^{t_0} dt\,[\hat{H}_{sys}-\frac{\chi}{2}\hat{A}]}\right], \tag{2.12}$$

where finally we have considered the smooth coupling function $\alpha_{t_0}(t)$ defined in Equation 2.3.

Chapter 3

Quantum field-theoretical methods

3.1 Keldysh Green's functions formalism

Quantum field theoretical methods formulated in terms of Green's functions are a powerful instrument in many-body problems, see for example [52, 53]. Many systematic methods and calculation schemes have been formulated for them. The Keldysh Green's Function formalism [54, 55] is a diagrammatic approach, analogous to the usual Feynman technique in field theory, see for example [56], which was developed to describe many-body systems out of equilibrium. This formalism turns out to be particularly useful in the case of nonequilibrium superconductors [57, 58]. Concerning our goal to describe charge transport through a rough superconducting tunnel junction, the Keldysh technique will be essential to connect the general full counting statistic, basically given in Equation 2.9, to a microscopic description of the junction in terms of Green's Functions.

We consider a physical system described by the time-independent Hamiltonian

$$H = H_0 + H^i \tag{3.1}$$

that is composed of the free particle part H_0 and the interaction between particles H^i. Such a decomposition for time-independent Hamiltonians becomes convenient in the case of a diagrammatic Green's function expansion in terms of the single-particle propagator. In thermodynamic equilibrium, the state of the system is described by the statistical operator

$$\rho(H) = \frac{e^{-\beta H}}{\mathrm{Tr}\left[e^{-\beta H}\right]}.$$

The standard way to introduce a nonequilibrium state is to disconnect the system from the reservoir, with which it is assumed to be in thermodynamic equilibrium at time t_0, and expose it to a disturbance, represented by the Hamiltonian $H'(t)$; hence, the total Hamiltonian is given by

$$\mathscr{H}(t) = \begin{cases} H & t < t_0 \\ H + H'(t) & t \geq t_0 \end{cases} . \tag{3.2}$$

Nonequilibrium statistical mechanics deals with calculating expectation values for some physical observable $A_{\mathscr{H}}(t)$, given in the Heisenberg picture, for times $t \geq t_0$

$$\langle A_{\mathscr{H}}(t) \rangle = \mathrm{Tr}\left[\rho(H) A_{\mathscr{H}}(t)\right].$$

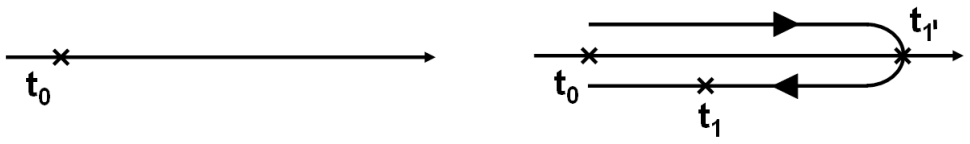

Figure 3.1: Left: standard time-ordering along a straight line. Right: time ordering along contour c. The "closed time path" starts and ends at time t_0 but introduces an upper and lower time branch each possessing different ordering directions. The contour passes through time point t_1 and $t_{1'}$ once.

A diagrammatic theory always requires one to take into account various time-orderings that can become quite complicated. The usual forward ordering $\overrightarrow{T}$ arranges operators, depending on their time argument, along the straight time line depicted in Figure 3.1 (left). To simplify the description of nonequilibrium systems, Keldysh introduced a very different kind of time-ordering. Instead of organizing along a straight line, the so called contour-ordering operator T_c orders operators according to the position of their time argument on the contour c which is depicted in Figure 3.1 (right). This contour starts and ends at t_0 and passes through t_1 and $t_{1'}$ once. It is important to note that this contour introduces two different time branches. This way, a time argument can reside either on the upper or on the lower branch of the contour.

Completely analogous to the standard single-particle Green's function [53], the so-called contour-ordered Green's function

$$G(1,1') = -i\langle T_c(\psi_{\mathscr{H}}(1)\psi^\dagger_{\mathscr{H}}(1'))\rangle \tag{3.3}$$

is introduced, where, in comparison to the standard version, only the time-ordering operator $\overrightarrow{T}$ is changed to the new contour-ordering operator T_c. We use the common abbreviation $1 \equiv (t_1, \mathbf{x}_1)$. $\psi(1)$ and $\psi^\dagger(1')$ refer to single particle field operators.

Given the field operators, we can formally define T_c as

$$T_c(\psi_{\mathscr{H}}(1)\psi^\dagger_{\mathscr{H}}(1')) \equiv \begin{cases} \psi_{\mathscr{H}}(1)\psi^\dagger_{\mathscr{H}}(1') & t_1 >_c t_{1'} \\ \pm\psi^\dagger_{\mathscr{H}}(1')\psi_{\mathscr{H}}(1) & t_1 <_c t_{1'} \end{cases},$$

where the contour ordering relation $t_1 >_c t_{1'}$ means t_1 is further along the contour than $t_{1'}$ like, for instance, depicted in Figure 3.1 (right). Like in case of usual Green's functions, due to their different commutation relations, we have to distinguish Bose (upper sign) and Fermi (lower sign) fields.

So far, purely formally, we have introduced a new type of time ordering T_c and a Green's function utilizing this new operator. Let us see why in case of nonequilibrium systems it is useful to do so. Although basically following Ref. [55], we will give some additional calculation steps and comments that might appear to be trivial once written down, yet may be very useful both to those new in the field and to understand the idea of contour-ordering.

We are interested in a diagrammatic expansion of the contour-ordered Green's function (3.3). First of all we note that the well-known transformation, relating an operator $A_{\mathscr{H}}$ in the Heisenberg picture to the corresponding one A_H in the interaction picture with

respect to H

$$A_{\mathscr{H}}(t) = u^\dagger(t,t_0) A_H(t) u(t,t_0)$$

with

$$u(t,t_0) = \overrightarrow{T} \exp\left[-i \int_{t_0}^{t} dt'\ H'_H(t')\right],$$

can be expressed using a time ordering along the contour c_t, shown in Figure 3.2 (left). This contour is designed such that it starts and ends at the initial time t_0 of the transformation $u(t,t_0)$. Additionally, the course of the contour changes from the upper to the lower branch at time t. We get

$$\begin{aligned} A_{\mathscr{H}}(t) &= u^\dagger(t,t_0) A_H(t) u(t,t_0) \\ &= \underbrace{\overleftarrow{T} \exp\left[-i \int_{t}^{t_0} dt'\ H'_H(t')\right]}_{\text{ordered lower branch } c_t} A_H(t) \underbrace{\overrightarrow{T} \exp\left[-i \int_{t_0}^{t} dt'\ H'_H(t')\right]}_{\text{ordered upper branch } c_t} \\ &= T_{c_t}\left[\exp\left(-i \textstyle\int_{c_t} d\tau\ H'_H(\tau)\right) A_H(t)\right]. \end{aligned} \tag{3.4}$$

This can be used to express the contour-ordered Green's function (3.3)

$$\begin{aligned} G(1,1') &= -i\langle T_c \left\{ \psi_{\mathscr{H}}(1) \psi^\dagger_{\mathscr{H}}(1') \right\} \rangle \\ &= -i\langle T_c \left\{ T_{c_t}\left[\exp\left(-i \textstyle\int_{c_t} d\tau\ H'_H(\tau)\right) \psi_H(1)\right] \right. \\ &\times \left. T_{c_{t'}}\left[\exp\left(-i \textstyle\int_{c'_t} d\tau\ H'_H(\tau)\right) \psi^\dagger_H(1')\right] \right\} \rangle \\ &= -i\langle T_c \left\{ S_c^H\ \psi_H(1) \psi^\dagger_H(1') \right\} \rangle, \end{aligned} \tag{3.5}$$

where in the final step we have taken care of the proper time-ordering T_c, combining the contours c_t and $c_{t'}$ into contour c, and abbreviated

$$S_c^H = \exp\left[-i \int_c d\tau\ H'_H(\tau)\right].$$

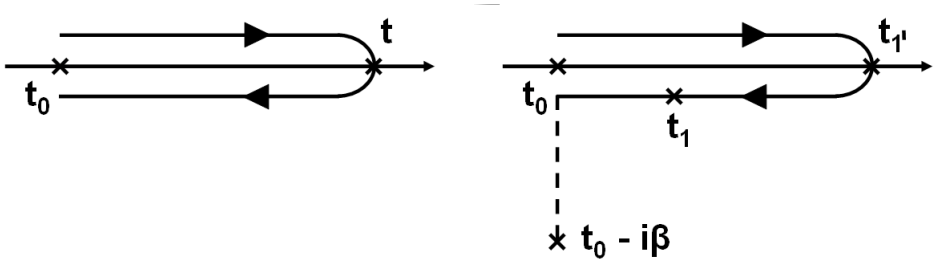

Figure 3.2: Left: contour c_t. The contour changes from upper to lower branch at time t. Right: contour c_i composed of the dotted and solid part. The dotted part formally arises due to the transformation to the interaction picture with respect to the single-particle Hamiltonian H_0

In Equation 3.5, the operators are given in the interaction picture with respect to the entire time-independent Hamiltonian $H = H_0 + H^i$, Equation 3.1. However, as the goal of the Keldysh formalism is to derive a diagrammatic expansion for nonequilibrium systems which is analogous to the usual Feynman technique in equilibrium, we wish to employ the standard, statistical Wick's theorem [56]. The usual diagrammatic expansion uses Wick's theorem to find Green's function expansions in terms of the single-particle propagator. Hence, in a final step, we have to transform to the interaction picture with respect to the free, single-particle Hamiltonian H_0, Equation 3.1.

Formally using $t - t_0 \equiv -i\beta$ and the standard relation [48]

$$\tilde{u}(t, t_0) = e^{-iH_0 t} \tilde{u}_I(t, t_0) e^{iH_0 t_0},$$

where

$$\tilde{u}_I(t, t_0) = \overrightarrow{T} \exp\left[-i \int_{t_0}^{t} dt' H^i_{H_0}(t')\right],$$

relating the time-evolution operator $\tilde{u}(t, t_0)$, due to Hamiltonian $H = H_0 + H^i$, to its representation in the interaction picture $\tilde{u}_I(t, t_0)$ with respect to H_0, we find the relation

$$e^{-\beta H} = e^{-\beta H_0}\ \tilde{u}_I(t_0 - i\beta, t_0).$$

Utilizing this expression, the contour-ordered Green's function can be written as

$$\begin{aligned} G(1, 1') &= -i \frac{\langle T_c \left\{ S_{c^i} S_c\ \psi_{H_0}(1) \psi^\dagger_{H_0}(1') \right\} \rangle_0}{\langle T_c \{ S_{c^i} S_c \} \rangle_0} \\ &\equiv -i \frac{\mathrm{Tr}\left[e^{-\beta H_0} T_c \left\{ S_{c^i} S_c\ \psi_{H_0}(1) \psi^\dagger_{H_0}(1') \right\} \right]}{\mathrm{Tr}\left[e^{-\beta H_0} T_c \{ S_{c^i} S_c \} \right]} \end{aligned} \tag{3.6}$$

with

$$S_{c^i} = \exp\left[-i \int_{c^i} d\tau\ H^i_{H_0}(\tau)\right],$$

$$S_c = \exp\left[-i \int_{c} d\tau H'_{H_0}(\tau)\right],$$

employing the contour c^i shown in Figure 3.2 (right).

Equation 3.6 is a remarkable result: it shows that equilibrium and nonequilibrium statistical mechanics are formally and structurally equivalent. We are left with an expression which is completely analogous to its counterpart in equilibrium theory and we can now use Wick's theorem, as usual, to get a perturbation expansion of the contour-ordered Green's function. The only, but essential, difference here is integration over a contour instead of the real time axis, and the modified time-ordering. Taking this into account, the contour-ordered Green's function is mapped onto its Feynman diagrams and rules exactly as in equilibrium theory. For instance, like stated by the *linked cluster theorem* the denominator in Equation 3.6 cancels all unlinked diagrams.

As we do not consider initial correlations, we let t_0 approach $-\infty$. It can be shown that, in this case, we can neglect the dotted part of the contour c_i, Figure 3.2 (right), proceeding from t_0 to $t_0 - i\beta$ which arose from the transformation of Equation 3.5 to the interaction

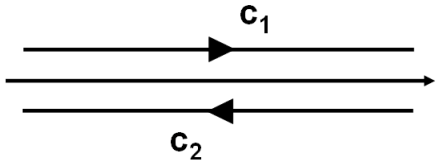

Figure 3.3: Keldysh contour c_K composed of upper branch c_1 proceeding from $-\infty$ to $+\infty$ and lower branch c_2 going from $+\infty$ to $-\infty$

picture with respect to the single-particle Hamiltonian H_0, see [55, 59]. Furthermore, due to the unitary of the time-evolution operator, we can expend the largest time to $+\infty$ and finally get the original Keldysh contour c_K, shown in Figure 3.3, which consists of an upper branch c_1 going from $-\infty$ to $+\infty$ and a lower branch c_2 going from $+\infty$ back to $-\infty$.

To enable the rather complicated time-ordering along c_K, the so-called *Keldysh space* is established which incorporates contour-ordering into a matrix structure. The contour-ordered Keldysh Green's function G_{c_K} is mapped onto this space

$$G_{c_K}(1,1') \mapsto \check{G} \equiv \begin{pmatrix} \check{G}_{11} & \check{G}_{12} \\ \check{G}_{21} & \check{G}_{22} \end{pmatrix}, \tag{3.7}$$

such that the ij component of $\check{G}$ corresponds to $G_{c_K}(1,1')$ in the case when t_1 and $t_{1'}$ are located on the contour branches c_i and c_j respectively. Within each component of $\check{G}$ it is now sufficient to use the usual time- $\overrightarrow{T}$ and inverse-time-ordering operator $\overleftarrow{T}$. For example, given $\check{G}_{11}(1,1')$, as both time argument t_1, $t_{1'}$ reside on the upper branch, going from $-\infty$ to $+\infty$, the field operators are ordered using $\overrightarrow{T}$. As the lower branch proceeds in the opposite direction, from $+\infty$ to $-\infty$, in $\check{G}_{22}(1,1')$ the standard inverse time-ordering $\overleftarrow{T}$ is used. By contrast, in $\check{G}_{12}(1,1')$ and $\check{G}_{21}(1,1')$, we do not need any ordering operator because, due to the fact that both times reside on different branches, it is immediately clear which argument is the first along the contour.

Finally, we remark that the components $\check{G}_{ij}$ are not linearly independent [54] and it is possible to transform $\check{G}$ into a triangular form in Keldysh space [55]

$$\underline{G} = \begin{pmatrix} G^R & G^K \\ 0 & G^A \end{pmatrix}.$$

This is important to note as different forms of the Keldysh Green's function can be found in the literature. We will explain the rotation axis used when performing calculations in Chapter 6 and Appendix B.1.

3.1.1 Coupling to an external potential

As a concrete example of how the contour ordering in Keldysh space is taken into account, we treat the simplest case of an external potential $U(t,\mathbf{x})$. The coupling of such a potential will be essential for calculating the full counting statistics of charge transport in the following chapters.

As mentioned before, the contour-ordered Green's function is mapped onto the same Feynman diagrams and rules as in equilibrium theory. Following the linked cluster theorem,

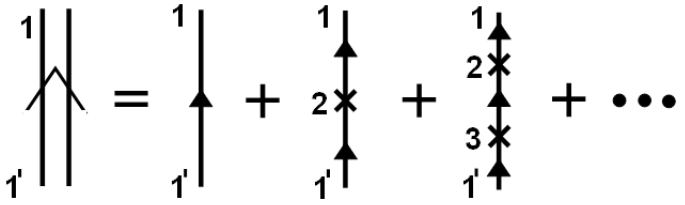

Figure 3.4: Diagrammatic expansion of G_{c_K} in the case of an external potential $U(t, \mathbf{x})$. A cross denotes interaction with the potential.

only connected diagrams are relevant and we find the simple standard diagrammatic expansion of G_{c_K} shown in Figure 3.4, see for example [52]. Using the Keldysh time-ordering, we find for the correction first-order in $U(t, \mathbf{x})$, i.e., second diagram in the expansion series,

$$G^{(1)}_{c_k}(1, 1') = \int d\mathbf{x}_2 \int_{c_K} d\tau_2 \; G^{(0)}_{c_K}(1, 2) \; U(2) \; G^{(0)}_{c_K}(2, 1').$$

We can map the contour integration onto the real time axis respecting the two different contour directions

$$\int_{c_K} d\tau \mapsto \int_{-\infty}^{\infty} dt - \int_{-\infty}^{\infty} dt.$$

Thus, in Keldysh space we find

$$\check{G}^{(1)}_{ij}(1, 1') = \int d\mathbf{x}_2 \int_{-\infty}^{\infty} dt_2 \left[\check{G}^{(0)}_{i1}(1, 2) U(2) \check{G}^{(0)}_{1j}(2, 1') - \check{G}^{(0)}_{i2}(1, 2) U(2) \check{G}^{(0)}_{2j}(2, 1') \right],$$

where the different indices originate from the two distinct cases where $U(t, \mathbf{x})$ either resides on the upper or on the lower branch of the contour. This can be rewritten as

$$\check{G}^{(1)}_{ij}(1, 1') = \int d\mathbf{x}_2 \int_{-\infty}^{\infty} dt_2 \; \check{G}^{(0)}_{ik}(1, 2) \; \check{U}_{kk'}(2) \; \check{G}^{(0)}_{k'j}(2, 1'),$$

where we use the Einstein summation convention and introduce

$$\check{U}_{ij}(2) = U(2) \tau^3_{ij}.$$

τ^i denote the set of Pauli matrices. Hence, we see that an external potential $U(t, \mathbf{x})$ couples to a particle in Keldysh space through a τ^3 matrix. Different couplings in Keldysh space, due to other interactions, can be found along similar lines and in general can lead to a tensor, e.g., for electron-phonon interaction. It will turn out that the coupling relevant for the FCS also has this simple τ^3 form.

3.2 Quasiclassical Approximation

Unfortunately, finding exact solutions for Green's functions in mesoscopic transport problems is almost impossible, thus simplifications and approximations seem to be always necessary. An important way to simplify the Green's function in a transport problem is via the quasiclassical approximation. This is a very well described theory and will not go into details here. Nevertheless, we will shortly summarize the essentials. For further details we refer to Ref. [60, 41].

3.2.1 Eilenberger and Usadel equation

The quasiclassical approximation uses the fact that most energy scales involved in transport are small compared to the Fermi energy. The Green's function, depending on two spatial coordinates, oscillates as a function of relative coordinate $|\mathbf{r} - \mathbf{r}'|$ on a scale of the Fermi wavelength λ_F. Typically this is much shorter than the characteristic length scales of the considered system, e.g., the superconducting coherence length ξ_0. Thus, for most systems it is sufficient to integrate out the dependence on the relative coordinate. Following this idea the equation of motion of the Green's function, see for example Ref. [41], can be reduced to the so-called *Eilenberger equation* [61], eliminating the complicated dependence on two coordinates.

Frequently, due to strong impurity scattering in the superconducting material, another important simplification arises, described by the so-called *dirty limit*, $l \ll \xi_0$, but still quasiclassical, i.e., $l \gg \lambda_F$, where l is the impurity mean free path. The requirement is that the self-energy term, see for instance [52, 56], of the Eilenberger equation is dominated by elastic impurity scattering. In this case the electron motion becomes diffusive and the Green's function will be nearly isotropic. By expanding the Green's function in spherical harmonics the Eilenberger equation can be further simplified to the so-called *Usadel equation* [62].

Chapter 4

Keldysh Green's function approach

In this chapter we will present how the Keldysh Green's function approach can be employed to calculate the cumulant generating function. The idea to apply the Keldysh technique to compute the full counting statistics was introduced by Nazarov in Ref. [40]. We began by laboriously learning this method from [40, 63, 47, 64]. Later, we found the very advisable short review given in Ref. [65]. Here, we will concentrate on presenting the central aspect of formally connecting the statistics to transport theory in terms of Green's functions. For details on utilizing methods to approximate the relevant Green's functions, such as the quasiclassical limit, we refer the reader to the well-elaborated theory and the references given in Section 3.2, i.e., Ref. [41, 60, 61, 62]

4.1 Extending FCS to the Keldysh contour

In Chapter 2 we saw that the cumulant generating function of charge transport can be calculated according to Equation 2.12 via

$$e^{S(\chi)} = \mathrm{Tr}_{System}\left[\overrightarrow{T}\, e^{-i\int_0^{t_0} dt\, [\hat{H}_{sys}+\frac{\chi}{2e}\hat{I}]}\, \hat{\rho}^{system}\ \overleftarrow{T}\, e^{i\int_0^{t_0} dt\, [\hat{H}_{sys}-\frac{\chi}{2e}\hat{I}]}\right], \tag{4.1}$$

where the general quantum mechanical operator $\hat{A}$ is now replaced by the current operator $\hat{I}/e$. For reasons becoming clear very soon, we would like to express this in terms of an expectation value using contour-time ordering, introduced in Section 3.1. Given time and inverse-time ordering in Equation 4.1, we could do so if the sign in front of the so-called *counting field* χ in the inverse-time-ordered exponential was changed. Therefore, we introduce a counting field that possesses two distinct signs on the upper and lower branch of the Keldysh contour, see Figure 4.1, which effectively results in two different Hamiltonians $H_{1(2)}$ on the respective contours,

$$H_{1(2)} = \hat{H}_{sys} + \frac{\chi_{1(2)}(t)}{2e}\hat{I} \quad \text{with} \quad \chi_{1(2)}(t) = \begin{cases} +\chi & t \in C_1 \\ -\chi & t \in C_2 \end{cases}. \tag{4.2}$$

Hence, the counting field is treated as a perturbation and we note that the current operator is coupled in Keldysh space exactly like an external potential, see Section 3.1.1. From the explanations on the Keldysh Green's function formalism in Section 3.1 it is clear that we can express the cumulant generating function as

$$e^{S(\chi)} = \langle T_{c_K} e^{-\frac{\chi}{2e}\int_{c_K} d\tau \hat{I}(\tau)}\rangle, \tag{4.3}$$

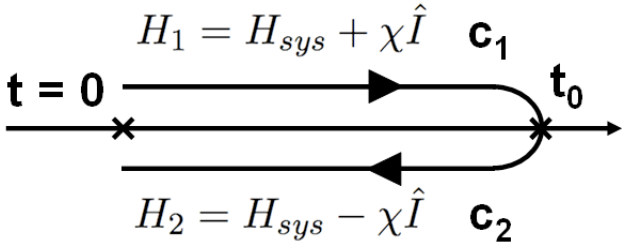

Figure 4.1: Counting field $\chi(t)$ possessing two different signs on the upper c_1 and lower c_2 branch of the Keldysh contour between 0 and t_0 that results in two different Hamiltonians $H_{1(2)}$

.

see for instance Equation 3.5. We note the curial role the Keldysh technique plays here to separate the perturbation, due to the counting field, from an arbitrary system Hamiltonian H_{sys}. In most references Equation 4.3 can be found as a starting point.

4.2 Relating CGF to Keldysh Green's functions

With Equation 4.3 we have related the cumulant generating function to a nonequilibrium system treated in terms of a Keldysh contour. The counting field couples in Keldysh space like an external potential. The next step is to connect this to accessible field-theoretical quantities. For this reason we rewrite the system Hamiltonian

$$\hat{H}_{sys} = \int d\mathbf{x}\ \hat{\psi}^\dagger(\mathbf{x})\hat{h}_{sys}(\mathbf{x})\hat{\psi}(\mathbf{x}),$$

and the time-dependent perturbation

$$\frac{\chi}{2e}\hat{I}(t) = \pm\frac{\chi}{2e}\int d\mathbf{x}\ \hat{\psi}^\dagger(\mathbf{x},t)\hat{j}(\mathbf{x})\hat{\psi}(\mathbf{x},t), \tag{4.4}$$

in terms of the usual field operators $\hat{\psi}^\dagger$ and $\hat{\psi}$. $\hat{h}_{sys}$ is the usual single-particle Hamiltonian of the system. Therewith, we formulate the equation of motion, see for example Ref. [41], for the counting field-dependent, contour-ordered Green's function $\check{G}(1,1';\chi)$ using Keldysh space

$$\left[i\frac{\partial}{\partial t} - \hat{h}_{sys}(\mathbf{x}) + \frac{\chi}{2e}\,\tau^3\,\hat{j}(\mathbf{x})\right]\check{G}(1,1';\chi) = \delta(1-1'). \tag{4.5}$$

Here $\hat{j}(\mathbf{x})$ denotes the current density operator and, as seen in Section 3.1.1, it has to be coupled by a τ^3 Pauli matrix.

Given the Green's function $\check{G}(1,1';\chi)$ as solution of Equation 4.5 it is straightforward to calculate the current which now depends on the counting field χ and thus is called the *counting current*,

$$I(\chi,t) = \int d\mathbf{x}\ \mathrm{Tr}\left[\tau^3\,\hat{j}(\mathbf{x})\check{G}(1,1';\chi)\right]\Big|_{1\to 1'}. \tag{4.6}$$

Additionally, in comparison to standard Green's functions, in Equation 4.6 we have to mind the Keldysh space structure leading to the additional τ^3 matrix and the trace with respect

to its components. The usual current density operator is given by

$$\hat{j}(\mathbf{x}) = (\nabla F(\mathbf{x})) \lim_{\mathbf{x}\to\mathbf{x}'} \frac{ie}{2m}(\nabla_{\mathbf{x}} - \nabla_{\mathbf{x}'}), \tag{4.7}$$

where $F(\mathbf{x})$ is designed such that we obtain the current flowing through a cross-section c as depicted in Figure 4.2.

By virtue of the discussion in Chapter 3, we can directly write down the expansion of the Green's function defined by Equation 4.5. Its diagrams are shown in Figure 3.4. Taking into account Equation 4.4, we get

$$\begin{aligned} G(1,1';\chi) &= -i\sum_{n=0}^{\infty} \tfrac{1}{n!}\left(-i\tfrac{\chi}{2e}\right)^n \int_{c_K} d\tau_1 \cdots \int_{c_K} d\tau_n \\ &\times \langle T_{c_K} \psi(\mathbf{x},t)\psi^\dagger(\mathbf{x}',t')\hat{I}(\tau_1)\hat{I}(\tau_2)\cdots\hat{I}(\tau_n)\rangle_{connected}, \end{aligned} \tag{4.8}$$

where again we use the standard diagram technique replacing usual by contour time-ordering. Disconnected diagrams are canceled due to the linked cluster theorem. Utilizing Equation 4.6, we calculate the current

$$\begin{aligned} I(\chi,t) &= -\sum_{n=1}^{n=\infty} \tfrac{1}{(n-1)!}\left(-i\tfrac{\chi}{2e}\right)^{n-1} \int_{c_K} d\tau_1 \cdots \int_{c_K} d\tau_{n-1} \\ &\times \langle T_{c_K} \hat{I}(\tau_1)\hat{I}(\tau_2)\cdots\hat{I}(\tau_{n-1})\hat{I}(t)\rangle_{connected}. \end{aligned} \tag{4.9}$$

Expansion 4.9 is the field-theoretical quantity the cumulant generating function will be connected to.

To make this connection, we write down the power series of the exponential function in Equation 4.3

$$e^{S(\chi)} = \sum_{n=0}^{\infty} \frac{1}{n!}\left(-i\frac{\chi}{2e}\right)^n \int_{c_K} d\tau_1 \cdots \int_{c_K} d\tau_n \langle T_{c_K} \hat{I}(\tau_1)\hat{I}(\tau_2)\cdots\hat{I}(\tau_n)\rangle. \tag{4.10}$$

The crucial difference, in contrast to the Green's function in Equation 4.8, is that here also unconnected diagrams occur. There is no cancelation of unlinked graphs. Thus to connect

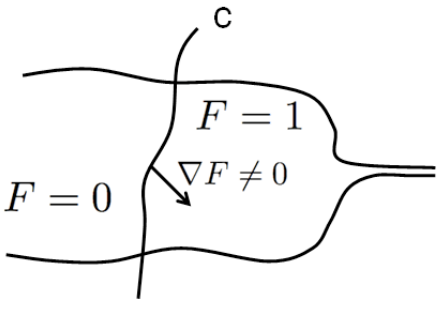

Figure 4.2: Schematic picture of a terminal with a cross-section c through which charge transport is calculated. The cross-section function $F(\mathbf{x})$ is 0 on the left and 1 on the right of c and changes on a certain length scale such that, its gradient is nonzero and perpendicular to the separating surface.

the cumulant generating function with the counting current we are left with a standard combinatoric problem of counting the number of connected graphs possessing n vertices contained in the diagram sum in Equation 4.10. The result can be expressed in another exponential series

$$\begin{aligned} \exp\left[S(\chi)\right] &= \exp\Big[\textstyle\sum_{n=1}^{\infty}\frac{1}{n!}\left(-i\frac{\chi}{2e}\right)^n\int_{c_K}d\tau_1\cdots\int_{c_K}d\tau_n \\ &\times \quad \langle T_{c_K}\hat{I}(\tau_1)\hat{I}(\tau_2)\cdots\hat{I}(\tau_{n-1})\hat{I}(t)\rangle_{connected}\Big]. \end{aligned} \tag{4.11}$$

By integrating the time argument of $I(\chi,t)$ in Equation 4.9 over the Keldysh contour between $t=0$ and $t=t_0$, using $\int_{c_K}d\tau\ I(\chi,\tau)=2\int_0^{t_0}dt\ I(\chi,t)$ and matching it with the expression for the cumulant generating function $S(\chi)$, resulting from Equation 4.11, we finally obtain the essential result

$$\frac{\partial}{\partial\chi}S(\chi)=\frac{i}{e}\int_0^{t_0}dt\ I(\chi,t). \tag{4.12}$$

It relates the cumulant generating function to the counting current. Once the Green's function $\check{G}(1,1';\chi)$ (Equation 4.5) is known the counting current (Equation 4.6) provides the desired accessible field-theoretical quantity. Unfortunately, finding exact solutions for such Green's functions is almost impossible and approximations have to be used. In the rest of this chapter we will deal with the question: how to find $\check{G}(1,1';\chi)$.

4.3 Counting field as a modified boundary condition

The first step towards dealing with the Green's function $\check{G}(1,1';\chi)$ is to address the perturbation, due to the counting field $\frac{\chi}{2e}\tau^3\hat{j}(\mathbf{x})$, in the equation of motion (4.5). The incentive will be to find a transformation to relate the general solution to the $\chi=0$ case. This way, the counting field drops out the calculation and we are "only" left with the problem of finding the Green's function of the system described by H_{sys}, see Equation 4.2.

Let us consider for a moment a charged particle in a vector potential $\mathbf{A}(\mathbf{x})$ leading to the Hamiltonian

$$H=\int d\mathbf{x}\ \psi^\dagger(\mathbf{x})\left[\frac{(\mathbf{p}-e\mathbf{A})^2}{2m}\right]\psi(\mathbf{x}).$$

Taking into account $[\mathbf{p},\mathbf{A}(\mathbf{x})]\neq 0$, utilizing the position space representation of $\mathbf{p}$ and neglecting the term quadratic in $\mathbf{A}(\mathbf{x})$, we can write down the perturbation H' due to the vector potential as

$$\begin{aligned} H' &= -\tfrac{e}{2m}\textstyle\int d\mathbf{x}\ \psi^\dagger(\mathbf{x})\left[\mathbf{p}\mathbf{A}+\mathbf{A}\mathbf{p}\right]\psi(\mathbf{x}) \\ &= \textstyle\int d\mathbf{x}\ \mathbf{A}(\mathbf{x})\cdot\left[\frac{ie}{2m}\left(\psi^\dagger\nabla\psi-(\nabla\psi^\dagger)\psi\right)\right]. \end{aligned} \tag{4.13}$$

In our case, the perturbing Hamiltonian is given by Equation 4.4. We rewrite this in Keldysh space using τ^3 and the representation of the current density operator in Equation 4.7

$$H'=\tau^3\int d\mathbf{x}\ \frac{\chi}{2e}\nabla F(\mathbf{x})\cdot\left[\frac{ie}{2m}\left(\psi^\dagger\nabla\psi-(\nabla\psi^\dagger)\psi\right)\right].$$

Comparison with Equation 4.13 suggests that we can incorporate the counting field into a gauge like transformation [48]

$$\mathbf{A}\rightarrow\mathbf{A}+\nabla\Lambda$$

with

$$\Lambda = \frac{\chi}{2e} F(\mathbf{x}) \tau^3.$$

This would yield a rotation in Keldysh space

$$\mathscr{G} = \exp\left[i \frac{\chi}{2} \tau^3 \right], \tag{4.14}$$

where in the argument of the exponential (Equation 4.14), we assumed that we can choose a point $\mathbf{x}$ on the right of the cross-section c in Figure 4.2, where $F(\mathbf{x}) = 1$. Here, in this simple, motivating analogy, this step cannot be further justified. It turns out that, under very general approximations of the Green's function (4.5), Equation 4.14 is indeed the correct transformation. Needless to say, the comparison to the perturbation due to a vector potential is not a rigorous proof. Nevertheless, we think this is a very accessible way to illustrate the essential idea.

To get this result formally, we have to go through the steps explained in [65]: Assuming adequate conditions for the length scale on which the cross-section function $F(\mathbf{x})$ changes from 0 to 1, we can derive a quasiclassical version of the equation of motion (4.5). Given the Eilenberger equation, see Section 3.2.1, it formally follows that the counting field can be eliminated transforming its solution $\check{g}(\mathbf{x}, \mathbf{v}_F, t, t', \chi)$ by

$$\check{g}(\mathbf{x}, \mathbf{v}_F, t, t', \chi) = e^{-i\chi F(\mathbf{x})\tau^3/2}\, \check{g}(\mathbf{x}, \mathbf{v}_F, t, t', 0)\, e^{i\chi F(\mathbf{x})\tau^3/2}.$$

Finally, we assume the electrons are counted through a cross-section of a terminal where the dirty limit, $l \ll \xi_0$ but $l \gg \lambda_F$ (see Section 3.2.1), is applicable. Hence, the Green's function becomes constant in position and isotropic in momentum space. This finally supplies the opportunity to consider a point on the right of the cross-section c in Figure 4.2, where $F(\mathbf{x})$=1. Diffusive approximation and Usadel Equation in the terminal provide

$$\check{G}(\chi) = e^{-i\chi\tau^3/2}\, \check{G}(0)\, e^{i\chi\tau^3/2}. \tag{4.15}$$

This is exactly the same transformation as in Equation 4.14 that we motivated heuristically.

To summarize this crucial fact, we see that we can completely incorporate the counting field into a *modified boundary condition*. We can easily count electrons in one of the terminals and the counting field is then simply introduced by the rotation in Keldysh space (4.15).

4.4 Circuit Theory

In the previous sections of this chapter we have seen how to relate the cumulant generating function to the counting field-dependent counting current (4.6) and that, in the case when electron counting is accomplished within one of the terminals, we can incorporate the counting field into a modified boundary condition utilizing the gauge-like transformation (4.15). All this is necessary to handle charge counting and its statistics. Nevertheless, it does not solve or simplify the general transport problem posed by the system Hamiltonian $\hat{H}_{sys}$. Hence, to complete our task, we need an approach that describes transport given the equation of motion (4.5) in the case $\chi = 0$. Additionally, this theory must respect the full Keldysh space matrix structure such that rotations in this space, see Equation 4.15, can be performed. This request is particularly important with respect to the remark given in Section 3.1, that the components of the Keldysh Green's function's matrix representation are not linearly

independent. A theory that uses this source of simplification will not be general enough to handle the counting field introduced by Equation 4.15.

The Circuit Theory of mesoscopic transport introduced by Nazarov in Ref. [66, 67] fulfills this requirement. It originated from the attempt to introduce an appliciable formulation of the adequate, extensive theory of nonequilibrium superconductivity which is given in terms of the quaisclassical and dirty limit approximation, see for instance Ref. [68, 69]. An overview of this well elaborated theory as well as the important extension of introducing an arbitrary connector is given in Ref. [70]. We briefly summarize the points that will be important for us here.

The central idea of this theory is to describe a mesoscopic device by discrete elements similar to the approach used in Kirchhoff's classical circuit theory. A specific device will be arbitrarily well approximated depending on the number of chosen elements. Formally this is achieved by formulating a discrete version of the relevant Usadel equation, see Section 3.2.1. The current is described by a *matrix current* in terms of Green's functions analogous to Equation 4.6. Following this approach, a circuit is subdivided into three kinds of elements: terminals, nodes and connectors. Terminals set boundary conditions on both, thermodynamic quantities (voltage, temperature etc.) and material properties (normal metal vs. superconductor etc.). Nodes refer to the approximate discreteness. Their Green's functions have to be determined using quasiclassical normalization conditions $\check{G}^2 = 1$ and matrix current conservation, taking into account individual connectors between particular nodes.

The crucial element in this theory is the *arbitrary connector* given by a set of transmission eigenvalues $\{T_n\}$. Given the Green's functions $\check{G}_{1(2)}(t,t')$, on the right and the left of the contact, the matrix current is given by

$$\check{I}(t,t') = -\frac{e^2}{\pi}\sum_n \frac{2T_n\,[\check{G}_1 \overset{\otimes}{,} \check{G}_2]}{4 + T_n\,\left(\{\check{G}_1 \overset{\otimes}{,} \check{G}_2\} - 2\right)}, \tag{4.16}$$

where in case of two explicit time arguments $\otimes$ denotes a convolution over the intermediate time $(A\otimes B)(t,t') = \int dt''\, A(t,t'')B(t'',t')$. From matrix current $\check{I}(t,t')$ the current is obtained by

$$I(t) = \frac{1}{4e}\mathrm{Tr}[\tau^3\check{I}(t,t)],$$

analogous to Equation 4.6. It is essential to note that the matrix current in Equation 4.16 is derived by using quasiclassical Zaitsev boundary conditions which properly describe boundaries between metals, see Ref. [71].

4.5 Model summery

We can now concretize the model describing the Josephson junction under investigation. We consider two superconducting terminals in the zero temperature limit $T = 0K$, setting a given voltage bias as the boundary condition. The oxide layer separating the two superconductors is treated as a constriction incorporated by a scatterer which is characterized by a set of transmission eigenvalues $\{T_n\}$. This set will comprise values $T \ll 1$, referring to usual tunnel transmission channels, and pinholes with eigenvalues close to unity. This model is connected to the physics of single mode contacts but, because the tunneling channels combined give a large contribution to the total conductance, is markedly distinct.

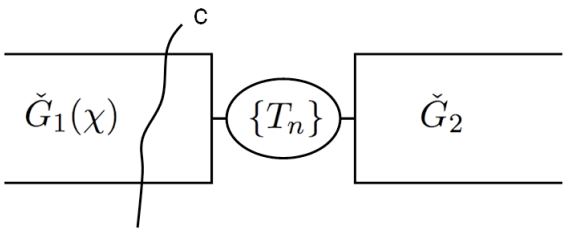

Figure 4.3: Schematic diagram of the modeled Josephson junction consisting of two superconducting terminals and a separating oxide layer which is characterized by a set of transmission eignevalues $\{T_n\}$. The counting field χ counting electrons passing through cross-section c can be incorporated into Green's function $\check{G}_1$.

The oxide layer is much short than the superconducting coherence length. Thus, the proper equivalent circuit using circuit theory is just an arbitrary connector with transmission eigenvalues $\{T_n\}$, connecting the two superconducting terminals, see Figure 4.3. The terminal Green's functions are given in terms of their bulk solutions, see [41] and Appendix A.2.

So finally, by performing electron counting in one of the terminals, we incorporate the counting field into the Green's function $\check{G}_1$ (4.15) and can use the resulting matrix current (4.16) to calculate the cumulant generating function (4.12).

Chapter 5

CGF normal conducting case

To get familiar with calculations which use the Keldysh Green's function technique, we calculated the cumulant generating function in the case of two normal conducting terminals, see Figure 4.3. Although the properties of a normal conducting quantum point contact are well known, we nevertheless briefly mention this case to appreciate its simplicity, and to put emphasis on the complications arising when dealing with the superconducting case.

For normal conducting reservoirs, following the steps described in Section 4.5, and by using energy instead of time representation of the Green's functions, we can write down the cumulant generating function, see [47, 65],

$$S(\chi) = \frac{t_0}{2\pi} \sum_n \int dE \ \mathrm{Tr} \ \ln \left[1 + \frac{T_n}{4} (\{\check{G}_1(\chi), \check{G}_2\} - 2) \right], \tag{5.1}$$

where the trace only refers to the components of the Keldysh space and we just have matrix products between the Green's functions given at fixed energy E. We get

$$S(\chi) = \frac{e t_0 V}{\pi} \sum_n \ln \left[1 + T_n (e^{i\chi} - 1) \right], \tag{5.2}$$

where $\mu_1 - \mu_2 = eV \geq 0$ is the potential difference between the two normal conducting terminals (see Appendix B.1 for clarification on some details of the calculation). With Equation 5.2 we reproduced the well known result which statistics for a single-mode contact with transmission T is binomial

$$P_{t_0}(N) = \left(\begin{array}{c} M \\ N \end{array} \right) T^N (1-T)^{M-N},$$

defining the number of attempts $M = et_0V/\pi$. The second cumulant can be related to the noise power (Chapter 8). Using Equation 5.2 we find exactly the standard shot noise formula [4]

$$S_I = \frac{2e^3 V}{\pi} \sum_n T_n (1 - T_n).$$

Equation 5.2 is one of the first results on full counting statistics in mesoscopic solid-state systems [44] and can be understood as one of the starting points of this theory. Although its calculation using Keldysh technique already involves some algebra, it is extremely simplified, due to the fact that the normal conducting terminal Green's functions only depends on the

difference of its time arguments $\check{G}(t,t') = \check{G}(t-t')$. Hence, in energy representation these Green's functions become diagonal $\check{G}(E,E') = \check{G}(E)\delta(E-E')$, see Appendix A.1, and we can find an expression like Equation 5.1 involving only a single energy integral and simple matrix multiplication of Keldysh Green's functions at a fixed energy E. Even though, by taking into account superconductivity, the terminal Green's functions become more complicated, the cumulant generating function for this contact, assuming equilibrium, can still be expressed by Equation 5.1. In fact, formula (5.1) was at first derived for such a superconducting contact, see Ref. [47].

However, considering the system of a voltage-biased Josephson junction, in which we are interested here, the ac Josephson effect, see for instance [72], gives rise to time-dependent currents and due to the Josephson relation $(\partial/\partial t)\phi(t) = 2eV/\hbar$ the terminal Green's function will depend on both time arguments independently, $\check{G}(t,t') \neq \check{G}(t-t')$, see Chapter 6. This will introduce a major complication that can not be circumvented as is possible, for example, in case of an Andreev SN contact, where we can set the energy offset such that the superconductor is at zero chemical potential for all times.

We will discuss how to treat this complication in the following chapter.

Chapter 6

CGF superconducting case

6.1 Nambu formalism

Superconductivity is one of the great areas of interest in many-body physics. Without question, the BCS theory, celebrating its 50 year jubilee this year, counts to one of the great theoretical highlights in this field. Although diagrammatic expansion techniques have been especially invented for dealing with such many-body systems, it turns out that, in the superconducting case, the usual graphical method using the ordinary propagator $G(1,1') = -i\langle T(\psi(1)\psi^\dagger(1'))\rangle$ is not sufficient. In fact, the expansion of the propagator creates classes of diagrams that cause an unstable diagram sum, see for instance Ref. [56]. These diagrams involve scattering of pairs of particles with momentum equal in magnitude but opposite in direction, i.e., Cooper pairs.

The fact, that the BCS theory, see Ref.[24], provides the superconducting state by introducing a paired superconducting wave function, suggests that, in order to treat superconductivity, the pairing interaction has to be made compatible with the standard Feynman diagrammatic method. To do so, Nambu introduced the pseudospinor creation and annihilation operator, see Ref. [52, 73],

$$\psi_k = \begin{pmatrix} \psi_{k\uparrow} \\ \psi^\dagger_{-k\downarrow} \end{pmatrix} \qquad \psi^\dagger_k = \begin{pmatrix} \psi^\dagger_{k\uparrow} & \psi_{-k\downarrow} \end{pmatrix}$$

and used it to define a matrix propagator

$$\begin{aligned} \bar{G}(k;t) &= -i\langle T\{\psi_k(t)\psi^\dagger_k(0)\}\rangle \\ &= -i \begin{pmatrix} \langle T\{\psi_{k\uparrow}(t)\psi^\dagger_{k\uparrow}(0)\}\rangle & \langle T\{\psi_{k\uparrow}(t)\psi_{-k\downarrow}(0)\}\rangle \\ \langle T\{\psi^\dagger_{-k\downarrow}(t)\psi^\dagger_{k\uparrow}(0)\}\rangle & \langle T\{\psi^\dagger_{-k\downarrow}(t)\psi_{-k\downarrow}(0)\}\rangle \end{pmatrix} \\ &= -i \begin{pmatrix} G(k\uparrow,t) & F(k,t) \\ F'(k,t) & -G(-k\downarrow,-t) \end{pmatrix}, \end{aligned} \tag{6.1}$$

where index k refers to momentum state $|k\rangle$, T denotes usual time ordering and the Green's function is given in its momentum representation.

The matrix propagator should not be confused with the Keldysh space representation in Section 3.1. By introducing the *anomalous propagators* F, F' (which give the probability

amplitude for creation and destruction of Cooper pairs) in addition to the ordinary propagator G, superconductivity can be treated by the usual diagrammatic technique. The only additional feature of the Feynman rules is to interpret Green's functions in this particle-hole or Nambu space, represented by the component of the matrix propagator (6.1). In case of nonequilibrium treated in terms of Keldysh Green's functions, each Kelysh component is then naturally represented by a matrix propagator in Nambu space. The components can be seen as the electron and hole components of pair correlations.

Coming back to the calculation of the cumulant generating function in the superconducting case, we can utilize Green's functions $\check{G}$ using both Keldysh and Nambu formalism. The Green's function in this Keldsh($^\wedge$)-Nambu($^-$) space will be represented by 4×4 matrices, and the approach presented in Chapter 4 completely takes over. The only change that must be made is to add another $\bar{\sigma}^3$ Pauli matrix to the current density operator in Equation 4.7, to account for the particle-hole structure in Nambu space, see Ref. [41]. Hence, the equation of motion 4.5 becomes

$$\left[i\frac{\partial}{\partial t} - \hat{h}_{sys}(\mathbf{x}) + \frac{\chi}{2e}\, \check{\tau}_k\, \hat{j}(\mathbf{x}) \right] \check{G}(1,1';\chi) = \delta(1-1'),$$

where we introduce $\check{\tau}_k = \bar{\sigma}^3\hat{\tau}^3$. Note that there is no matrix product between $\bar{\sigma}^3$ and $\hat{\tau}^3$ as they operate in different spaces. The counting field transformation 4.15 becomes

$$\check{G}(\chi) = e^{-i\chi\check{\tau}_k/2}\, \check{G}(0)\, e^{i\chi\check{\tau}_k/2}. \tag{6.2}$$

For details on the quasiclassical Green's function description in the superconducting case see Ref. [41].

6.2 Voltage-biased Josephson junction

Finally, after introducing the methods and techniques above, we are able to discuss how to calculate the cumulant generating function of a voltage-biased Josephson junction, modeled according to Section 4.5. The case of a single-mode superconducting quantum point contact with arbitrary transmission T was addressed in Ref. [37, 74]. To generalize this to a junction containing multiple transport channels characterized by a set of transmission eigenvalues $\{T_n\}$, we have to consider this set by a sum over individual channels within the matrix current of an arbitrary connector given in Equation 4.16. Basically, we will follow Ref. [74] adding some additional notes and calculation steps. Unfortunately, to our understanding, there were some misprints that hindered understanding of the details of the calculation. To improve the accessibility we will give some additional notes in Appendix B.2.

We are facing two voltage-biased terminals, see Figure 4.3, that are described by Keldysh-Nambu Green's functions $\check{G}_{1(2)}$. We set the chemical potential of the right Green's function $\check{G}_2$ to zero and incorporate the constant voltage bias V completely into $\check{G}_1$. Hence, we have $\check{G}_2 = \check{G}_S(t-t')$, where $\check{G}_S$ is the Green's function of a superconducting reservoir given by

$$\check{G}_S(t-t') = \int dE\, \check{G}_S(E) e^{E(t-t')} \tag{6.3}$$

$$\check{G}_S(E) = \begin{pmatrix} (\bar{A}-\bar{R})f + \bar{R} & (\bar{A}-\bar{R})f \\ (\bar{A}-\bar{R}(1-f) & (\bar{R}-\bar{A})f + \bar{A} \end{pmatrix},$$

$f(E)$ is the Fermi function. $\bar{R}$, $\bar{A}$ denote the retarded and advanced Green's function respectively, each possessing Nambu structure $\bar{R}, \bar{A} = g^{R,A}\bar{\tau^3} + f^{R,A}\bar{\tau^1}$, see Ref. [41] and Appendix A.2.

Given the phase ϕ_0, the BCS wave function [24], is given by

$$\Psi = \prod_k (u_k + v_k e^{i\phi_0}\psi_k^\dagger \psi_{-k}^\dagger).$$

The voltage bias at one electrode can be considered by a gauge transformation on each electron state $\psi_k^\dagger \to e^{i(e/\hbar)\int dt\, V}\psi_k^\dagger$

$$\Psi \to \prod_k (u_k + v_k e^{i[\phi_0 + (2eV/\hbar)t]}\psi_k^\dagger \psi_{-k}^\dagger)$$

Taking into account the Nambu structure, we can thus write for the left terminal Green's function

$$\check{G}_1(t,t') = e^{i\phi(t)\bar{\sigma}^3/2}\check{G}_S(t-t')e^{-i\phi(t')\bar{\sigma}^3/2}, \tag{6.4}$$

where $\phi(t) = \phi_0 + (2eV/\hbar)t$ is the time-dependent phase difference. Note that Equation 6.4 is a rotation solely in Nambu space. Incorporating the counting field into the left terminal via Equation 6.2, we find

$$\check{G}_1(\chi;t,t') = e^{-i\chi\check{\tau}_k/2}\check{G}_1(t,t')e^{i\chi\check{\tau}_k/2} \tag{6.5}$$

Using the time dependence of these Green's functions it can be shown that the counting current can be expressed in the following Fourier series

$$I(\chi,t) = \sum_n I_n(\chi)e^{in\phi(t)}.$$

Thus, the current oscillates with the harmonics of the Josephson frequency, whereas, the coefficients $I_n(\chi)$ are independent of the dc part of the superconducting phase ϕ_0. This is a crucial point as it helps us to circumvent the interpretation problems of the full counting statistics discussed in Chapter 2 that arise in the superconducting case. $I(\chi,t)$ enters further calculations of the cumulant generating function via Equation 4.12, i.e., integrated over its time argument. Thus, if we restrict ourselves to measurement times t_0, much longer than the inverse of the Josephson frequency, or to say to the *dc part of the cumulant generating function*, ϕ_0 drops out the calculation and thus we can set $\phi_0 = 0$. The gauge transformation mentioned in Chapter 2 still applies such that Equation 2.10 does not depend on x. Only in this way is the cumulant generating function free of the problem related to the broken gauge invariance in the mean field sense of BSC theory, discussed in Chapter 2. Thus, we obtain a classical, and therefore accessible, interpretation of the full counting statistics, free of the problem of "negative probabilities", see Ref. [47] and Chapter 2. Note that by writing down Equation 2.12 this was already used.

Using the matrix current of an arbitrary connector (4.16) with a given set of transmission eigenvalues $\{T_n\}$, and, as explained above, neglecting the oscillating terms of the counting current, we can integrate Equation 4.12 to find the expression

$$S(\chi) = \frac{t_0}{h}\sum_n \mathrm{Tr}\ln\left(1 + \frac{T_n}{4}\left[\{\check{G}_1(\chi), \check{G}_2\}_\otimes - 2\right]\right), \tag{6.6}$$

where in energy representation $\otimes$ denotes a convolution of the Green's functions over the internal energy agrument

$$(G_1 \otimes G_2)(E, E') = \int dE_1 \; G_1(E, E_1) G_2(E_1, E').$$

Additionally, the trace here does not only run over Keldysh-Nambu space but also includes a trace over the energy arguments. It is crucial that, in contrast to Equation 5.1, where in the normal conducting case we had a simple energy integral and the trace only referred to the Keldysh-Nambu space, we now have to account for off-diagonal elements of the Green's function $\check{G}_1(\chi)$ in energy space, because of the two independent time arguments, see Equation 6.4. Using the normalization condition of the time-dependent Green's function, $\check{G} \otimes \check{G} = \delta(t - t')$, see Ref. [41], and the expression $\mathrm{Tr} \ln \check{\mathrm{A}} = \ln \det \check{\mathrm{A}}$, we can express Equation 6.6 as

$$S(\chi) = \frac{2t_0}{h} \sum_n \ln \det \check{Q}_n,$$

where

$$\check{Q}_n = 1 + \frac{\sqrt{T_n}}{2} \left(\check{G}_1(\chi) - \check{G}_2 \right)$$

is a matrix in both Keldysh and Nambu space. Thus we are left to calculate the determinant of an infinite matrix and hence we have to take a closer look at $\check{G}_{1(2)}(E, E')$ including its Keldysh-Nambu structure.

The reservoir Green's function $\check{G}_S$, Equation 6.3, is diagonal in energy space. Given $\check{G}_S(t - t')$, by the components of its Keldysh-Nambu matrix representation $[\check{G}_S(t - t')]_{ij}$ we write Equation 6.4 in matrix form

$$\check{G}_1(t, t') = \begin{pmatrix} \begin{pmatrix} e^{ieV/\hbar(t-t')}[\check{G}_S(t-t')]_{11} & e^{ieV/\hbar(t+t')}[\check{G}_S(t-t')]_{12} \\ e^{-ieV/\hbar(t+t')}[\check{G}_S(t-t')]_{21} & e^{-ieV/\hbar(t-t')}[\check{G}_S(t-t')]_{22} \end{pmatrix} & (\cdots) \\ (\cdots) & (\cdots) \end{pmatrix},$$

where we indicated each Nambu matrix propagator, that is placed for the individual Keldysh components, by brackets. As (6.4) is a rotation only in Nambu space, all other Keldysh components denoted by $(\cdots)$ pick up the same distribution of $e^{\pm ieV/\hbar(t \pm t')}$ exponentials in their Nambu components. By applying a Fourier transformation to transform to energy representation, we get

$$\check{G}_1(E, E') = \begin{pmatrix} \begin{pmatrix} [\check{G}_S(E - eV)]_{11} \, \delta(E - E') & [\check{G}_S(E - eV)]_{12} \, \delta(E - E' + 2eV) \\ [\check{G}_S(E + eV)]_{21} \, \delta(E - E' - 2eV) & [\check{G}_S(E + eV)]_{22} \, \delta(E - E') \end{pmatrix} & (\cdots) \\ (\cdots) & (\cdots) \end{pmatrix}. \tag{6.7}$$

Thus, in energy space $\check{G}_1(E, E')$ possesses diagonal and off-diagonal elements in a tridiagonal form. Note that the energy argument of the upper Nambu row is lowered by eV and the lower row is increased by the same amount. Physically this becomes clear if we imagine the upper and lower row in Numbu space characterizing electron and hole character, respectively (see Equation 6.1). Furthermore, to introduce the counting field, we rotate in Keldysh-Nambu space following Equation 6.5. Of course this will not change the structure in energy space.

Having calculated $\check{G}_{1(2)}$ and understood the structure of each in energy space, we can restrict ourself to the energy interval $(E-E') \in [0, eV]$ and express $\check{Q}_n$ using the notation $[\check{Q}_n]_{k,l} = \check{Q}_n(E+keV, E+leV)$ as

$$\check{Q}_n = \begin{pmatrix} \ddots & \ddots & \ddots & \check{0} & & & \\ & [\check{Q}_n]_{-2,-4} & [\check{Q}_n]_{-2,-2} & [\check{Q}_n]_{-2,0} & \check{0} & & \\ & \check{0} & [\check{Q}_n]_{0,-2} & [\check{Q}_n]_{0,0} & [\check{Q}_n]_{0,2} & \check{0} & \\ & & \check{0} & [\check{Q}_n]_{2,0} & [\check{Q}_n]_{2,2} & [\check{Q}_n]_{2,4} & \\ & & & \check{0} & \ddots & \ddots & \ddots \end{pmatrix} \tag{6.8}$$

and the cumulant generating function becomes $S(\chi) = (2t_0)/h) \sum_n \int_0^{eV} dE \ \ln\det \check{Q}_n$. Using the bulk solution (6.3) we can easily write down $[\check{Q}_n]_{k,k}$, $[\check{Q}_n]_{k,k+2}$ and $[\check{Q}_n]_{k,k-2}$ in terms of the counting field χ and the advanced and retarded Green's functions $g^{R,A}$ and $f^{R,A}$. These 4×4 matrices can be found in Ref. [74]. However note the misprint in $\check{Q}_{n,n}$ where it should be $[\check{Q}_{n,n}]_{22} = \rho_n - \rho_{n-1} + g_n^R - g_{n-1}^R$ in the paper's notation. We would like to give some further remarks on how to proceed with calculations of the determinant of (6.8)

We define the 4×4 matrices

$$\begin{aligned} \check{F}_{\pm k} &= [\check{Q}_n]_{\pm k,\pm k} - [\check{Q}_n]_{\pm k,\pm k\pm 2}\check{F}^{-1}_{\pm k\pm 2}[\check{Q}_n]_{\pm k\pm 2,\pm k} \qquad k \geq 2 \\ \check{F}_0 &= [\check{Q}_n]_{0,0} - [\check{Q}_n]_{0,-2}\check{F}^{-1}_{-2}[\check{Q}_n]_{-2,0} - [\check{Q}_n]_{0,2}\check{F}^{-1}_{2}[\check{Q}_n]_{2,0} \end{aligned} \tag{6.9}$$

Using these definitions, the determinant is given by $\det \check{Q}_n = \prod_{j=-\infty}^{\infty} \det \check{F}_{2j}$. Both this form of the determinant, and the definition $\check{F}$ in Equation 6.9 become immediately clear if we take into account the determinate of a triangular matrix and elementary matrix operations which do not change the determinant.

In the zero temperature limit the lengthly but straightforward calculation was done analytically in Ref. [37, 74]. The result is given by

$$\begin{aligned} S(\chi) &= \frac{2t_0}{h}\sum_n \int_0^{eV} dE \ \ln\left[1 + \sum_{n=0}^{\infty} P_n(E,V,T_n)(e^{in\chi}-1)\right] \\ P_n(E,V,T_n) &= P'_n(E,V,T_n)/\sum_{n=0}^{\infty} P'_n(E,V,T_n) \\ P'_n(E,V,T_n) &= \sum_{l=0}^{n-l} J_{-n+l}\left[\prod_{k=-n+l+1}^{l-1} \frac{T_n}{4}|f_k^A|^2\right] J_l \qquad n \geq 1 \\ P'_0(E,V,T_n) &= K\left\{Z_0^R\left[1 + \frac{\sqrt{T_n}}{2}(g_0^R - g_{-1}^A) - \frac{T_n}{4}(f_{-1}^A)^2 B_{-2}^A\right] - \frac{T_n}{4}(f_0^R)^2\right\} \\ &\quad \times [R \leftrightarrow A] \end{aligned} \tag{6.10}$$

where we use the abbreviation $x_n^{A,R}(E) = g^{A,R}(E+neV)$ with $x = g, f$ and defined using $\alpha = R, A$ for $n \geq 0$

$$Z^{\alpha}_{\pm n} = 1 \pm \frac{\sqrt{T_n}}{2}(g^{\alpha}_{\pm(n+1)} - g^{\alpha}_{\pm n}) - \frac{T_n}{4}(f^{\alpha}_{\pm(n+1)})^2 B^{\alpha}_{\pm(n+2)} \tag{6.11}$$

$$K = (\prod_{j=1}^{\infty} \det \check{F}_{-2j})(\prod_{j=1}^{\infty} \det \check{F}_{2j}) \tag{6.12}$$

$$
\begin{aligned}
(B^{\alpha}_{\pm n})^{-1} &= 1 \pm \frac{\sqrt{T_n}}{2}(g^{\alpha}_{\pm n} - g^{\alpha}_{\pm(n-1)}) - \frac{T}{4}(f^{\alpha}_{\pm n})^2/Z^{\alpha}_{\pm n} && (6.13)\\
\det \check{F}_{\pm n} &= \prod_{\alpha=A,R}\left(Z^{\alpha}_{\pm n}\left\{1 \pm \frac{\sqrt{T_n}}{2}(g^{\alpha}_{\pm n} - g^{\alpha}_{\pm(n-1)})\right\} - \frac{\sqrt{T_n}}{4}(f^{\alpha}_{\pm n})^2\right) && (6.14)\\
J_{\pm n} &= \left(\prod_{j=1}^{\infty}\det \check{F}_{\pm(n+2j)}\right)\left[\frac{\sqrt{T_n}}{2}(g^{A}_{\pm n} - g^{R}_{\pm n})\left(Z^{R}_{\pm n}Z^{A}_{\pm n} - \frac{T_n}{4}|f^{A}_{\pm n}|^2\right)\right. && (6.15)\\
&\mp \left.\frac{T_n}{4}(f^{A}_{\pm n} - f^{R}_{\pm n})(f^{R}_{\pm n}Z^{A}_{\pm n} + f^{A}_{\pm n}Z^{R}_{\pm n})\right] && (6.16)\\
& && (6.17)
\end{aligned}
$$

With Equation 6.10 we have finally obtained the desired cumulant generating function for charge transport in our model. It has the form of a multinomial distribution in energy space. The different terms in the sum in the argument of the logarithm correspond to transfers of multiple charge quanta ne, i.e., Andreev Cluster, at energy E with probability $P_n(E,V,T)$. This can be seen from the $(2\pi/n)$-periodicity of the accompanying factor $(e^{in\chi}-1)$. The actual probabilities have to be calculated numerically, see Appendix C.

6.2.1 Toy model

To get a feeling for the calculation and matrix structure arising in the superconducting case, a strongly simplified model was presented in Ref.[74]. It basically neglects Andreev reflections for energies outside the gap region and replaces the quasiparticle density of states by a constant for $|E| > \Delta$. In this case the superconducting bulk solutions, see Appendix A.2, reduce to $f^{R,A}(|E|<\Delta) = 1$, $g^{R,A}(|E|>\Delta) = \pm 1$ and both are equal to zero otherwise. Additionally, only MAR voltages $V_n = 2\Delta/n$ are taken into account. Due to the fact that always only one MAR process is considered, the cumulant generating function simplifies to the one of a binomial distribution

$$S(\chi) = \frac{2eVt_0}{h}\ln\left[1 + P_N(e^{iN\chi}-1)\right],$$

where the first three probabilities are given by

$$
\begin{aligned}
P_2 &= \frac{T^2}{(2-T)^2}\\
P_3 &= \frac{T^3}{(4-3T)^2}\\
P_4 &= \frac{T^4}{(8-8T+T^2)^2}.
\end{aligned}
$$

Probabilities to transfer larger charge quanta N can be calculated equally well. To improve accessibility and understanding of the calculation in Ref.[74] will give some note on the calculation details in Appendix B.2 and fix a misprint that slowed down comprehension and reproduction of these results.

Chapter 7

Leakage Current

We will investigate *leakage current*, i.e., current in the subgap voltage regime $eV < 2\Delta$ of a voltage-biased rough superconducting tunnel junction, as it was modeled in Section 4.5. With the method used here, we are able to properly quantify the current contribution due to few high-transmission channels residing in the junction. This will show that, in reality, we face the possibility of much fewer pinholes than suggested in Ref. [33], where a simple tunnel ansatz was used, and which was a major motivation to investigate potential high transmission channels present in Josephson junctions. We will demonstrate how highly sensitive current measurements can clarify the existence of pinholes and can set boundaries to their fraction in all transmission channels. Finally we will point out that current measurements done for the junction of the superconducting qubit device in Ref. [38] does not strictly rule out the existence of a pinhole.

7.1 Average Current

Having calculated the probabilities $P_n(E,V)$ for multiple-charge transport with quanta ne, determined by Equation 6.10, employing the numerical procedure explained in Appendix C, we obtain the average current

$$\begin{aligned}
\bar{I} &= \frac{1}{t_0}\int_0^{t_0} dt\langle I(t)\rangle = \frac{e}{t_0}\langle N\rangle = -i\frac{e}{t_0}\,\frac{\partial}{\partial\chi}S_{t_0}\Big|_{\chi=0} \\
&= \frac{2e}{h}\sum_n \int_0^{eV} dE \sum_n nP_n(E,V,T_n) \\
&= \frac{2e}{h}M\int_0^1 dT\rho(T)\int_0^{eV} dE\sum_n nP_n(E,V,T). \qquad (7.1)
\end{aligned}$$

Here, we will consider a junction with M transport channels where the set of transmission eigenvalues $\{T_n\}$ is described by the distribution $\rho(T)$. To approach our goal to discuss a rough superconducting tunnel junction, we will first start to investigate its constituents in terms of homogeneous contacts.

7.2 Homogeneous contacts

We start from single-mode quantum point contacts (QPC) between superconductors with a transmission eigenvalue distribution $\rho(T) = \delta(T - T_1)$. Later on we will apply this to contacts with multiple channels, given a set of transmission eingenvalues $\{T_n\}$, to model the rough superconducting tunnel junctions under consideration. These are composed of small and high-transmission channels. We discuss all resulting conductance in units of the normal state conductance $G_N = \frac{2e^2}{h} M \int dT \rho(T)$.

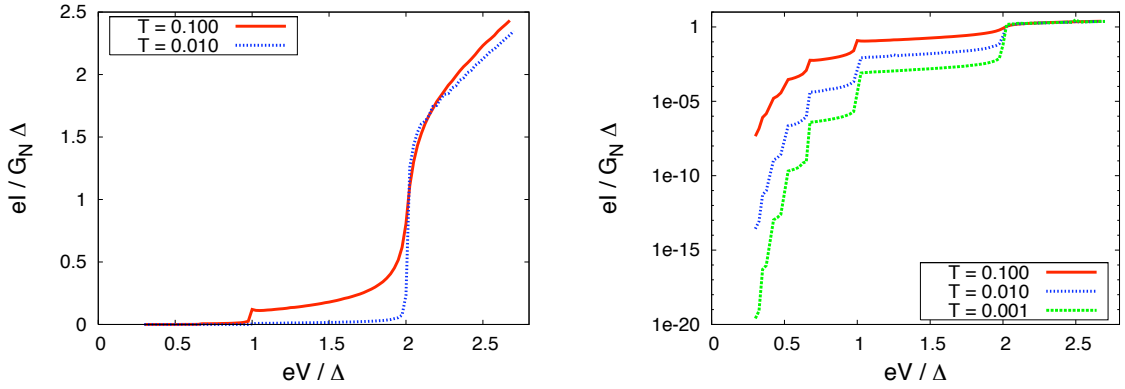

Figure 7.1: Current through a single-mode QPC with small transmission between superconductors as a function of bias voltage at $T = 0K$. Left panel: linear current scale. Right panel: logarithmic current scale.

We start discussing contacts with small transmission eigenvalues. Figure 7.1 shows the current as a function of bias voltage for low transmission probability $T_1 \ll 1$ on a linear (left panel) and logarithmic (right panel) scale. We see that a contact with $T_1 = 0.1$ already develops a relatively large leakage current in the subgap regime $eV < 2\Delta$. Another immediate observation, which will become important below, is the scaling of the subgap current. On a logarithmic scale, conductance steps of size T_1 arise at MAR voltages $2\Delta/n$ demonstrating that the current is reduced at each step by a factor of T_1. As we will see in Section 7.3, current transport for small transmission values in the voltage interval $[2\Delta/(ne), 2\Delta/(n-1)e]$ is dominated by the n^{th}-order MAR process and its average probability $\bar{P}_n = \frac{1}{eV} \int_0^{eV} dE P_n$. In Ref. [74], the authors reduced Equation 6.10 by a perturbative calculation in the case of $T \ll 1$ to

$$P_n(T \ll 1) = \frac{T^n}{4^{n-1}} \rho_0 \rho_n \prod_{k=1}^{n-1} |f_k^A|^2, \tag{7.2}$$

where $\rho(E)$ is the reservoir density of states. This explicitly shows the T^n dependence. It was mentioned by the authors of Ref. [74] that, with Equation 7.2, one recovers for the current the result from the multiparticle tunneling theory of Schrieffer and Wilkins [75], but it leads to divergences in the current. This demonstates that, even for small transmission eigenvalues, the problem cannot be treated by low-order perturbation theory in T and even in this transmission regime we must use the full expression given in Equation 6.10, as we do here.

Experimentally, the reduction of the subgap current by a factor T at MAR voltages $2\Delta/n$ in break junctions was addressed in [76].

After looking at small transmission eigenvalues $T_1 \ll 1$, we consider single mode-contacts with high transmission. Perturbative tunnel approaches will fail in this regime and it is necessary to use more extensive non-perturbative methods, as we do here. This will become especially important for deriving quantitative results in rough junctions containing low- and *high-* transmission channels. Figure 7.2 shows the current for a selection of transmission probabilities $T \geq 0.1$.

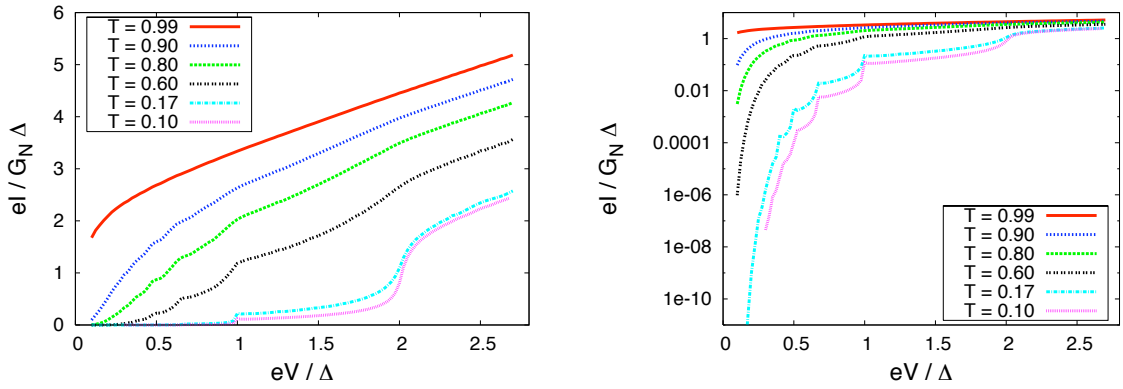

Figure 7.2: Current through a single-mode QPC with high transmission between superconductors as a function of bias voltage at $T = 0K$. Left panel: linear current scale. Right panel: logarithmic current scale.

For high transmission, we see leakage current much larger than the current we find in contacts with tunnel transmission coefficients on the order of $T = 0.1$. This is especially true at small voltages where, in comparison, the current through high-transmission modes is larger by orders of magnitude. Another aspect to be mentioned is that channels with extremely high transmission ($T = 0.8$ and higher) exhibit very little subgap structure, as we see very smooth current curves. Thus, subgap structure is *not* a special feature of channels with extremely high transmission. This aspect will become clear in Section 7.3 and we will come back to this in Section 7.4.

7.3 Probabilities of MAR-Processes

To understand the current transport process more deeply, it is instructive to look at *average MAR probabilities*:

$$\bar{P}_n(V) = \frac{1}{eV} \int_0^{eV} dE P_n(E, V, T).$$

A glance at equation 7.1 shows that the average current $\bar{I}$ is proportional to $\sum_n n\bar{P}_n$, showing that $\bar{P}_n$ can indeed be interpreted as the probability for charge transport with a charge quantum of size ne.

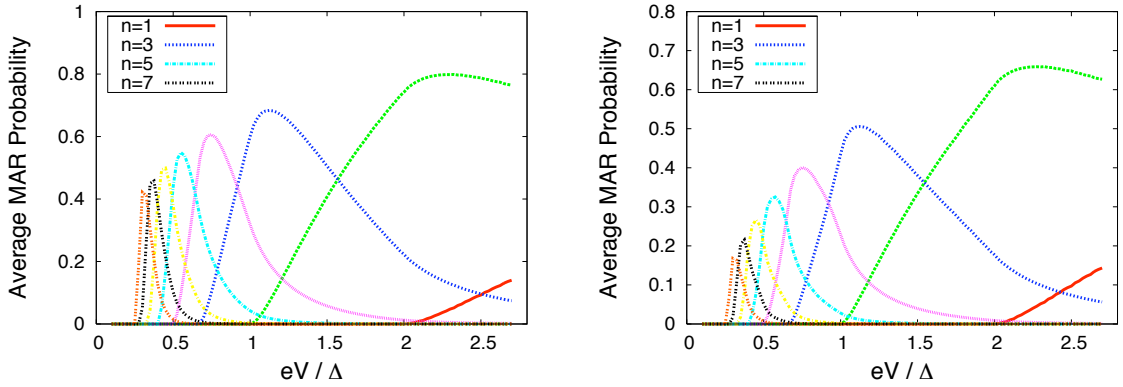

Figure 7.3: Average MAR probabilities $\bar{P}_n = \frac{1}{eV}\int_0^{eV} dEP_n$ as a function of applied voltage bias for several transport processes transferring n charge quanta at a time. Left panel: transmission eigenvalue $T = 0.99$. Right panel: transmission eigenvalue $T = 0.90$. (To improve readability, we have omitted the obvious labels for even process orders n).

In Figures 7.3 to 7.5, the average MAR probabilities $\bar{P}_n$ are plotted for several transmission coefficients ranging from very high to very low transparencies. As expected, independent of the eigenvalue T, there is a voltage threshold for the n^{th}-order MAR process at MAR voltage $V_n = 2\Delta/n$ (see Section 1.5.1). Below this voltage, the energy gap 2Δ can simply not be overcome by an n^{th}-order process.

First, we discuss high-transmission eigenvalues (see Figure 7.3). The average probabilities are smooth and we see that, especially for small voltages, many MAR processes contribute to transport. This smoothens the I-V characteristic and explains the lack of subgap structure observed for the current through high-transmission channels in Section 7.2. For each curve, the probability $\bar{P}_n$ rises for voltages above the threshold $V_n = 2\Delta/n$. This is due to the fact

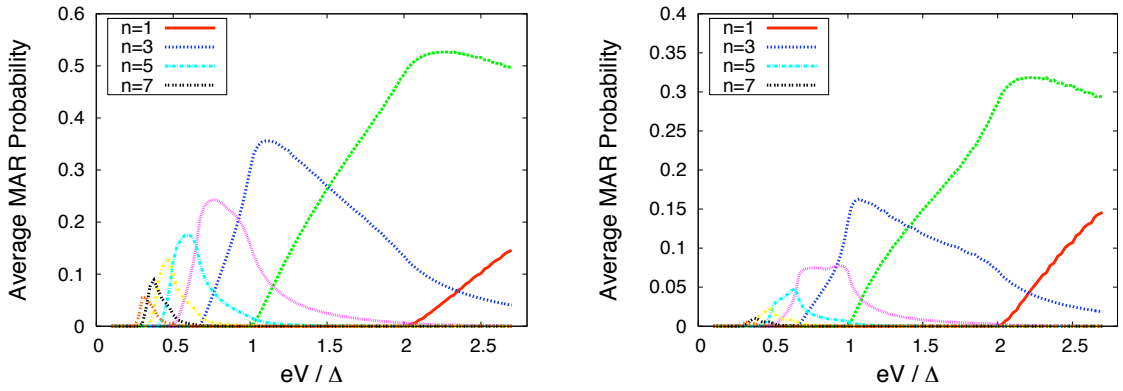

Figure 7.4: Average MAR probabilities $\bar{P}_n = \frac{1}{eV}\int_0^{eV} dEP_n$, as in Figure 7.3. Left panel: transmission eigenvalue $T = 0.80$. Right panel: transmission eigenvalue $T = 0.60$. (To improve readability, we have omitted the obvious labels for even process orders n)

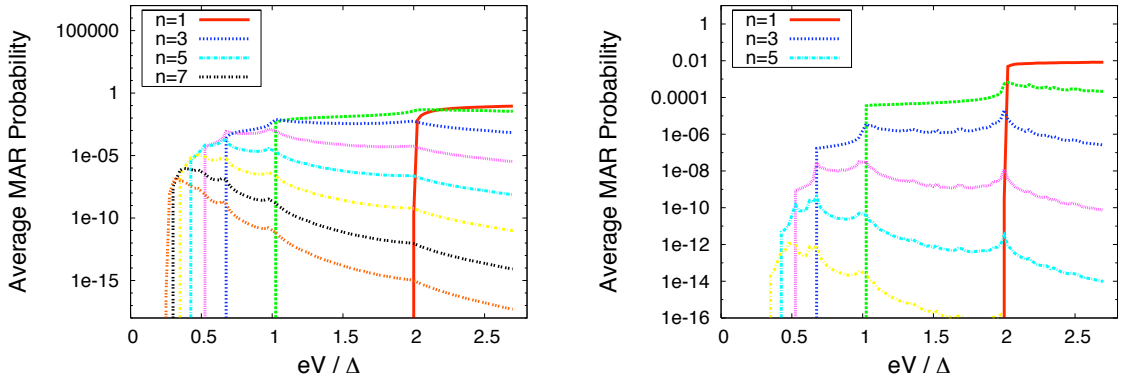

Figure 7.5: Average MAR probabilities $\bar{P}_n = \frac{1}{eV}\int_0^{eV} dE P_n$ as in Figure 7.3 and 7.4 on logarithmic scale. Left panel: transmission eigenvalue $T = 0.17$. Right panel: transmission eigenvalue $T = 0.01$. (To improve readability, we have omitted the obvious labels for even process orders n)

that, with an n^{th}-order process, we connect energies at E with thoses at $E + neV$ and their densities of states in the left and right terminal, respectively. For $V = V_n$, only the exact energies at the edges above and below the energy gap 2Δ can be connected by an n^{th}-order process . By increasing the voltage above V_n, a larger energy window enters in the n^{th}-order transport process, causing the rise in probability. For higher voltages, the energy gain of the n^{th}-order process neV starts to exceed 2Δ so much that the decrease of the density of states above and below the gap in both terminals reduces the contribution of the n^{th}-order process again. It is worth mentioning that the BCS density of states does not cause any divergences not even at $V_n = 2\Delta/n$. The possible divergence at $V_n = 2\Delta/n$ is renormalized by the full expression given in Equation 6.10.

Reducing the transmission coefficient (Figure 7.4) naturally decreases the probabilities. This is especially true for high-order MAR processes which involve multiple channel crossings and thus depend on high orders of T. Due to this, the $\bar{P}_n$ curves become deformed, causing subharmonic gap structure in the current, as seen in Section 7.2. Finally, for small transmission eigenvalues (Figure 7.5) transport in the voltage interval $[2\Delta/ne, 2\Delta/(n-1)e]$ is strongly dominated by the n^{th}-order MAR process. As already mentioned in Section 7.2, this causes the jumps in current and produces effectively exclusive transport in charge quanta of size ne. This behavior is also responsible for the charge quantization of noise in tunnel junctions seen in [31]. We will discuss this in Chapter 8.

7.4 Characterizing Pinhole Thresholds

So far, for illustrative reasons, we have looked at contacts with M channels but only a single transmission eigenvalue T_1 with distribution $\rho(T) = \delta(T - T_1)$. Our ultimate goal is, however, to investigate rough Josephson tunnel junctions as they are used in superconducting qubit devices, assuming a small number of pinholes with transmission eigenvalues close to unity that reside in the junction.

We consider a contact with M channels. Each of these channels has either transmission eigenvalue $T_1 = 0.986$ or $T_2 = 0.01$. The variable a determines the ratio of pinholes with transmission T_1 among the many of transport channels and is small according to our model. $(1-a)$ is the ratio of channels with small transmission coefficients, typical for tunnel contacts. Altogether, we consider the eigenvalue distribution

$$\rho(T) = a\delta(T - T_1) + (1 - a)\delta(T - T_2), \tag{7.3}$$

causing a normal conductance of

$$G_N = \frac{h}{2e^2} M[aT_1 + (1 - a)T_2].$$

In Section 7.5 we will discuss why this distribution captures the essential physics of even more complicated distributions.

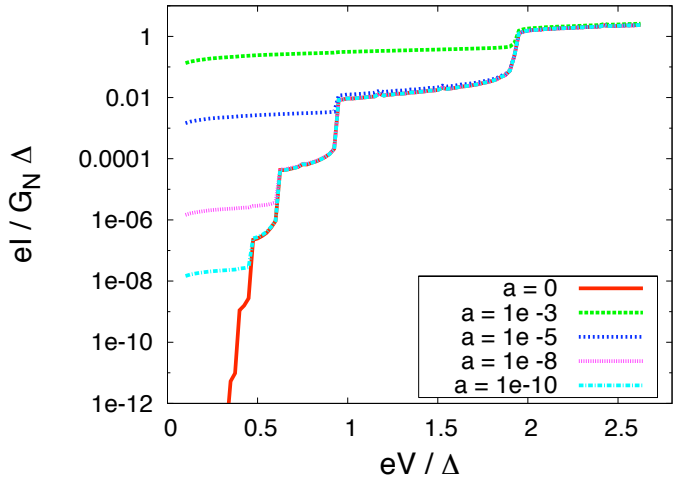

Figure 7.6: Leakage current on a logarithmic scale as a function of bias voltage at $T = 0K$ for a rough superconducting tunnel junction with transmission eigenvalue distribution $\rho(T) = a\delta(T - T_1) + (1 - a)\delta(T - T_2)$, $T_1 = 0.986$, and $T_2 = 0.01$. The different curves refer to different pinhole fractions within all transport channels, given by the parameter a.

We calculate the current for this arrangement, taking into account the very different transport properties of T_1 and T_2, as seen in the previous sections. The result is shown in Figure 7.6. A look at the values of parameter a reveals that, in this plot, we have considered extremely small fractions of pinholes, but even for those the leakage current changes dramatically. We see that, starting at high voltages, the current follows the well-known curve for tunnel transmission coefficient T_2 only to a certain point, depending on a. In this voltage regime the current exhibits the steps explained in Section 7.2 and Section 7.3.

As we have seen before, due to their high transmission, the current carried by pinholes shows a smooth, weakly structured subgap contribution and is barely reduced even at small voltages (cf. Figure 7.2). In contrast, the current carried by the tunnel transmission eigenvalues is reduced by a factor of T_2 each time the voltage falls below another MAR voltage

$2\Delta/n$. Consequently, at sufficiently low voltages, the current through rough tunnel contacts considered here, including some high transmission channels, is carried by the pinhole fraction only.

We can use this result to characterize the proportion of pinholes in all transmission channels by very sensitive current measurements. For a homogeneous tunnel contact with all channels having the same eigenvalue T_2, we expect current steps scaling with a factor of this transmission each time we pass another MAR voltage. In contrast, as we have seen, the current through very high-transmission channels does not exhibit these steps and proceeds smoothly as a function of bias voltage. Consequently, due to this kind of current in tunnel junctions possessing a small amount of pinholes, at some point the current will drop by less than a factor of T_2. From there on, continuing to smaller bias voltages, it is predominantly carried by the junction's proportion of high transmission channels showing the specific characteristics of these channels.

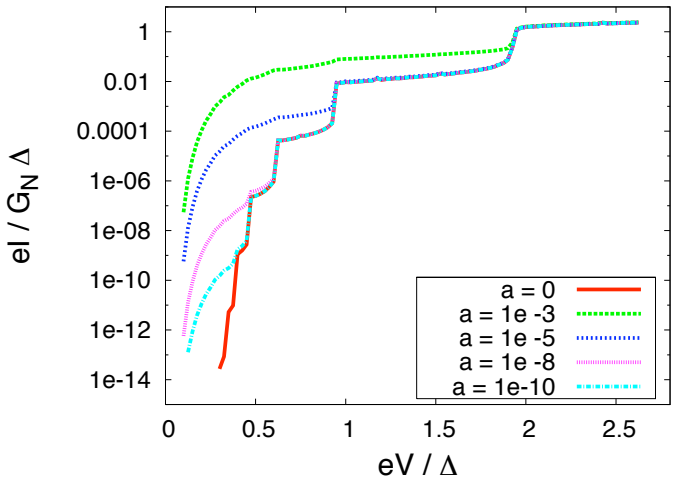

Figure 7.7: Leakage current on a logarithmic scale as a function of bias voltage at $T = 0K$ for a rough superconducting tunnel junction with transmission eigenvalue distribution $\rho(T) = a\delta(T - T_1) + (1 - a)\delta(T - T_2)$, $T_1 = 0.6$ and $T_2 = 0.01$. The different curves refer to different pinhole fractions within all transport channels given by the parameter a.

In Figure 7.7 we use the same transmission eigenvalue distribution as above, but with pinhole transmission $T_1 = 0.6$. As anticipated, at the crossover where finally the pinhole fraction starts to dominate the current characteristic, the current drop is smaller, in general, than T_2. For voltages below the crossover, the current shows the characteristic of a homogeneous $T_1 = 0.6$ contact, cf. Figure 7.2.

Finally, looking at the value of parameter a, we emphasize that, from this simple model, we have to anticipate that talking about high-transmission pinholes in tunnel junctions, which possess their typical step-like current-voltage characteristic, means talking about very few of such channels in huge junctions. For example, from Figure 7.7 we infer that, in a tunnel junction, where a possible measurement shows two full current steps, each scaling with a factor of $T = 0.01$ at $eV = 2\Delta$ and $eV = 2\Delta/2$, respectively, we can have roughly less than

1 out of 10^6 channels with transmission $T \geq 0.6$!

In Ref. [33], experimental data of current measurements in Nb-AlO_x-Nb tunnel junctions were modeled with a certain fraction of pinhole defects contributing to the total normal state conductance. The authors consider this fraction and a value for the transmission of pinhole channels within a simple tunnel ansatz. Although experimental data can be modeled well, the tunneling approach, which considers a current reduction by a factor T^n for the n^{th}-order process in high-transmission channels, is naturally insufficient. With the method used here we can quantify the current due to pinholes with high transmission in an appropriate way. This way, we properly take into account the very different transport properties of channels with high- and low- transmission eigenvalues, which we have seen in Section 7.3. As a major result, we see that, in tunnel junctions with characteristic current steps similar to Figure 7.1, we can only have very few pinholes and even these only in large junctions, but in general the existence of pinholes cannot be ruled out, see Section 7.5. Using the methods presented here, we anticipate that the description in Ref. [33], which suggested a junction consisting of 30 percent pinholes with transmission $T = 0.68$, and which was a major motivation for investigating pinholes residing in tunnel junctions is far from describing a tunnel junction. In fact, we have seen here that these kinds of junctions, with characteristic current steps, have to be huge such that we might have very few pinholes. If there were more, the subgap current would behave differently.

7.5 Pinholes in Josephson Qubit Devices

While we were looking for subgap current characteristics of tunnel junctions used in superconducting qubit devices, John M. Martinis kindly referred us to Ref [77]. In this paper, the authors present a current-voltage plot for a Al-Al_2O_3-Al junction used in a Josephson-junction qubit. The data are shown in Figure 7.8 in comparison with a sample calculation using the simple junction model from Section 7.4.

The experimental plot presents a voltage drop at $eV = 2\Delta$, corresponding to a tunnel transmission eigenvalue of $T = 0.003$. At $eV = \Delta$ the current starts to drop again, but the fall-off is less steep and the measurement does not reach the next expected plateau. As there are only very few data points in this region, and we obviously seem to reach the limitations of measurement, it might be too speculative to ascribe the broadening of the second decline to some additional tunnel channels with transmission slightly higher than $T = 0.003$. Nevertheless, the fact that we see the current drop at $eV = 2\Delta$ and the beginning of a second one at $eV = \Delta$ gives us an order of magnitude estimate for the possible number of high-transmission pinholes which might reside in the junction.

To estimate this order of magnitude, we present theoretical results (see right panel of Figure 7.8) for the simple junction model given in Section 7.4 with tunnel transmission coefficient $T_2 = 0.003$ according to the measured voltage drop at $eV = 2\Delta$ and, for instance, a pinhole transmission coefficient of $T_1 = 0.6$. As we have seen in Figure 7.2, for voltages around $eV = \Delta$ and higher, the magnitude of the G_N-normalized current through channels with transmission of $T = 0.6$ and larger have roughly the same magnitude. The plot with parameter $a = 0.5 \cdot 10^{-5}$ develops the full current drop with factor $T_2 = 0.003$ at $eV = 2\Delta$, but only a reduced drop at $eV = \Delta$. Below this voltage the current is primarily carried by the pinhole channels. Such a scenario could be embodied in the experimental measurement (left panel Figure 7.8). There, as well, we see the voltage drop by $T_2 = 0.003$, but the current

characteristics following the indicated drop at $eV = \Delta$ is unknown.

The fraction of pinholes in all transport channels $a = 0.5 \cdot 10^{-5}$, that would be consistent with the current measurement above, corresponds to one pinhole in $1/a = 200\,000$ channels. The question is whether the junction under consideration is large enough such that there are enough channels for these extremely open channels to be possible to exist.

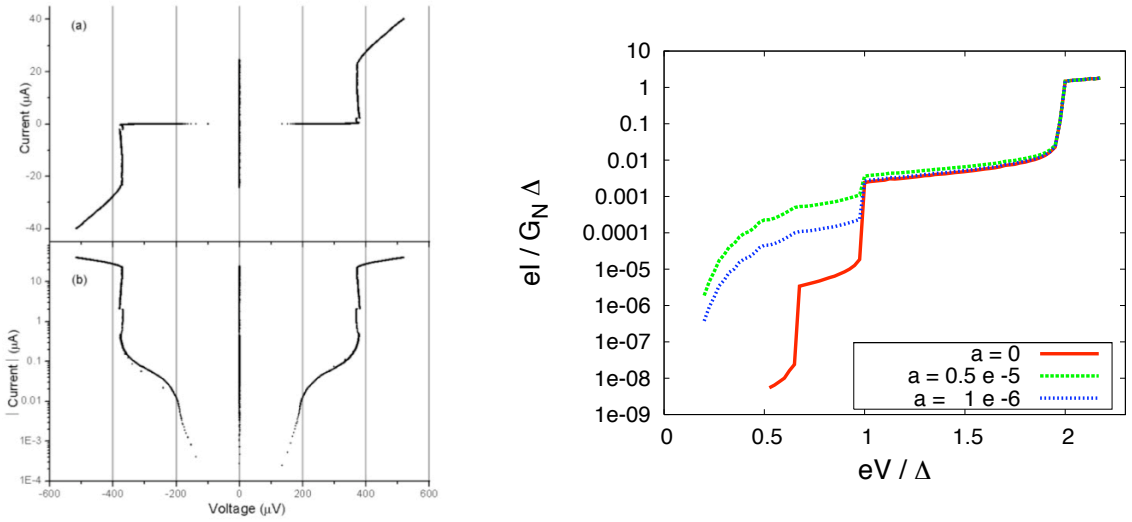

Figure 7.8: Left Panel: $T = 20mK$ Current-voltage plots for a Al-Al_2O_2-Al junction on normal and logarithmic scale, measured in Ref. [77]. The current drop at $V = 390\mu m$ corresponds to $eV = 2\Delta$. Right Panel: Calculation for current at $T = 0K$ for a rough superconducting tunnel junction with transmission eigenvalue distribution $\rho(T) = a\delta(T - T_1) + (1 - a)\delta(T - T_2)$, $T_1 = 0.6$ and $T_2 = 0.003$

In Ref [38], the authors estimate the number of transport channels for the junction measured in Ref [77] and for which a current-voltage characteristic is shown in Figure 7.8. They do so using the average tunneling transmission $\tau = 4 \cdot 10^{-3}$ and the junction's normal-state resistance $R_N = 29\Omega$ with the Landauer formula to calculate $N_{ch} = 1/(2\tau R_N e^2/h) = 125\,000$ channels. Thus from the estimations given here, we see that the magnitude of channels is roughly comparable to the number of channels needed for a single pinhole with high transmission to exist, consistent with current measurements. Altogether, we see that the existence of pinholes in state-of-the-art superconducting qubit devices is not strictly ruled out by current measurements so far. Indeed, using new design concepts have significantly reduced the junction size (see Ref.[39]). Nevertheless, to our knowledge, for those setups there are no reported highly sensitive current-voltage measurements in the low voltage regime stretching out over several current steps at $V_n = 2\Delta/n$. Future very sensitive current measurements in the low-voltage regime may clarify the actual existence of pinholes in superconducting qubit devices. In the following, we will assume very few pinholes to exist in a rough superconducting tunnel junction. We will show that having even very few of them will result in import effects.

Now it becomes clear why we used this very simple transmission distribution function, introduced in Section 7.4. When we started the project, we thought about doing statistics on the pinhole channels. For example, we considered a model where the transmission eigenvalues are determined by WKB, $T = \exp(-\kappa d)$, and this way, depend on the junction width d. Then

the pinhole transmission eigenvalues might be related to a width distribution $\rho(d)$ of the oxide layer separating the superconductors. Considering the strict non-negativity of d, a lognormal distribution might be appropriate for describing $\rho(d)$ for the pinholes.

All this can be done in our approach, but as we have seen above, in state-of-the-art superconducting qubit devices we might only have a small, single-digit number of pinholes in a huge junction. Thus, doing statistics is unjustified and considering a single value T_1 to represent the pinhole transmission eigenvalue distribution, as done in Equation 7.3, is a sensible way to consider them.

Chapter 8

Noise

We will examine the noise properties of rough superconducting tunnel junctions possessing some high-transmission channels residing in the junction. For high and subgap voltage, for which the energy is not too far below the superconducting gap $2\Delta/e$, we will find that such a junction basically behaves like a tunnel contact. However, we will demonstrate that already very few of these spurious pinholes give rise to an enormous increase of noise in the very low-subgap voltage regime. Although details of the comprehensive calculation given by the full expression, Equation 6.10, show quite complex behavior, and we will indicate that the character of noise enhancement due to MAR in open channels is much more complicated than in small transmission ones, we will discuss that the physical essence of the observed noise enhancement still has its seeds in the increased charge quantum that is transferred. Comparison to a simple model containing this essence will show qualitative agreements, but quantitative failure. This will demonstrate the necessity to utilize more sophisticated methods, as we do, in order to find the quantitative results present here. Along the way, we will calculate explicit results for the junction measured in Ref [30], see Figure 1.5.

8.1 Noise and cumulant generating function

The relation between the current noise power,

$$S_I \equiv \int_{-\infty}^{\infty} d\tau \langle \{\delta I(\tau), \delta I(0)\} \rangle, \tag{8.1}$$

and the second cumulant, which is given by the cumulant generating function, is less obvious than the analogous equation for the current [78]. Here, $\delta I(\tau) = I(\tau) - \langle I \rangle$ is the current-fluctuation operator and $\langle \ldots \rangle$ denotes quantum statistical average. The second cumulant can be written as

$$C_2 = \overline{(N - \overline{N})^2} = \frac{1}{2e^2} \int_0^{t_0} \int_0^{t_0} dt dt' \langle \{\delta I(t), \delta I(t')\} \rangle. \tag{8.2}$$

After transforming to average $\bar{t} = (t + t')/2$ and relative $\tau = t - t'$ time coordinates, and assuming that the observation time t_0 is much longer than the current correlation times, the correlator above will not depend on $\bar{t}$. Thus, after executing both integrations using Equation 8.1, we find the relation

$$S_I = \frac{2e^2}{t_0} \frac{\partial^2}{\partial \chi^2} S_{t_0} \Big|_{\chi=0}.$$

Note that, by using the cumulant generating function, we calculate zero-frequency noise since finite frequency would give rise to another factor $e^{i\omega t}$ in Equation 8.2. Using Equation 6.10 for S_{t_0}, we finally get

$$S_I = \frac{4e^2}{h} \int_0^{eV} dE[\sum_n n^2 P_n(E,V,T) - (\sum_n n P_n(E,V,T))^2]. \tag{8.3}$$

8.2 Dieleman's noise measurement

As mentioned in the introduction (see Section 1.5.2) one of the main motivations for looking at pinholes in tunnel junctions is the measurement of doubled shot noise due to 2^{nd} order MAR presented in Ref. [30, 31]. For this reason we come back to this experiment and start to calculate current and noise for this setup using our approach and considering a homogeneous superconducting tunnel junction with reported transmission eigenvalue $T = 0.17$. The results for current and noise are shown in Figure 8.1. Our calculation shows the peak at $eV = 2\Delta$

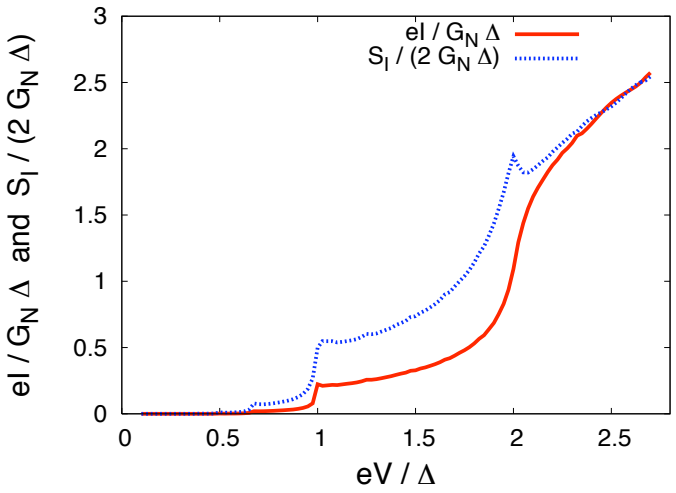

Figure 8.1: Noise and current for a homogeneous superconducting tunnel junction possessing transmission $T = 0.17$ at zero temperature, as a function of bias voltage. The calculation corresponds to the measurement done in Ref. [30] (see Figure 1.5 in Section 1.5.2).

measured in Ref. [30] (see Figure 1.5) which is effectively due to the sharp decline of the current. For voltages above this value, the noise follows Poissonian shot noise $S_I = 2eI$ [4]. Below $eV = 2\Delta$, the noise is approximately enhanced by a factor of two, and below $eV = \Delta$ by an even higher value. This indicates that, for this junction and its transmission eigenvalue, the model of enhanced Poissonian shot noise due to a larger transfered charge quantum $q(V)$, which is simply used in the Schottky formula $S_I = 2q(V)I$, is still valid, thus explaining experimental data in [30] well (see also the calculated average MAR probabilities $\bar{P}_n$ in Figure 7.5). In the experimental paper [30] the effective charge

$$q(V) = e \cdot \frac{\sum_{m=1}^{\infty} m I_m(V)}{\sum_{m=1}^{m=\infty} I_m(V)}$$

was determined by weighting the quantum m with the current I_m, carried by m Andreev reflections. I_m was calculated using the semiclassical trajectory method of the original paper on MAR [34] assuming unity transmission.

For higher transmission, which will become important with respect to our question regarding the effects of pinholes residing in the tunnel junction, the concept of effective charge is questionable. Firstly, we don't expect the Poissonian shot noise formula to be valid in this high-transmission regime, and secondly, as we have seen in Section 7.3, not one, but many MAR processes transferring differently-sized charge quanta ne will contribute to transport, with each process sensitively depending on T, cf. Figure 7.3 to Figure 7.5. The approach we are using here properly deals with this T-dependence.

8.3 Homogenous contacts

Again, as in Chapter 7 at the beginning, we will look at the constituents of rough superconducting tunnel junctions being composed of high- and small- transmission channels. Thus, firstly we regard homogeneous contacts with each channel having the same transmission eigenvalue (Ref. [74]) We start with small transmission tunnel contacts $T \ll 1$. Figure 8.2 shows

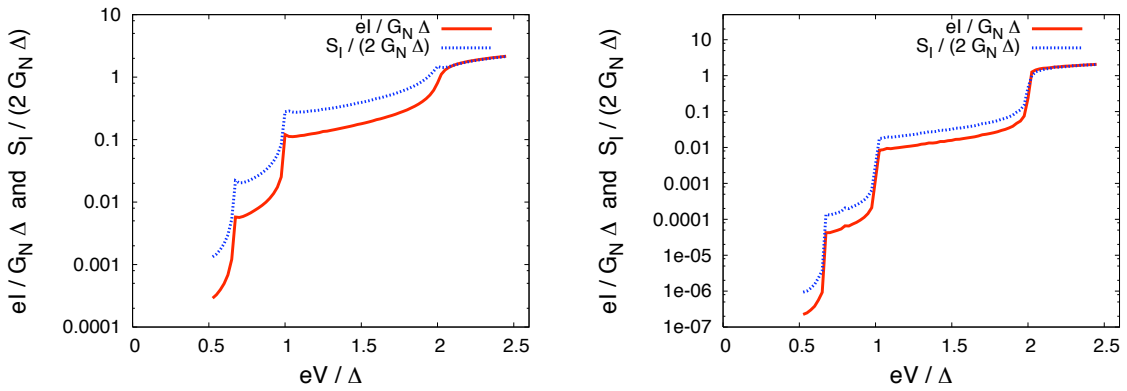

Figure 8.2: Noise and current as a function of bias voltage for two homogeneous superconducting tunnel junctions with different transmission eigenvalues. Left Panel: $T = 0.1$. Right Panel: $T = 0.01$.

noise and current characteristics for this case. At voltages above the gap, we see Poissonian shot noise $S_I = 2eI$. Below $eV = 2\Delta$, the noise scales with an additional effective charge factor, depending on the dominating MAR-process, as seen in Section 7.3. Thus, as already mentioned in the tunneling regime, we have Poissonian shot noise with quantized effective charge $q(V) = e(1 + \mathrm{Int}(2\Delta/eV))$, depending on the relevant MAR-process, where $\mathrm{Int}(x)$ is defined as $n \in \mathbb{N}_0$ with $n < x$.

In the case of large-transmission eigenvalues, as shown in Figure 8.3, the noise characteristic changes dramatically. For very high probabilities T, the noise increases with decreasing voltage in the subgap regime, depending on the value of T. It develops a maximum, but falls off again at even lower V. Remarkably, and in strong contrast to any simpler model, we note that a contact with perfect transmission $T = 1$ shows low, but finite noise. This is completely different from the normal conducting case, where given the shot noise formula

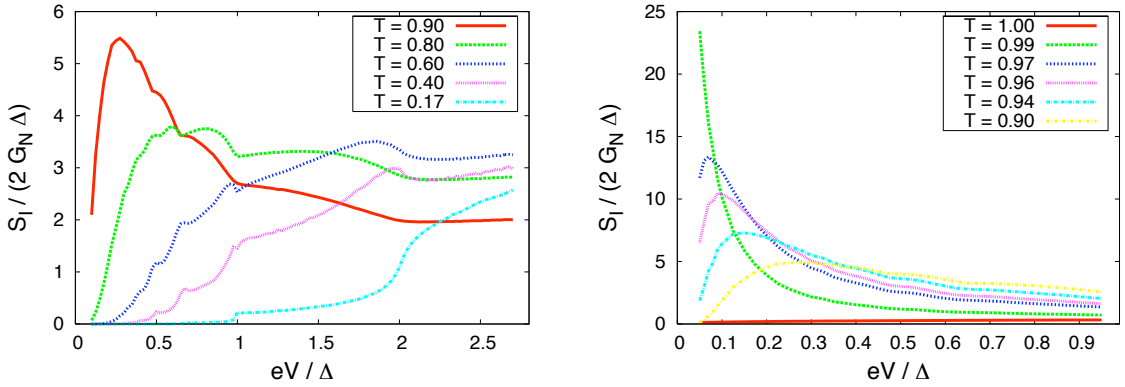

Figure 8.3: Noise of a single-mode QPC between superconductors as a function of bias voltage for large transmission eigenvalues T. Left panel shows transmission up to a value of $T = 0.9$. Right panel shows shows transmission values larger than $T = 0.9$

$S_I = (Ve^3/\pi\hbar)T(1-T)$, we would anticipate zero noise in the case of perfect transmission. Furthermore, we see that the larger the transmission the steeper and higher is the noise ascent for small voltages. For high eV, the high transmission curves approach the $T = 1$ characteristic.

Altogether, although we see a dramatic increase of S_I as function of decreasing voltage bias in the subgap regime, the noise *does not* agree with pure Poissonian shot noise $2qI$ given a larger charge quantum $q(V)$, which depends on the relevant MAR transport process. On the one hand, this could not explain the decrease of noise after reaching its maximum. On the other hand, for very high transmission, the noise does not follow the current curve for $eV \geq 2\Delta$ and is even finite for $T = 1$, which is very different from the the normal conducting case, where we have $S_I = \frac{e^3V}{\pi\hbar}T(1-T)$, see ([4]).

Finally, it is instructive to look at the noise curve from a different perspective, focussing on the T-dependence. In Figure 8.4, we set voltage as a parameter and plot the noise as a function of transmission. We see that, for small voltages, the noise develops a maximum at high transmission values, but as we noticed before, each curve falls off to a small but finite residual noise level at $T = 1$. For smaller voltages, the maximum becomes more and more pronounced and it seems to be squeezed into the high-transmission regime, although calculations show that $\int S_I \; dT$ is not constant for different voltage parameters. At small voltages on the order of $eV = 0.1$ only channels with very high transmission significantly contribute to the noise.

We now provide a physical explanation for these observed features. We start with the small-transmission case. As we have already seen in Section 7.3 for small transmission, there is always one very dominant MAR-process effectively causing charge transport in charge quanta of $q(V) = e(1 + \mathrm{Int}(2\Delta/eV))$ only. Thus, in the small-transmission regime Poissonian shot noise with modified charge quantum ne, which is determined by the dominant MAR-process, properly explains the observed noise features.

The explanation for high transmission is more difficult. We begin with the extreme case

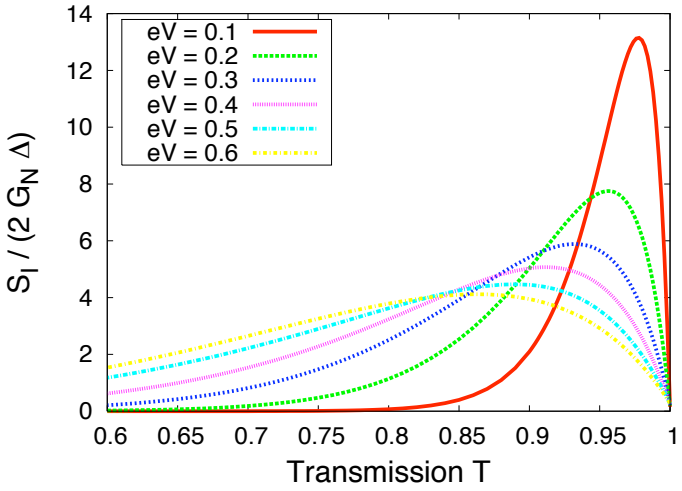

Figure 8.4: Noise S_I as a function of transmission eigenvalue T for a single-mode QPC between superconductors, where bias voltage in the subgap regime is set as a parameter.

of perfect transmission $T = 1$, where we have seen finite noise, in absolute contrast to the normal-conducting situation. Using Equation 8.3, we can express the noise in terms of the variance of $P_n(E, V, T)$, which is the probability distribution of a MAR-proces transferring charge quanta ne

$$S_I = \frac{4e^2}{h} \int_0^{eV} dE[\langle n^2 \rangle - \langle n \rangle^2] = \frac{4e^2}{h} \int_0^{eV} dE \, \mathrm{Var}(n) \tag{8.4}$$

For a single-mode normal conductor with perfect transmission $T = 1$, there is no uncertainty whether a particle is transmitted or reflected. Thinking of shot noise as partition noise, this results in zero noise. In the superconducting case considered here, we are still certain about charge transfer taking place, due to perfect transmission, but an additional uncertainty is introduced, namely the size of the transferred charge in each cycle, which is given by the probability distribution P_n. In Section 7.3 we have seen that, for high transmission probability including $T = 1$, there are many different MAR-processes contributing to charge transport (see Figure 7.3). This additional uncertainty is the qualitative physical explanation of the finite noise observed in the case of perfect transmission in the superconducting case.

To understand the noise features for high but imperfect transmission as seen in Figure 8.3, we have to look at the probabilities $P_n(E, V, T)$, which determine the variance entering Equation 8.4. In Figure 8.5 we illustrate the energy dependence of $P_n(E, V, T)$ for the transmission probabilities $T = 0.9$, $T = 0.97$ and $T = 1$ at voltage bias $eV = 0.1\Delta$. We have seen before, that the noise of high-transmission eigenvalues as a function of voltage primarily increases if we reduce the applied voltage, but after developing a maximum, the noise falls off again. Thus, apart from the special case of perfect transmission, we chose the two additional transmission eigenvalues such that, at $eV = 0.1\Delta$, we consider one point in the increasing ($T = 0.97$) and one in the decreasing noise regime ($T = 0.9$); see first panel in Figure 8.5. We should remark again that talking about increase and decrease, we always consider the noise slope

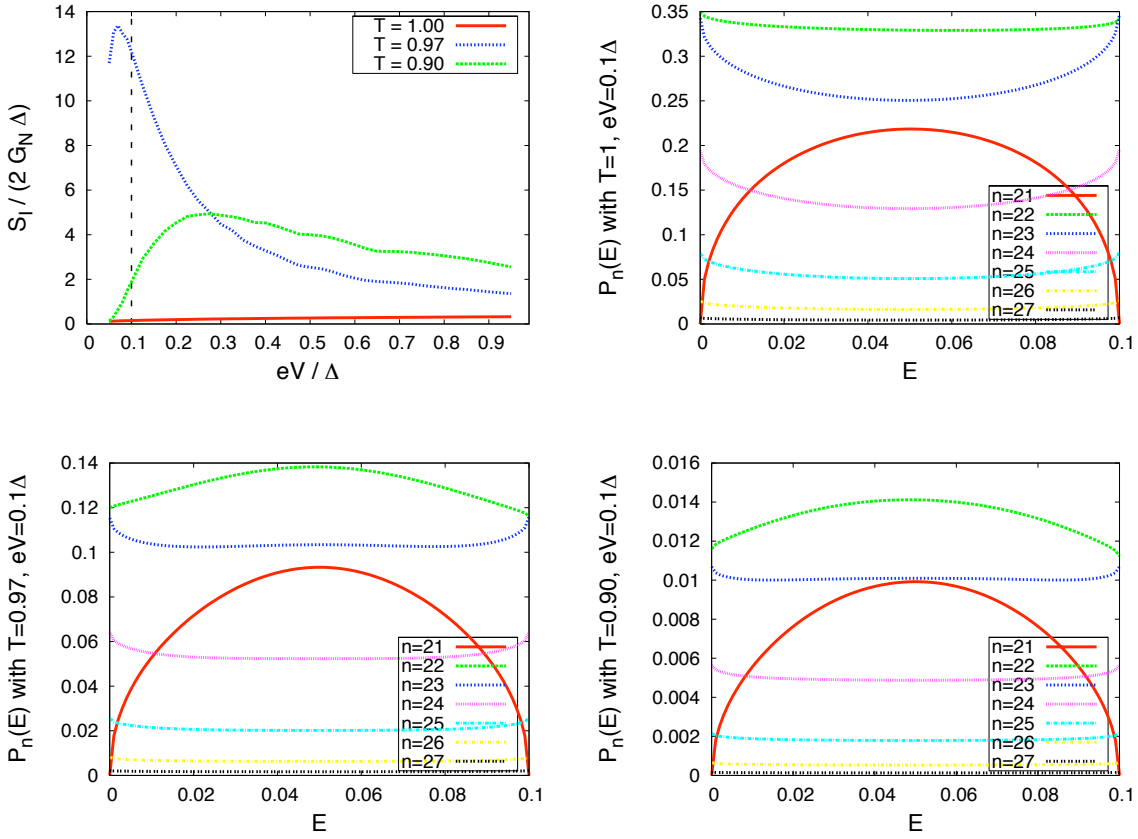

Figure 8.5: Panel 1: noise as a function of bias voltage for single-mode QPCs between superconductors for the three transmission eigenvalues considered in panels 2-4. Panels 2-4: Energy dependence of MAR probabilities P_n for several transport processes transferring n charge quanta at a time for voltage bias $eV = 0.1\Delta$. The individual panels refer to the transmission eigenvalues $T = 1$, $T = 0.97$ and $T = 0.9$, whose noise characteristics are regarded in panel 1, where the voltage parameter $eV = 0.1\Delta$ is indicated by the dotted line.

depending on voltage coming from high energies eV, going to smaller ones. In Figure 8.6, the energy dependence of $P_n(E, V, T)$ is shown for the same transmission parameters at voltage bias $eV = 0.5\Delta$. Note that here, in contrast to the previous case, $T = 0.9$ shows the highest noise of all three values, as the $T = 0.9$ and $T = 0.97$ noise curves cross around $eV = 0.3\Delta$ (see first panel of Figure 8.5 or Figure 8.6)

Looking at Figure 8.5 and Figure 8.6, we see that there is a specific energy dependence of $P_n(E, V, T)$. Furthermore, we note that, in principle, all the graphs for different parameters shown here look very similar. For example the curve of the lowest possible MAR process with finite probability is always concave, with reduced probability at the energy interval edges. Higher process probabilities are convex. As expected, starting with perfect transmission and going to smaller transmission eigenvalues strongly reduces $P_n(E, V, T)$. Additionally, we see that the curves might as well become slightly distorted by changing the parameters. This can be seen clearly in Figure 8.6 for the $n = 5$ case.

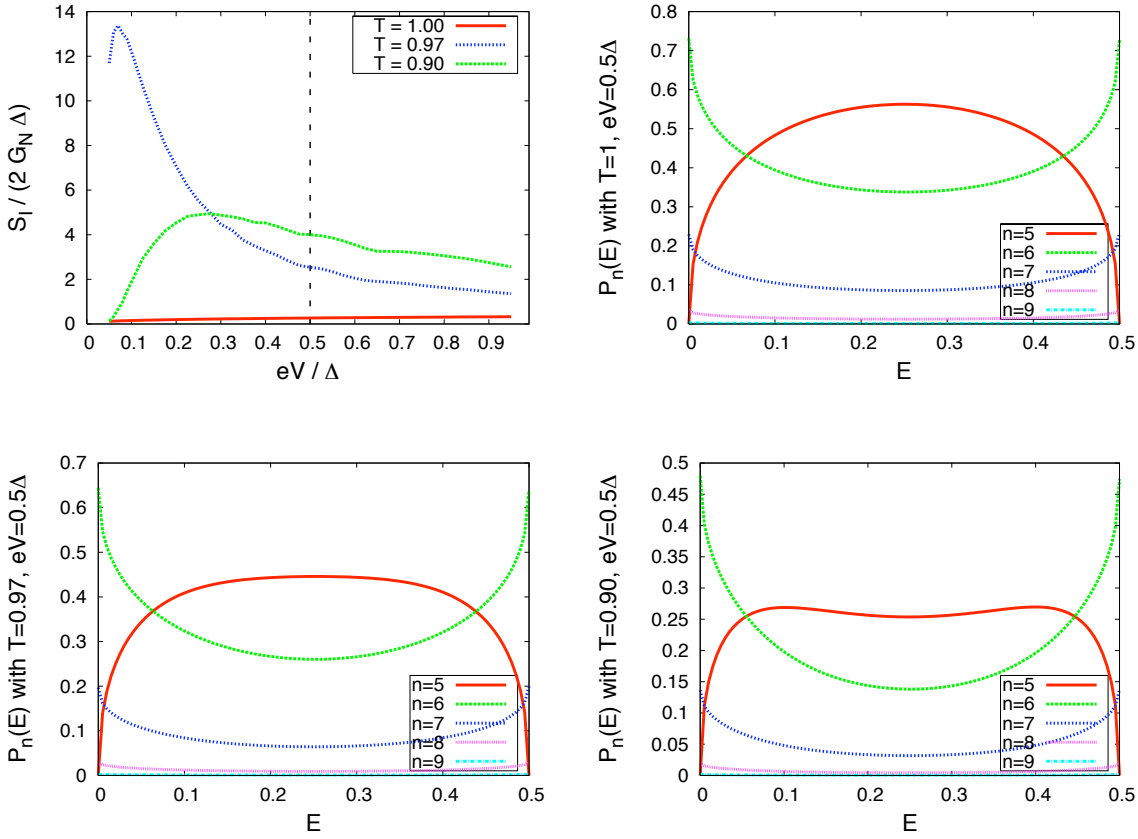

Figure 8.6: Panel 1: noise as a function of bias voltage for single-mode QPCs between superconductors for the three transmission eigenvalues considered in panels 2-4. Panels 2-4: Energy dependence of MAR probabilities P_n for several transport processes transferring n charge quanta at a time for voltage bias $eV = 0.5\Delta$. The individual panels refer to the transmission eigenvalues $T = 1$, $T = 0.97$ and $T = 0.9$, whose noise characteristics are regarded in panel 1, where the voltage parameter $eV = 0.5\Delta$ is indicated by the dotted line.

Looking at the different noise curves resulting from these MAR process probability distributions with their very different quantitative behavior, and in the case of perfect transmission even qualitative difference, we have to adopt that these little changes in $P_n(E, V, T)$, due to parameter change, very sensitively affect the resulting noise features. Consequently, to get quantitative noise results from the $P_n(E, V, T)$ distribution, we really have to take into account all its energy dependence, and have to do the long calculation to finally integrate over the MAR process probability distribution (Equation 8.4) correctly.

With respect to our goal of understanding the essential physics behind our calculated noise characteristics, the previous statement, which basically solely refers to the long calculation using the full expression in Equation 6.10, seems to be unsatisfactory. Thus, we will try to explain the basic noise features with the use of the strongly simplified toy model presented before in Section 6.2.1. Originally, this model was introduced to illustrate, in a strongly simplified way, how to calculate the cumulant generating function of a weak link with voltage

bias in an easy analytically solvable case. We briefly summarize the basic simplifications again.

We only look at MAR voltages $eV = 2\Delta/n$, and for each voltage we only take into account one MAR process. This simplifies the cumulant generating function $S(\chi)$ in Equation 6.10 to the one of a binomial distribution. Given the MAR voltage eV, the only incorporated transport process, as mentioned above, is the one which transfers $N = 2\Delta/eV + 1$ charge quanta. We have seen in Figure 7.3 that, in the actual multiprocess case, at MAR voltages, this process is the one with the highest probability. Furthermore, in this analytically solvable model, Andreev reflection above the gap was neglected and the Green's function was simplified by assuming a constant density of states.

Due to the fact that in this model, we consider a binomial, rather than the actual multinomial distribution, it is clear from partition noise arguments, given above, that this way, we will not be able to explain the feature of finite noise at perfect transmission. Thus, we already see that this model will only be sufficient to illuminate certain aspects of the more complicated full calculation and cannot supply an easy demonstrative explanation for everything. We have to compromise model generality and descriptive simplicity.

The cumulant generating function for the toy model in this case reads

$$S(\chi) = \frac{2eVt_0}{h} ln\left[1 + P_N(e^{iN\chi} - 1)\right]. \tag{8.5}$$

At each MAR voltage, the only considered, but mostly relevant, transport process is the one which transfers

$$N = \frac{2\Delta}{eV} + 1 \tag{8.6}$$

charge quanta. Thus, for every MAR voltage, another specific transport process with probability P_N is relevant. We emphasize the point that, due to this the argument of the logarithm in Equation 8.5 depends on voltage via the selection of the relevant P_N, see Equation 8.6.

The left panel of Figure 8.7 shows the toy-model probabilities P_N as a function of transmission eigenvalue T. For perfect transmission, each probability is unity, as we have reduced the

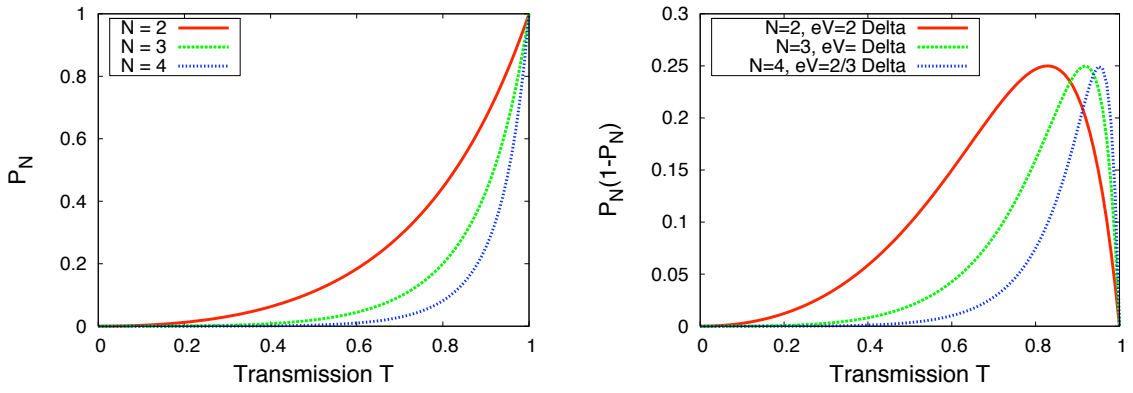

Figure 8.7: Left panel: Toy model probability P_N to transfer N charges at a time as a function of transmission eigenvalue T. Right panel: expression $P_N(1 - P_N)$ that occurs as a term in the 2^{nd} cumulant (Equation 8.7) as a function of transmission eigenvalue T.

system to a binomial distribution involving only one transport process. The transfer probabilities for $N \geq 2$ and imperfect transmission are always smaller than in the normal conducting case, because a higher-order process, multiplicatively depending on T, is necessary in order to transfer charge. To transfer huge charge quanta, N, with sufficient probability, very high transmission is necessary, since many Andreev reflections are involved in such a process. Thus, for larger N which, in our model, directly corresponds to small voltage bias (see Equation 8.6) nonzero probabilities shown in the left panel of Figure 8.7 are more and more shifted to the high-transmission regime.

From the cumulant generating function we get the second cumulant

$$C_2 = N^2 \frac{2eVt_0}{h} P_N(1 - P_N) \tag{8.7}$$

which is proportional to the noise correlator. The expression $P_N(1 - P_N)$, which depends on transfered charge, or conversely on voltage, matches the one in the traditional shot-noise formula if we replace T by P_N. The expression $P_N(1 - P_N)$ is displayed in the right panel of Figure 8.7. We see that, for large N, or conversely, small voltages, the maximum is shifted and squeezed into the high-transmission regime.

The corresponding diagram which shows the noise, using the full expression (Equation 6.10), depending on transmission, is Figure 8.4.

So, altogether, we can distinguish two ingredients to the noise given in Equation 8.7. One is the expression $P_N(1 - P_N)$ we just discussed. Additionally, there is the prefactor $N^2(2eVt_0/h)$. If we take into account the relation between N and eV in our model, which is given in Equation 8.6, we see that this part results in noise enhancement that behaves approximately like $1/V$ in the small-voltage regime. As the noise is determined by the product of both parts, for a fixed transmission coefficient, there will be a voltage regime where the noise gets enhanced by lowering the applied voltage bias. However, at some voltage, or conversely for some N, the behavior of $P_N(1 - P_N)$ presented in the left panel of Figure 8.7 will overcompensate this increase and reduce the noise again. So, we can summarize that the toy model still explains the noise enhancement by an increased charge quanta, cf. discussion of the $T \ll 1$ case. The decrease of noise at very low voltage follows from the overcompensation of this effect of charge quanta enhancement by the decrease of transfer probability in the expression $P_N(1 - P_N)$.

In Figure 8.8, for comparison, the noise calculated using the full expression and the toy model at MAR voltages, is presented in one plot. We see that the toy model qualitatively shows the basic features of our numerical calculation with noise enhancement for decreasing voltage in the subgap regime up to a certain point, where the noise starts to decrease again. Nevertheless, there is a huge quantitative difference. Thus, we realize that the toy model is sufficient and good to understand the shape and characteristic of the noise curves as well as its physical origin, but it fails dramatically to give quantitative results. Thus, for quantitative calculations, which are necessary below, the extensive calculation used here is essential.

The final aspect we investigate is what is fundamentally driving the noise increase. In the toy model we reduced the actual multiprocess problem to a binomial one and we have seen that, in this model, the explanation of the noise enhancement is simply reduced to the increase of charge quanta transfered. We can now ask the question: What is the maximal noise for a certain voltage? This means, for fixed voltage bias, we use the transmission eigenvalue as a parameter to find the maximal noise. With respect to Equation 8.7 and its illustration in Figure 8.7, in the toy model, the maximum of the expression $P_N(1 - P_N)$ is always $\frac{1}{4}$. Thus,

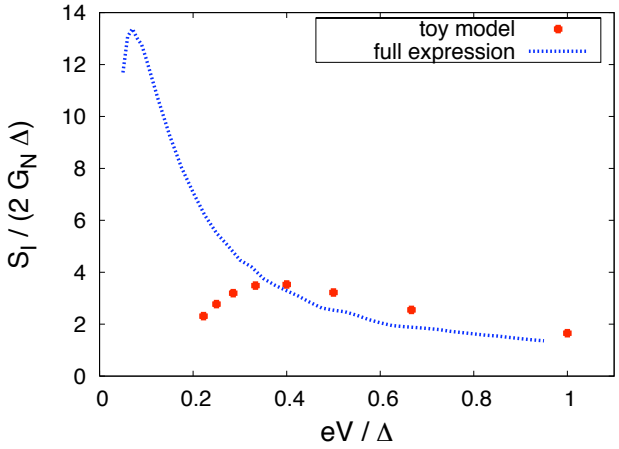

Figure 8.8: Comparison of the noise results calculated for a $T = 0.97$ single-mode QPC between superconductors as a function of bias voltage using either the full expression or the toy model.

here, the maximal noise $\max_T [S_I(T,V)]$ depends only on the prefactor given in Equation 8.7. Consequently, for small voltages, it approximately scales like $\frac{1}{V}$.

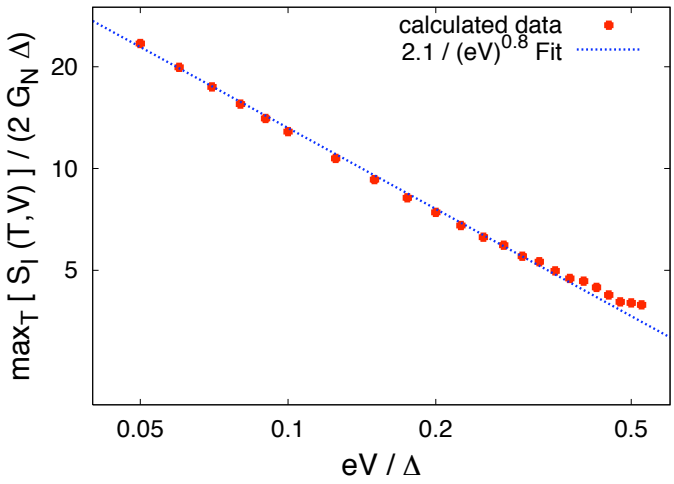

Figure 8.9: Maximal noise $\max_T [S_I(T,V)]$, optimized with transmission as a parameter, as a function of bias voltage on a double logarithmic scale for a single-mode QPC between superconductors. The calculated data using the full expression, Equation 6.10, are fitted using the given power law.

The question now is, how does the maximal noise behave performing a calculation with the full expression. In Figure 8.9, the maximal noise over all transmission eigenvalues for a given voltage $\max_T [S_I(T,V)]$ is plotted against voltage bias on a double logarithmic scale.

In the small-voltage regime, the data can be fitted extremely well using a power-law. We find

$$\max_T [S_I(T,V)] \propto \frac{1}{V^{0.8}}$$

Thus, although, as we have seen, that quantitative statements resulting from the toy model and from the full expression differ significantly, here we see that the maximal noise at given voltage follows a similar power law in the full expression as in the case of the toy model, if we just change the exponent from unity to 0.8. Hence, even in the much more complicated situation, including multiple MAR processes, the inherent $\frac{1}{V}$ dependence, which basically results from the increased charge quanta due to MAR, seems to be incorporated and a characteristic feature of noise enhancement.

8.4 Noise of tunnel junctions containing pinholes

After discussing homogeneous contacts and their noise features, we come back to our original goal of investigating rough superconducting tunnel junctions containing a small number of pinholes. For this reason, we continue considering the model of Section 7.4. There, we looked at a contact with M transport channels, each having either transmission eigenvalue $T_1 = 0.986$ or $T = 0.01$ and eigenvalue distribution

$$\rho(T) = a\delta(T - T_1) + (1 - a)\delta(T - T_2).$$

The variable a determines the small ratio of pinholes among the number of transport channels. Here, we are concerned with the noise generated in this kind of junction. Figure 8.10 shows the calculated results.

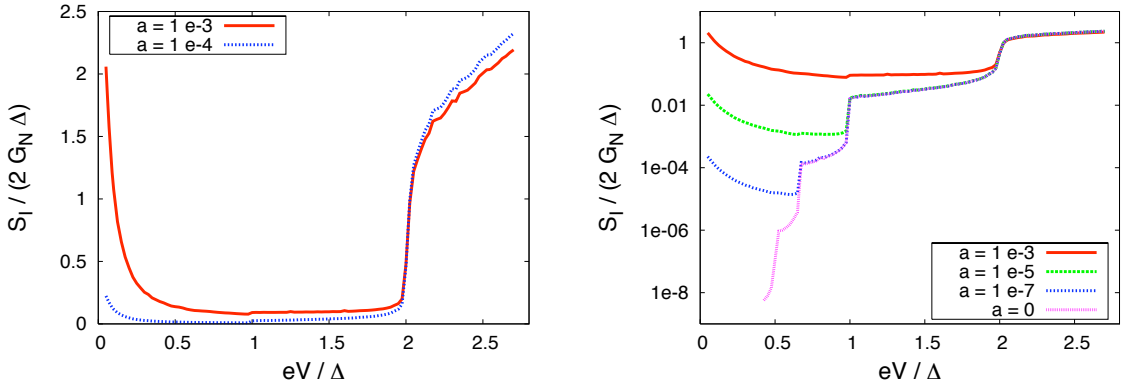

Figure 8.10: Noise S_I as a function of bias voltage for a rough superconducting tunnel junction including pinholes, characterized by the transmission eigenvalue distribution $\rho(T) = a\delta(T - T_1) + (1-a)\delta(T-T_2)$, $T_1 = 0.986$ and $T = 0.01$. The different curves refer to different pinhole fractions within all transport channels, given by the parameter a. Left panel: normal noise scale. Right panel: logarithmic noise scale.

We see a dramatic change in the noise characteristic of tunnel junctions due to very few pinholes with an enormous noise increase at small voltages. As in the case of leakage current,

at some point in the small-voltage regime, the ratio of pinholes begins to dominate the noise characteristic, see right panel of Figure 8.10. In this range, S_I is solely carried by the pinhole fraction and we see the enormous rise of noise, as discussed in Section 8.3, introduced by only a very small ratio of pinholes contained in the junction.

We note again that, as explained in Section 7.4, sensitive measurements of the leakage current will supply us with a threshold on the fraction of pinholes that might be contained in the considered junction. Together with the junction size and the number of channels we then might rule-out the existence of pinholes and the effect presented here in the case of a specific junction.

The considered pinhole eigenvalue of $T = 0.986$ is an example chosen due to the considered voltage regime going down to $eV = 0.05\,\Delta$ (see Appendix C). Nevertheless, considering the explanations given in Section 8.3, we can add two more aspects: Firstly, for smaller voltages than given in Figure 8.10, the noise will show a maximum and then will fall off again. Secondly, considering higher values of transmission will lead to an even steeper and higher ascent, which will, however, start at smaller voltages.

Chapter 9

Full Counting Statistics of Pinholes

We will investigate the *full counting statistics* (FCS) of charge transport through pinholes. This crucially depends on the measurement time t_0. It has to be chosen sufficiently short so that we do not lose most structure due to individual transport processes in the statistics but on the other hand, has to be considerably longer than the inverse of the Josephson frequency. Despite this limited window of measurement time, we will show that it is nevertheless feasible to resolve non-Gaussian peak structure in the FCS of pinholes. Using this deep insight into the transport process, we will furthermore discuss a possible model of high transmission channels as microscopic origin of two-level current fluctuators. Due to different MAR processes, this scenario could be an additional source of junction resonators, see Ref. [38], even though in practice, other processes like charge-trapping might be much more relevant. Indeed, for certain voltage parameters the FCS will show two-level peak structure but, although tempting at first sight, a more detailed analysis will show that this *cannot* be related to distinct MAR processes. Hence, we will find the result that given the dc part of the probability distribution, see Section 6.2, there is no evidence that a pinhole might introduce an additional source of two-level current fluctuators. Finally, we will present an alternative, consistent interpretation of the observed peak structure in terms of successful transmission attempts of Andreev clusters.

9.1 Full Counting Statistics and Cumulant Generating Function

Given the definition of the cumulant generating function, Equation 2.1,

$$\exp\left[S(\chi)\right] = \sum_N P(N) \exp(iN\chi),$$

it is clear that we can get the full counting statistics, the probability to transfer a total number of N charge during the measuring time t_0, by a Fourier transformation

$$P(N) = \frac{1}{2\pi} \int_{-\pi}^{\pi} d\chi \; e^{-iN\chi} \exp\left[S(\chi)\right].$$

As presented before, the cumulant generating function in the considered case reads

$$S(\chi) = \frac{2t_0}{h} \int_0^{eV} dE \; \ln\left[1 + \sum_{n=0}^{\infty} P_n(E,V,T)\left(e^{in\chi} - 1\right)\right],$$

where the probabilities $P_n(E,V)$ have to be calculated numerically as explained above. Thus, altogether we can write the full counting statistics as

$$P(N) = \frac{1}{2\pi}\int_{-\pi}^{\pi} d\chi\, e^{-iN\chi} \exp\left(\frac{2t_0}{h}\int_0^{eV} dE\ \ln\left[1+\sum_{n=0}^{\infty} P_n(e^{in\chi}-1)\right]\right)$$

$$= \frac{1}{\pi}\int_0^{\pi} d\chi\, \mathrm{Re}\left\{e^{-iN\chi}\exp\left(\frac{2t_0}{h}\int_0^{eV} dE\ \ln\left[1+\sum_{n=0}^{\infty} P_n(e^{in\chi}-1)\right]\right)\right\}. \qquad (9.1)$$

9.2 Full Counting Statistics of high transmission channels

We have seen in the previous sections that, for rough superconducting tunnel junctions including a small number of pinholes, current and noise characteristics in the low voltage bias regime are dominated by the incorporated high transmission channels. Thus, here we will focus on the features of this kind of transport channels and we will investigate their properties with respect to the full counting statistics.

To calculate the probability distribution, we have to set the measurement time t_0. We commented on this time before when we derived the cumulant generating function of a voltage biased Josephson Junction, see Section 6.2. This issue was significantly complicated due to the ac Josephson effect. In order to make calculation feasible, and to prevent us from the (in Chapter 2) already mentioned interpretation difficulties of arising 'negative probabilities' [47] in our superconducting system, we set the dc part ϕ_0 of the superconducting phase $\phi(t) = \phi_0 + \frac{2eV}{\hbar}t$ to zero. For sufficiently long measuring times this procedure is justified because the matrix current

$$I(\chi,t) = \sum_n I_n(\chi)e^{in\phi(t)},$$

which entered the derivation of the cumulant generating function (see Equation 4.12), only integrated over measurement time t_0, oscillates with all harmonics of the Josephon frequency, while the coefficients $I_n(\chi)$ are independent of ϕ_0. Thus, ϕ_0 drops the calculation if t_0 is sufficiently longer than the inverse of the Josephson frequency $T_{Josephson}$. This makes the derivation of the FCS feasible and enables a classical, and therefore accessible, interpretation of the probability distribution in our superconducting case. Consequently $T_{Josephson}$ sets a time scale in our approach and there is a lower bound for the measurement time.

We consider a contact with transmission eigenvalue $T = 0.936$ and examine three bias voltages: above the gap $eV = 2.2\Delta$, not too far from the energy gap $eV = 1.5\Delta$ and low voltages $eV = 0.3\Delta$ where qubits might be operated. To start with, we consider two different measurement times $t_0 = 10 \cdot T_{Josephson}$ and $t_0 = 100 \cdot T_{Josephson}$. Figures 9.1 to 9.3 show the results.

We see that in every case the FCS for the long measurement time $t_0 = 100 \cdot T_{Josephson}$ is a Gaussian. The average and variance of this is exactly the first and second cumulant respectively, which are given by the cumulant generating function in the accordant case. For the two voltage biases $eV = 2.2\ \Delta$ and $eV = 1.5\ \Delta$ the FCS, in the case of smaller measurement time $t_0 = 10\ T_{Josephson}$, is as well nearly Gaussian. Both results are solely slightly tilted against this form. More interesting is the case of small measurement time t_0 for low voltage bias $eV = 0.3\ \Delta$ in Figure 9.3. Here we see a rich comb structure.

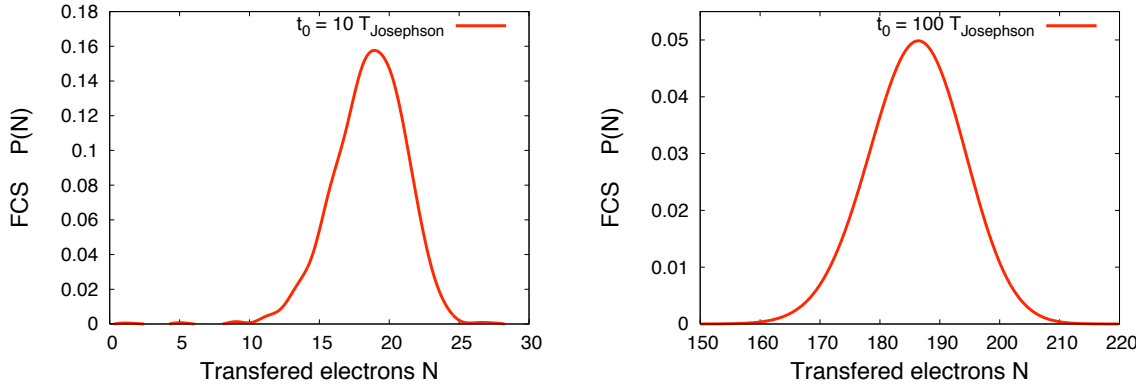

Figure 9.1: FCS for a transport channel between superconductors with transmission $T = 0.936$ and voltage bias $eV = 2.2\Delta$. Left panel: measurement time $t_0 = 10 \cdot T_{Josephson}$. Right panel: measurement time $t_0 = 100 \cdot T_{Josephson}$

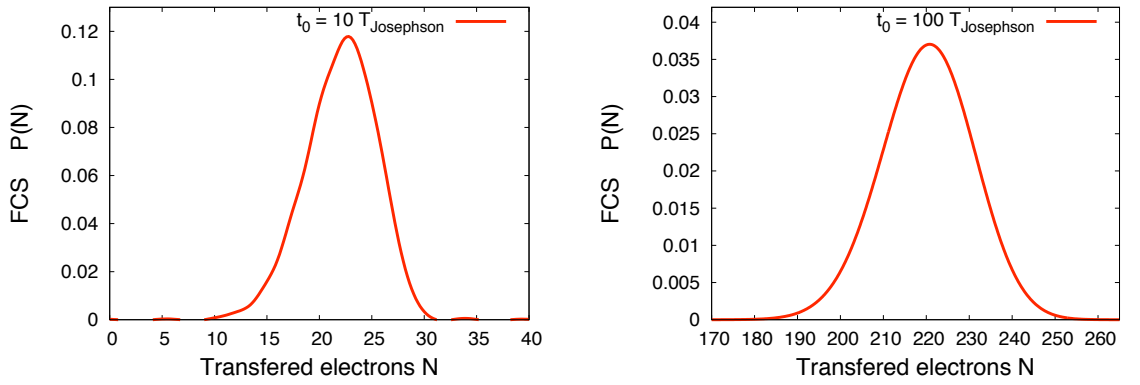

Figure 9.2: FCS for a transport channel between superconductors with transmission $T = 0.936$ and voltage bias $eV = 1.5\Delta$. Left panel: measurement time $t_0 = 10 \cdot T_{Josephson}$. Right panel: measurement time $t_0 = 100 \cdot T_{Josephson}$

We will discuss this comb structure and its origin in detail later on, but intuitively we can already anticipate that it is related to MAR transport processes transferring large charge quanta like encountered in previous chapters. Here, we want to point out that this structure turns into a Gaussian for long measurement times. This is as we would expect because, if we sum the number of transfered charges over a very long measurement time it will become possible, instead of considering individual MAR processes with their specific probabilities, to just assign an average probability for one elementary charge quantum to be transfered. Thus, in the long measurement time limit, transport can be described by a sum of many independent and identically-distributed events, namely transfer of an elementary charge quantum, which results in a Gaussian. This is the essence of the central limit theorem extensively used in statistical physics. Indeed, the problem above can be related to the concept of *quasi-ergodic*

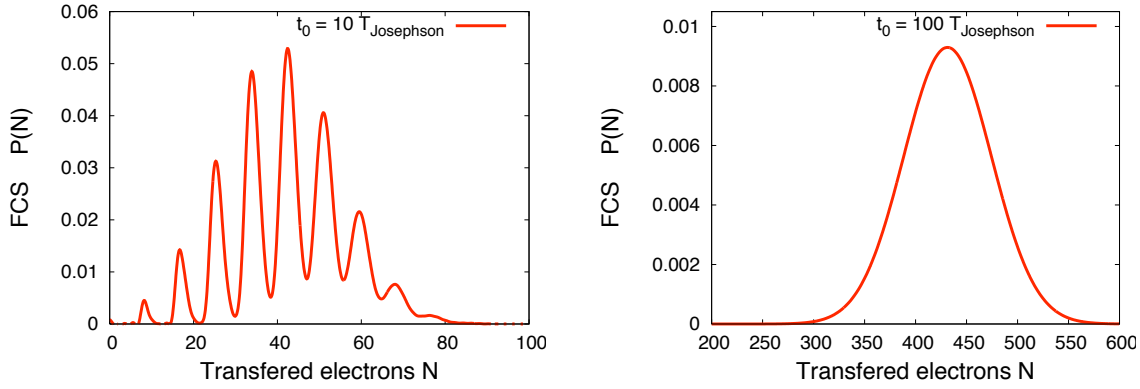

Figure 9.3: FCS for a transport channel between superconductors with transmission $T = 0.936$ and voltage bias $eV = 0.3\Delta$. Left panel: measurement time $t_0 = 10 \cdot T_{Josephson}$. Right panel: measurement time $t_0 = 100 \cdot T_{Josephson}$

hypothesis, see for instance Ref [79], which constitutes the basis of the essential thermodynamic limit. Hence, it is clear that for very long measurement times the comb structure due to individual, discrete transport processes is washed out. In the additionally considered cases of $eV = 2.2\ \Delta$ and $eV = 1.5\ \Delta$, see Figure 9.1 and 9.2, the most relevant transport processes transfer only very small charge quanta whose discrete structure in the FCS cannot be resolved in the used time interval. Therefore, even with a measurement time of just $t_0 = 10 \cdot T_{Josephson}$ we see a nearly Gaussian distribution.

So the central question is how far the measurement time can be reduced. We have mentioned above that, for very small detection intervals, we are running into problems with the approximations we made on our way to derive the FCS in our superconducting case. For long measurement time, we saw that we lose the peak structure and we cannot resolve structures due to individual, discrete transport processes that reflect information contained in higher cumulants. Despite this window of possible or rather interesting times, we are able to see discrete structure in the FCS and we can use it to gain information from it. We can use normalization of the probability distribution to roughly verify that our values of t_0 are still sufficiently long. In all calculations that we performed, for very small measurement times at some point the shape of the calculated probability distribution becomes unreasonable and the resulting FCS diverged significantly from its usual normalization to unity. We used this as a criterion bounding the measurement time to figure out how short it can be chosen for a given set of parameters. As an example, for smaller measurement times in Figure 9.4 the FCS for a channel with transmission $T = 0.972$, voltage bias $eV = 0.3\ \Delta$ and detection period $t_0 = 6 \cdot T_{Josephson}$ is shown.

9.3 Pinholes as Junction Resonators

9.3.1 Motivation

So far we have seen that, in spite of the limitations on the measurement time t_0, we are able to resolve pronounced structures in the FCS for high transmission transport channels. In

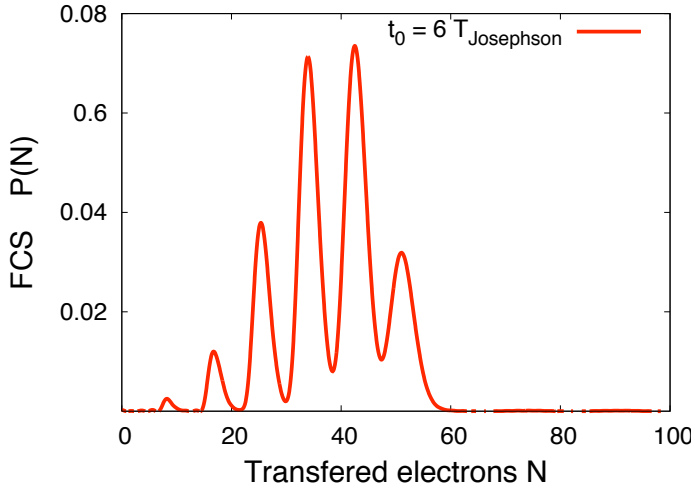

Figure 9.4: FCS for a transport channel between superconductors with transmission $T = 0.972$ and voltage bias $eV = 0.3\ \Delta$ for a measurement time $t_0 = 6 \cdot T_{Josephson}$

particular we have shown several discrete peaks in the probability distribution in case of low subgap voltage for high transmission channels, which as pinholes might reside hidden in huge tunnel junctions. We note the obvious fact that discrete probabilities to transfer different total numbers of charge during the measurement time t_0 result in discrete probabilities for different, distinct values of average current flow.

One of the original motivations of this research was decoherence from junction resonators in phase qubits. It was measured in Ref. [38] and hence, we are especially interested in the microscopic origin of systems that might cause two-level current fluctuators. Moreover, this is particularly relevant in trying to reveal sources of 1/f noise, see Ref. [27, 28, 29] and the discussion in Section 1.4.1.

Thinking of the different possible MAR processes, which transfer different sizes of charge quanta, a pinhole might introduce current fluctuators: imagine a high transmission channel, i.e., a pinhole hidden in the junction. Two different MAR processes A and B transfer two different charge quanta $n_A e$ and $n_B e$ in each cycle. Thus, we might think of two current states $|A\rangle$ and $|B\rangle$; each of them carry charge using one of the different MAR processes A, B. Due to the different Andreev clusters being transfered, the two states will cause two different currents. In principle the mechanism is similar to the idea of charge-trapping in Ref. [29], where a, for instance by defects, trapped charge blocks tunneling through a transport channel. One introduces an untrapped state $|\tau_u\rangle$ causing high current and a trapped state $|\tau_t\rangle$ causing low current. In comparison, we suggest two states $|A\rangle$ and $|B\rangle$ corresponding to two different MAR processes and thereby causing two different currents.

9.3.2 Calculation

If such a system is actually generated by a pinhole we expect to find two distinct peaks p_A and p_B in the FCS, where probability p_A refers to charge transport due to MAR process A within time interval t_0 and p_B to MAR process B. Hence, let us see whether we find parameters

that result in such an FCS.

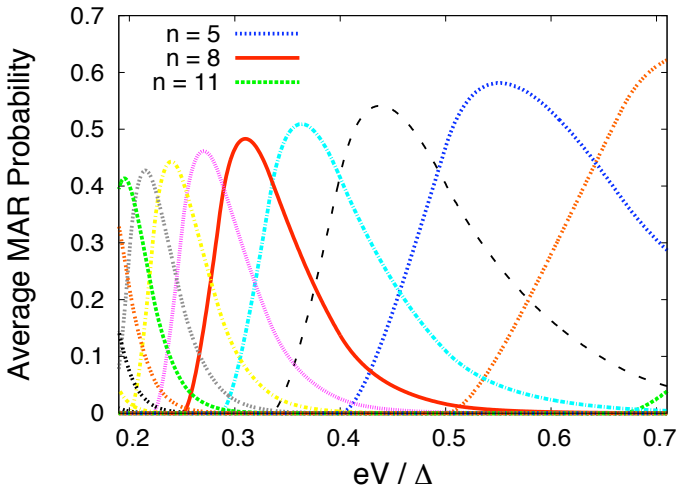

Figure 9.5: Average MAR probabilities $\bar{P}_n = \frac{1}{eV}\int_0^{eV} dE\, P_n$ as function of applied voltage bias for a perfect transmission channel $T = 1$. (To improve readability we only labeled every third process orders n).

We consider very high transmission channels, for instance $T = 0.99$. We have seen before that the MAR probabilities $P_n(E, V, T)$ depend very sensitively on parameters (see Figure 8.5 and 8.6). Although by looking at average MAR probabilities $\bar{P}_n = \frac{1}{eV}\int_0^{eV} dE\, P_n$ (see Section 7.3), we disregard much information (see Chapter 8), we use them to get a first hint at what kind of voltages we might find a two peak structure in the FCS. In Figure 9.5 we see that in the case of of perfect transmission, there are points, always close to MAR voltages, where two curves cross with the same probability and the subsequent processes have a much smaller probabilities than the other two. Here we use the extreme case of perfect transmission as representative for high transmission channels. In fact, as we have seen in Chapter 8, $\bar{P}_n$ curves in the high transmission regime do not differ significantly.

We calculate the FCS for some of these voltages and the transmission eigenvalue $T = 0.99$. The results are shown in Figure 9.6. Actually, for some of these parameters, we find two very pronounced peaks in the FCS. We call them p_A and p_B. Note that here the measurement time is very short but, despite some artifacts in the diagrams, the distribution still has a normalization close to unity.

9.3.3 Interpretation in terms of two-level fluctuator

So given these pronounced peaks, does this indicate that a pinhole via its different MAR processes can actually introduce a two-level current fluctuator? If we assume so, we associate peak p_A with the case where charge transport is carried by charge quanta $n_A e$, in the time interval t_0, and p_B with the case of transport using charge quanta $n_B e$. In all the probability distributions in Figure 9.6 we see a sharp boundary for the appearance of peaks for large total charge numbers N. In contrast to such an boundary to the right, in some plots we see a little peak on the left of the dominating ones. Under the assumption made above, this sharp

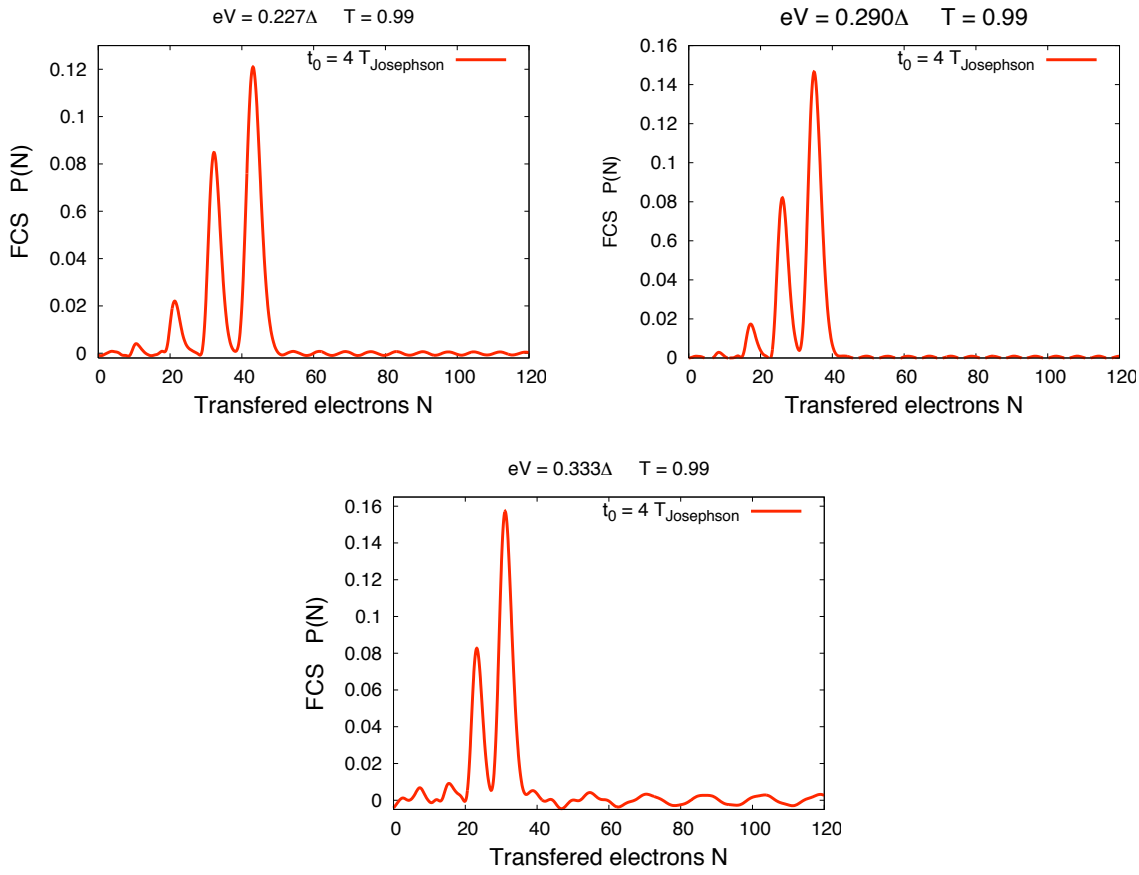

Figure 9.6: Set of FCSs for a transport channel between superconductors with transmission eigenvalue $T = 0.99$ and voltage bias $eV = 0.227\Delta$, $eV = 0.290\Delta$ and $eV = 0.333\Delta$, respectively, showing a double peak structure. The measurement time is $t_0 = 4 \cdot T_{Josephson}$.

boundary is surprising because, for a given voltage there is in fact a *lower* threshold for the MAR order n, i.e., a *lower* bound on the minimal charge cluster transferred in each MAR cycle. Although there might be the two very dominant processes A and B, there will also be finite probability to transfer higher charges which would result in little peaks on the right. So the two-level interpretation, given the above, identifying each peak with different MAR processes, is not consistent with the sharp boundary for peaks at large total charge number N that we see in all the FCSs.

The second aspect is the spacing between the peaks. For all the distributions in Figure 9.6, the distance is slightly larger than $(2\Delta/eV + 1)$. With respect to the MAR threshold, this is roughly the size of the average charge quantum that we would expect to be transferred by one Andreev cluster. Looking at the number of, in total, transferred charges of each rightmost peak in all distributions in Figure 9.6 and, additionally, noting the MAR threshold $2\Delta/eV$ i.e., the minimum Andreev cluster size, we infer that, within the measurement time t_0, roughly 5 MAR processes contributed to all the three rightmost peaks. The discussion in Section 7.3 strongly suggests that, in the above two-level scenario, A and B are adjacent MAR processes meaning their transferred charge quanta differ only in one elementary charge. (See also the

order of processes n whose $\bar{P}_n$ curves cross at equal probabilities in Figure 9.5). Thus, if a pinhole introduced a two-level current fluctuator in the way suggested above, in Figure 9.6 we would expect a peak spacing of $\Delta N = 5$ elementary charge quanta rather than a value larger than $(2\Delta/eV + 1)$.

9.3.4 Alternative, consistent interpretation

Thus, the structure we have seen in the FCS of a pinhole does not strictly correspond to the scenario of a two-level current fluctuator, due to different MAR processes, as suggested above. In fact, the description of the probability distribution becomes consistent if we do not identify each peak with different MAR processes but, with the total number of attempts being successful to transmit Andreev cluster: within the measurement time t_0 we might think of a total number of attempts to transfer charge cluster, where the actual size of the quantum might differ due to different MAR processes. In the distributions in Figure 9.6, each rightmost peak corresponds to the case where every attempt is successful to transfer an Andreev cluster, so we get the sharp boundary observed for the appearance of peaks at large N. The next peak to the left corresponds to the case where exactly one attempt fails and so on. Thus, the peaks are naturally separated by a distance larger than $2\Delta/eV$, namely the average Andreev cluster size transferred in case of a successful attempt. Due to the individual MAR processes, where in fact, the most likely ones differ only by one or two elementary charge quanta, the pronounced peaks of successful attempts are broadened. This description is also consistent with the distribution in Figure 9.4. The peak spacing is again given by a value slightly larger than $(2\Delta/eV + 1)$ and we seem to have a sharp boundary for peaks to the right. Due to the fact that, in comparison to Figure 9.6, we have a smaller transmission eigenvalue, the rightmost peak, corresponding to the case where all attempts have been successful, is not the one with the highest probability.

9.3.5 Conclusion

To summarize this section, we have discussed the possibility of a pinhole to introduce a two-state current fluctuator due to its different MAR transport processes. This is conceptually similar to the mechanism of charge-trapping, Ref. [29]. Although at a first sight it is tempting to relate the observed peak structure to different MAR processes, we have shown that a more detailed analysis suggests a very different, consistent interpretation in terms of successful transport attempts of Andreev cluster. Actually, at first, this was not immediately obvious to us. Taking this into account, within the dc part of the probability distribution, see Section 6.2, we see no clear evidence that a pinhole might be a microscopic origin for introducing two-level current fluctuators. Charge-trapping in junctions is probably one of the most relevant mechanisms. However, it might be especially interesting to think about such a process opening and closing a very high transmission channel i.e. a pinhole. Due to the large charge quanta transfered, the process of trapping and untrapping might result in much higher magnitudes of current fluctuations. So far, electron-electron interacting has not been taken into account. A very intuitive picture might be an occupied upper Andreev bound state with energy E_{J+}, see Ref [80], that causes such a repulsion within the channel. Nevertheless, in the case of voltage bias, such a state with energy $E_{J\pm} = \pm\Delta[1 - T\sin^2(\phi(t)/2)]^{1/2}$, where subscript E_{J-} additionally refers to the lower bound state and $\phi(t)$ is the superconducting phase, might be adiabatically carried above the gap directly after population within the actual Josephson

cycle. Further investigation might clarify this aspect.

Conclusion

We have investigated voltage-biased *rough superconducting tunnel junctions* containing some high transmission channels, so-called *pinholes*, through the junction. We have done this using the method of full counting statistics formulated within the non-equilibrium Keldysh Green's functions technique. By reason of this microscopic, field-theoretical approach, we were able to properly quantify physical effects due to low- *and high-* transmission channels.

We explored *leakage current*, i.e., current in the subgap voltage regime $eV < 2\Delta$ of such systems. We discussed that charge transport through pinholes is effectively carried by various MAR processes, transferring Andreev clusters of different sizes. In contrast, for low-transmission channels, there is always a single strongly dominant MAR process, transferring charge clusters of a single specific size, depending on voltage. We have confirmed the intuitive result that the current contribution of high-transmission modes is larger than the one due to low-transmission channels by orders of magnitude. We were able to properly quantify this contribution to tunnel junctions for all values of transmission coefficients. We observed that such a junction of a given leakage characteristics may contain much fewer pinholes than previously speculated in Ref. [33]. We further demonstrated how highly sensitive current measurements can clarify the existence of pinholes and set boundaries to their fraction in all transmission channels. We pointed out that current measurements, done for the junction of the superconducting qubit device in Ref. [38], do not strictly rule out the existence of a pinhole hidden in the junction.

Furthermore, we examined *noise* properties. For voltage bias above or slightly below the gap edge we found that a rough superconducting tunnel junction behaves much like a tunnel contact. However, we demonstrated that even very few of these pinholes give rise to a drastic increase of the noise in the very low subgap voltage regime. The height and the position of the emerging noise maximum depend on the transmission coefficient of the actual pinhole. In fact, higher values of transmission lead to a higher and steeper noise ascents which, however, occur at smaller voltages. Although, for pinholes, details of this noise enhancement, comprising contributions of several, different MAR processes, turned out to be quite complicated, we proposed that the physical essence of the observed noise boost still lies in the increased charge quanta that is transfered. We compared the explicit noise calculation to a simple model containing this essential feature but no further details. This showed qualitative agreements, and thus illuminated some essential features, but failed quantitatively, therefore demonstrating the need of detailed calculations to obtain our results. Moreover, similar to previous authors, we observed finite shot noise in perfect transmission channels between superconductors, that is completely different from what we would anticipate from the normal conducting case. We have explained this feature in terms of the additionally

introduced uncertainty of the actual Andreev cluster size, by reason of several possible MAR processes. Furthermore, we calculated explicit results for the junction measured in Ref [30], see Figure 1.5. We confirmed that, in this transmission eigenvalue regime, it is still valid to use the simple picture of Poissonian shot noise $2qI$ with modified charge quantum q.

Finally, we investigated the *full counting statistics* (FCS) of charge transport through pinholes. This crucially depends on the measurement time t_0. To obtain a classical, and therefore accessible, interpretation of the FCS in our superconducting case, this time must not be chosen too short. For long detection times, we demonstrated that we lose most structure, due to individual transport processes, in the statistics. Despite this window of limited measurement time, we showed that it is nevertheless feasible to resolve non-Gaussian peak structure in the FCS of a pinhole. Using this deep insight into the transport process, we discussed a possible model of high-transmission channels as a microscopic origin of two-level current fluctuators. Due to different MAR processes, this scenario could have been an additional source of junction resonators, see Ref. [38], even though in practice, other processes like charge-trapping might be much more relevant. Indeed, for certain voltage parameters, the FCS showed a two-level peak structure. Nevertheless, although tempting at first sight, from a more detailed analysis we inferred that this structure *cannot* be related to charge transport by distinct MAR processes. Hence, we found the result that, given the dc part of the probability distribution (see Section 6.2), there is no evidence that a pinhole might introduce an additional source of two-level current fluctuators. In addition, we presented an alternative, consistent interpretation of the observed peak structure in terms of successful transmission attempts of Andreev clusters.

So far, although the method we used provides much insight into the microscopic transport process, it is basically limited to the stationary or quasi-stationary case. Further improvements on this might incorporate time-dependence into the Keldysh Green's function approach. This may permit a more rigorous discussion of finite-frequency noise with respect to pinholes. Very recently, first steps concerning the discussion of time-dependence using this method have been made see Ref. [81], where elementary events in the statistics of a normal conducting QPC driven by an arbitrary time-dependent voltage bias were discussed. Also, electron-electron interactions describing the traditional 1/f noise scenario for Josephson junctions should be included as mentioned in Section 9.3.5.

Acknowledgments

I am deeply grateful to my supervisor Dr. Frank K. Wilhelm, Associate Professor at the University of Waterloo, for giving me the opportunity to do research at the Institute for Quantum Computing (IQC), for his support and advice concerning physical and non-physical issues. Frank, I very much enjoyed working with you; not only because of your great supervision but also due to your very likable kind.

I would like to thank Prof. Dr. Jan von Delft, Professor at the University of Munich, for his official support making it possible to write this external LMU Diploma thesis. I am furthermore thankful to Dr. Raymond Laflamme, director of the IQC, and Dr. Robert Mann, chairman of the Department of Physics & Astronomy, University of Waterloo, for the invitation to come to Canada.

I am very grateful to the entire QDT group and members of the IQC for there support and for making may stay very pleasant. Especially, I would like to thank Austin, Bill, Chris, Tobias, Martin, Ioana, Hauke, Jonathan, Brendan and Devin.

At the end of my studies I would like to thank the Studienstiftung des deutschen Volkes for my scholarship and the extremely stimulating sponsorship. In particular, I am thankful to Prof. Dr. Angelika Schnieke, Professor at the Technical University of Munich, for her continuous support.

Last, but not least, very special thanks to my parents for all their support and dedication throughout all the years. Much love to both of you.

Appendix A

Bulk solutions

It took us a while to find the correct bulk solutions in the superconducting case as there seems to be different sign conventions in the literature. Thus it might be useful to discuss this issue in some detail. We will use the Keldsh(^)-Nambu($^-$) notation introduced in Section 6.1.

A.1 Normal conductor

The bulk solution of a normal conducting terminal, see for example Ref. [70, 65], is given by,

$$\check{G} = \begin{pmatrix} \bar{R} & \bar{K} \\ 0 & \bar{A} \end{pmatrix} \tag{A.1}$$

with

$$\bar{R} = \bar{\sigma}^3$$

$$\bar{A} = \bar{\sigma}^3$$

$$\bar{K} = 2 \begin{pmatrix} 1-2f(E) & 0 \\ 0 & 1-2f(-E) \end{pmatrix}.$$

Here f(E) is the Fermi function. Sometimes this solution is stated using the equation $\tanh(x/2) = 1-2f(x)$. Note that the Keldysh Green's function in Equation A.1 is given in its triangular form, see remark at the end of Section 3.1 and Appendix B.1.

A.2 Superconductor

A.2.1 Bulk solutions in the literature

In nearly all references on full counting statistics in the superconducting case, see for instance Ref. [47, 74, 65], the bulk solution of the Usadel equation (see Section 3.2.1), for BCS superconductors at zero potential $\mu_S = 0$ is stated as

$$\check{G}_S(E) = \begin{pmatrix} (\bar{A}-\bar{R})f + \bar{R} & (\bar{A}-\bar{R})f \\ (\bar{A}-\bar{R})(1-f) & (\bar{R}-\bar{A})f + \bar{A} \end{pmatrix} \tag{A.2}$$

with Nambu structure

$$\bar{R}, \bar{A} = g^{R,A}\bar{\sigma}^3 + f^{R,A}\bar{\sigma}^1$$

$$f^{R,A} = \frac{i\Delta}{\sqrt{(E \pm i\delta)^2 - \Delta^2}} \tag{A.3}$$

where f refers to the Fermi function, Δ denotes the superconducting gap and $\delta = 0^+$. Note that different forms of Equation A.2, that can be found in the literature, usually depend on whether or not the Keldysh Green's function is given in its triangular from (see also Appendix B.1). Given Equation A.3, $g^{R,A}$ should follow from quasiclassical normalization, $g^2 + f^2 = 1$. Here, in this representation, δ is necessary to choose the correct signs when doing square roots. If we do this calculation, using Equation A.3 and including the limit $\delta = 0^+$, we find the explicit representation of the bulk solution

$$\begin{aligned} \bar{R}(\bar{A}) &= \bar{\sigma}^3 \left[\pm \frac{|E|}{\sqrt{E^2 - \Delta^2}} \delta(E^2 - \Delta^2) + i \frac{-E}{\sqrt{\Delta^2 - E^2}} \delta(\Delta^2 - E^2) \right] \\ &+ \bar{\sigma}^1 \left[\frac{\Delta}{\sqrt{\Delta^2 - E^2}} \delta(E^2 - \Delta^2) \pm i \frac{\Delta}{sign(E)\sqrt{E^2 - \Delta^2}} \delta(\Delta^2 - E^2) \right]. \end{aligned} \tag{A.4}$$

It turns out that Equation A.4 is exactly the solution found in one of the very early reviews on kinetic equations for superconductors, see Ref. [58]. From Equation A.3 and A.4 it follows that

$$f^A = -(f^R)^* \tag{A.5}$$

However, our calculations of Equation 6.10 using Equation A.4 failed. For this reason we look at the extensive review in Ref. [41].

A.2.2 Used bulk solution

In Ref. [41] the derivative of the bulk solution for the Usadel equation in case of BCS superconductors at zero potential $\mu_S = 0$ results

$$\begin{aligned} \bar{R}(\bar{A}) &= \bar{\sigma}^3 \left[\pm \frac{|E|}{\sqrt{E^2 - \Delta^2}} \delta(E^2 - \Delta^2) + i \frac{-E}{\sqrt{\Delta^2 - E^2}} \delta(\Delta^2 - E^2) \right] \\ &+ \bar{\sigma}^1 \left[\frac{\Delta}{\sqrt{\Delta^2 - E^2}} \delta(\Delta^2 - E^2) \pm i \frac{\Delta}{sign(E)\sqrt{E^2 - \Delta^2}} \delta(E^2 - \Delta^2) \right]. \end{aligned} \tag{A.6}$$

Note that here, in comparison with Equation A.4, the delta functions in the anormalous propagator part are interchanged. Thus, instead of Equation A.5, we get

$$f^A = (f^R)^*.$$

We can rewrite Equation A.6 in a form similar to Equation A.3

$$\begin{aligned} g^{R,A} &= \pm \frac{|E|}{\sqrt{(E \pm i\delta)^2 - \Delta^2}} \\ f^{R,A} &= \pm \frac{i\Delta}{\sqrt{(E \pm i\delta)^2 - \Delta^2}} \end{aligned} \tag{A.7}$$

Apparently there must be different sign conventions involved. We used this solution that is consistently derived in Ref. [41] and we found consistent results using it.

Appendix B

Notes on computational details

B.1 Rotation in Keldysh space

It was already pointed out at the end of Section 3.1 that the components of the Keldysh Green's function, in its original form (Equation 3.7), are not linearly independent and can be transformed into a triangular form similar to Equation A.1. The transformation can be found in Ref. [41]. Here, we want to point out that the rotation in Keldysh space incorporating the counting field (Equation 6.2)

$$\check{G}(\chi) = e^{-i\chi\check{\tau}_k/2}\,\check{G}(0)\,e^{i\chi\check{\tau}_k/2}$$

naturally depends on the representation of the Green's function. The τ^3 coupling, see Section 3.1.1 and 4.2, requires a representation as in Equation 3.7. In fact, we calculated the normal conducting QPC using the bulk solution A.1 in its triangular form. In this case, the rotation axis is changed to τ^1. If we use τ^3 under these circumstances the counting field will actually drop out calculations due to the wrong rotation axis.

B.2 Toy model

We do not want to repeat the entire calculation of the toy model, introduced in Ref. [74] to illustrate the calculation of the cumulant generating function in a strongly simplified case. For this we refer to the mentioned reference. Nevertheless, we want to point out some additional remarks since we think the computational details are not very easily understandable and there are some misprints at the beginning of section III.3 in this paper that complicate its accessibility.

In the remainder of this section we will exclusively talk about labels of equations in Ref. [74] and it should be read in parallel with section III.3 of that paper. We consider only MAR voltages $eV = 2\Delta/n$. At each of these voltage we only consider the MAR process transferring $N = 2\Delta/n + 1$ charge quanta. Note that a process transferring $2\Delta/n$ quanta only connects the gap edges. An odd (even) number N means that we can subdivide the energy gap into an even (odd) number of energy intervals of length eV. In section III.3 it is best to set the energy offset such that we have for the chemical potential of the left terminal $\mu_L = -eV/2$ and for the one on the right $\mu_R = eV/2$. This way, in contrast to the derivation in section B, we have off diagonal elements in energy space for both terminal Green's functions and the subdivision of the energy gap 2Δ into intervals of length eV becomes

handy. Note that this way, the energy off-diagonal elements, see Equation 6.7 in this thesis, become $\delta(E - E' \pm 2\mu_{L,R}) = \delta(E - E' \pm eV)$. For odd N we use the fundamental interval $[-eV/2, eV/2]$ and introduce M such that $N = 2M + 1$. For even N we use the interval $[0, eV]$ and $N = 2(M + 1)$. This way Table II and Equation (40) become consistent with the description. Now, Equation (40) can be easily understood with Equation 6.7 in this thesis.

Appendix C

Numerics

Finally, to find concrete results, the probabilities $P_n(E, V, T)$, emerging in the expression of the cumulant generating function of the voltage-biase Josephson junction, had to be calculated numerically. According to Equation 6.10, this can be accomplished by an iterative procedure making use of the fact that for $|n| \gg \Delta/eV$ expressions like $g^{\alpha}_{\pm n} - g^{\alpha}_{\pm(n-1)}$, with $\alpha = A, R$, vanish and thus, we can use the boundary condition $B^{A,R}_n = \det \check{F}_n = 1$. We set an appropriate threshold ϵ for accuracy of the calculation. The physical reason that makes this iterative calculation feasible is that practically only energies around the Fermi energy contribute to transport.

Nevertheless, as it can already be guessed from the structure of Equation 6.10, the expressions, which finally always have to be integrated over energy, become very complicated and the software package *Maple 10*, which was used, was unable to do this kind of calculation. So we did this by choosing a certain number of equal-distant points within the energy interval $[0, eV]$, evaluated the integrand at these points and sumed the contributions multiplied by the point distance.

Additionally, the smaller the voltage bias, the more calculation steps are necessary to finally make use of the boundary condition. This number of steps increases in proportion to $1/V$. This becomes immediately clear if we look at the structure of Equation 6.10. Thus there is a lower limit for voltage bias due to computational effort. The smallest voltage we calculate is $eV = 0.05\Delta$.

Bibliography

[1] R. Landauer, Nature **392**, 658 (1998).

[2] W. Schottky, Ann. Phys. **362**, 541 (1918).

[3] S. Datta, *Electronic Transport in Mesoscopic Systems* (Cambridge University Press, Cambridge, 2005).

[4] Y. Blanter and M. Büttiker, Physics Reports **336**, 1 (2000).

[5] M. A. Nielsen and I. L. Chuang, *Quantum Computation and Quantum Information* (Cambridge University Press, Cambridge, 2000).

[6] D. Deutsch, Proc. R. Soc. Lond. A **400**, 97 (1984).

[7] C. H. Bennett and D. P. DiVincenzo, Nature **377**, 389 (1995).

[8] L. K. Grover, Phys. Rev. Lett. **79**, 325 (1997).

[9] D. P. DiVincenzo, Science **270**, 255 (1995).

[10] F. Schmidt-Kaler, H. Häffner, M. Riebe, S. Gulde, G. P. T. Lancaster, T. Deuschle, C. Becher, C. F. Roos, J. Eschner, and R. Blatt, Nature **422**, 408 (2003).

[11] C. Negrevergne, T. S. Mahesh, C. A. Ryan, M. Ditty, F. Cyr-Racine, W. Power, N. Boulant, T. Havel, D. G. Cory, and R. Laflamme, Phys. Rev. Lett. **96**, 170501 (2006).

[12] E. Knill, R. Laflamme, and G. Milburn, Nature **409**, 46 (2001).

[13] Y. Makhlin, G. Schön, and A. Shnirman, Rev. Mod. Phys. **73**, 357 (2001).

[14] V. Cerletti, W. A. Coish, O. Gywat, and D. Loss, Nanotechnology **16**, R27 (2005).

[15] L. M. K. Vandersypen, M. Steffen, G. Breyta, C. S. Yannoni, M. H. Sherwood, and I. L. Chuang, Nature **414**, 883 (2001).

[16] J. R. Friedman, V. Patel, W. Chen, S. K. Tolpygo, and J. E. Lukens, Nature **406**, 43 (2000).

[17] C. H. van der Wal, A. C. J. ter Haar, F. K. Wilhelm, R. N. Schouten, C. J. P. M. Harmans, T. P. Orlando, S. Lloyd, and J. E. Mooij, Science **290**, 773 (2000).

[18] I. Chiorescu, Y. Nakamura, C. J. P. M. Harmans, and J. E. Mooij, Science **299**, 1869 (2003).

[19] Y. Nakamura, Y. A. Pashkin, and J. S. Tsai, Nature **398**, 786 (1999).

[20] Y. A. Pashkin, T. Yamamoto, O. Astafiev, and Y. Nakamura, Nature **421**, 823 (2003).

[21] J. M. Martinis, S. Nam, and J. Aumentado, Phys. Rev. Lett. **89**, 117901 (2002).

[22] Y. Yu, S. Han, X. Chu, S.-I. Chu, and Z. Wang, Science **296**, 889 (2002).

[23] R. McDermott, R. W. Simmonds, M. Steffen, K. B. Cooper, K. Cicak, K. D. Osborn, S. Oh, D. P. Pappas, and J. M. Martinis, Science **307**, 1299 (2005).

[24] M. Tinkham, *Introduction to superconductivity* (Dover Publications, Inc., New York, 2004).

[25] M. R. Geller, E. J. Pritchett, A. T. Sornborger, and F. K. Wilhelm, in *Manipulating Quantum Coherence in Solid State Systems*, edited by M. E. Flatté and I. Tifrea (Springer, Dordrecht, 2005).

[26] F. K. Wilhelm, M. J. Storcz, U. Hartmann, and M. R. Geller, in *Manipulating Quantum Coherence in Solid State Systems*, edited by M. E. Flatté and I. Tifrea (Springer, Dordrecht, 2005).

[27] P. Dutta and P. M. Horn, Rev. Mod. Phys. **53**, 497 (1981).

[28] M. B. Weissman, Rev. Mod. Phys. **60**, 537 (1988).

[29] D. J. Van Harlingen, T. L. Robertson, B. L. T. Plourde, P. A. Reichardt, T. A. Crane, and J. Clarke, Phys. Rev. B **70**, 064517 (2004).

[30] P. Dieleman, H. G. Bukkems, T. M. Klapwijk, M. Schicke, and K. H. Gundlach, Phys. Rev. Lett. **79**, 3486 (1997).

[31] P. Dieleman, Ph.D. thesis, University of Groningen, 1998.

[32] G. Zaránd, G. T. Simányi, and F. Wilhelm, Phys. Rev. B **62**, 8137 (2000).

[33] A. W. Kleinsasser, R. E. Miller, W. H. Mallison, and G. B. Arnold, Phys. Rev. Lett. **11**, 1738 (1994).

[34] T. M. Klapwijk, G. E. Blonder, and M. Tinkham, Physica **109 - 110B**, 1657 (1982).

[35] G. E. Blonder, M. Tinkham, and T. M. Klapwijk, Phys. Rev. B **25**, 4515 (1982).

[36] M. Octavio, M. Tinkham, G. E. Blonder, and T. M. Klapwijk, Phys. Rev. B **27**, 6739 (1983).

[37] J. C. Cuevas and W. Belzig, Phys. Rev. Lett. **91**, 187001 (2003).

[38] R. W. Simmonds, K. M. Lang, D. A. Hite, S. Nam, D. P. Pappas, and J. M. Martinis, Phys. Rev. Lett. **93**, 077003 (2004).

[39] M. Steffen, M. Ansmann, R. McDermott, N. Katz, R. C. Bialczak, E. Lucero, M. Neeley, E. M. Weig, A. N. Cleland, and J. M. Martinis, Phys. Rev. Lett. **97**, 050502 (2006).

[40] Y. V. Nazarov, Ann. Phys. (Leipzig) **8**, 507 (1999).

[41] J. Rammer and H. Smith, Rev. Mod. Phys. **58**, 323 (1986).

[42] L. S. Levitov and G. B. Lesovik, JEPT Lett. **55**, 555 (1992).

[43] L. S. Levitov and G. B. Lesovik, JEPT Lett. **58**, 230 (1993).

[44] L. S. Levitov, H. Lee, and G. B. Lesovik, J. Math. Phys. **37**, 4845 (1996).

[45] R. Loudon, *The Quantum Theory of Light* (Oxford University Press, Oxford, 2000).

[46] Y. V. Nazarov and M. Kindermann, Eur. Phys. J. B **35**, 413 (2003).

[47] W. Belzig and Y. V. Nazarov, Phys. Rev. Lett. **87**, 197006 (2001).

[48] J. J. Sakurai, *Modern Quantum Mechanics* (Addison-Wesley Publishing Company, Inc., Reading, MA, 1994).

[49] L. S. Schulman, *Techniques and Applications of Path Integration* (Dover Publications, New York, 2005).

[50] H. Kleinert, *Path Integrals in Quantum Mechanics, Statistics and Polymer Physics* (World Scientific Publishing Co. Pte. Ltd., Singapore, 1995).

[51] W. P. Schleich, *Quantum Optics In Phase Space* (WILEY-VCH Verlag, Berlin, 2001).

[52] G. Rickayzen, *Green's Functions and Condensed Matter* (Academic Press, London, 1980).

[53] A. A. Abrikosov, L. P. Gorkov, and I. E. Dzyaloshinski, *Methods of Quantum Field Theory in Statistical Physics* (Dover Publications, Inc., New York, 1963).

[54] L. V. Keldysh, Sov. Phys. JETP **20**, 1018 (1965).

[55] J. Rammer and H. Smith, Rev. Mod. Phys. **58**, 323 (1986).

[56] R. D. Mattuck, *A Guide to Feynman Diagrams in the Many-Body Problem* (Dover Publication, Inc., New York, 1992).

[57] A. I. Larkin and Y. N. Ovchinnikov, Sov. Phys. JETP **41**, 960 (1975).

[58] A. Schmid, in *Nonequilibrium Superconductivity, Phonons, and Kapitza Boundaries*, edited by K. E. Gray (Plenum Press, New York, 1981).

[59] R. Mills, *Propagators for Many-particle Systems* (Gordon and Breach Science Publishers Ltd., New York, 1969).

[60] W. Belzig, F. K. Wilhelm, C. Bruder, and G. Schön, Superlattices and Microstructures **25**, 1252 (1999).

[61] G. Eilenberger, Z. Phys. **214**, 195 (1968).

[62] K. D. Usadel, Phys. Rev. Lett. **25**, 507 (1970).

[63] Y. V. N. Dmitri A. Bagrets, cond-mat/0301505 (unpublished).

[64] W. Belzig, An introduction to Full Counting Statistics in Mesoscopic Electronics, Slides of talk given at Lancaster School on Counting Statistics, 2006.

[65] W. Belzig, in *Quantum Noise in Mesoscopic Physics*, edited by Y. V. Nazarov (Kluwer Academic Publishers, Dordrecht, 2003).

[66] Y. V. Nazarov, Phys. Rev. Lett. **73**, 134 (1994).

[67] Y. V. Nazarov, Phys. Rev. Lett. **73**, 1420 (1994).

[68] A. F. Volkov and T. M. Klapwijk, Physics Letters A **168**, 217 (1992).

[69] A. F. Volkov, A. V. Zaitsev, and T. M. Klapwijk, Physica C **210**, 21 (1993).

[70] Y. V. Nazarov, Superlattices and Microstructures **25**, 1221 (1999).

[71] A. V. Zaitsev, Sov. Phys. JETP **59**, 1015 (1984).

[72] K. Kopitzki and P. Herzog, *Einführung in die Festkörperphysik* (B. G. Teubner Verlag, Wiesbaden, 2004).

[73] J. R. Schrieffer, *Theory of Superconductivity* (W. A. Benjamin Inc., New York, 1964).

[74] J. C. Cuevas and W. Belzig, Phys. Rev. B **70**, 214512 (2004).

[75] J. R. Schrieffer and J. W. Wilkins, Phys. Rev. Lett. **10**, 17 (1963).

[76] N. van der Post, E. T. Peters, I. K.Yanson, and J. M. Ruitenbeek, Phys. Rev. Lett. **7**, 2611 (1994).

[77] K. M. Lang, S. Nam, C. U. J. Aumentado, and J. M. Martinis, IEEE Transactions on Applied Superconductivity **13**, 989 (2003).

[78] *Quantum Noise in Mesoscopic Physics*, *NATO Science Series*, edited by Y. V. Nazarov (Kluwer Academic Publishers, Dordrecht, 2003).

[79] W. Nolting, *Grundkurs Theoretische Physik Bd. 6: Statistische Physik* (Springer-Verlag, Berlin, 2004).

[80] J. M. Martinis, cond-mat/0402415 (unpublished).

[81] M. Vanević, Y. V. Nazarov, and W. Belzig, Phys. Rev. Lett. **99**, 076601 (2007).